Dielectric Waveguides for Electromagnetic Band Gap (EBG) Structures, Antennas, and Microwave Circuits

A Thesis

in

The Department

of

Electrical and Computer Engineering

Presented in Partial Fulfillment of the Requirements

for the Degree of Doctorate in Philosophy (Electrical Engineering) at

Concordia University

Montreal, Quebec, Canada

January 2010

CONCORDIA UNIVERSITY
SCHOOL OF GRADUATE STUDIES

This is to certify that the thesis prepared

By: **Michael Wong**
Entitled: **Dielectric Waveguides for Electromagnetic Band Gap (EBG) Structures, Antennas, and Microwave Circuits**

and submitted in partial fulfillment of the requirements for the degree of

DOCTOR OF PHILOSOPHY in Electrical Engineering

complies with the regulations of the University and meets the accepted standards with respect to originality and quality.

Signed by the final examining committee:

Dr. Ramin Sedaghati	Chair
Dr. Derek McNamara	External Examiner
Dr. Marco Bertola	External to Program
Dr. Robert Paknys	Examiner
Dr. Vijay Devabhaktuni	Examiner
Dr. Abdel Razik Sebak	Thesis Supervisor
Dr. Tayeb A. Denidni	Thesis Co-Supervisor

Approved by: Dr. Mojtaba Kahrizi
Graduate Program Director

Dr. Robin Drew
Dean of the Faculty Engineering and Computer Science

Abstract

Dielectric Waveguides for Electromagnetic Band Gap (EBG) Structures, Antennas, and Microwave Circuits

Michael Wong, Ph.D.

Concordia University, January 2010

Dielectric waveguide structures, formed using rectangular blocks of dielectric, can guide electromagnetic energy in a frequency range suitable for new microwave antennas and devices, or between 2 GHz and 18 GHz. In this thesis, we present the analysis and design of thin dielectric waveguide structures so small that for the first time, they can be made economically out of readily available substrates, or circuit boards, even at these frequencies. These strikingly thin metallic-bound dielectric waveguides (H-guides), to be operated in a single fundamental mode, are analyzed and subsequently applied to three brand new applications: a square periodic H-guide structure, an antenna, and a thin H-guide dual-directional coupler.

In the first application, we investigate periodic dielectric structures, or Electromagnetic Band Gap (EBG) structures, where a new model for periodicity applies thin H-guide transmission lines with discontinuities. This model allows for the resonant frequency, transmission (S21), and reflection (S11) parameters of such structures to be found quickly and quite accurately with closed form expressions, without the need for any numerical methods. As an added benefit of the new model, which can be represented as a z-transform, an inverse operation exists, creating the possibility to design a structure that meets a certain frequency response.

In the second application, we explore the use of the thin H-guide as a transmission line feed for a new type of aperture horn antenna that is not only high gain, but also wideband. Incredibly, with proper design, the antenna can also meet low-sidelobe levels between frequencies of 8 and 18 GHz. The proposed thin H-guide aperture horn antennas have wider bandwidths than typical array designs, have similarly high gains as

compared to traditional air-filled horn antennas, and can even be easily fabricated using typical two dimensional substrate machining processes. The prototype operates from 8 to 18 GHz with a peak gain of about 18 dBi with reference to the H-guide transmission line.

To make antenna fabrication and measurement of periodic dielectric structures possible, a new transition based on microstrip design has been carefully developed that exceeds the performance of all previous microstrip to dielectric waveguide transition designs. This wideband, low loss, Bézier-shaped microstrip to thin H-guide transition has been carefully developed and is discussed in detail in this thesis. This transition can even be fabricated using the same two dimensional substrate machining processes used for the H-guide aperture horn antenna, which allows for the seamless integration of the two structures.

Finally, a dual-directional H-guide coupler is discussed that is much thinner than air-filled waveguide designs. The structure is so thin that its total thickness can be less than 2 millimeters, where the design obtains a directivity of better than 25 dB over a large bandwidth of 8 to 14 GHz.

Table of Contents

List of Symbols

∇	Del operator
α	Attenuation constant
α_{xo}	Attenuation constant in the x direction outside the dielectric
Γ	Reflection coefficient
Γ_{uv}	Reflection coefficient from region "u" back into region "v"
λ	Wavelength
a	Width of dielectic slab
A_d	magnitude constant inside the dielectric
A_o	magnitude constant outside the dielectric
β	Propagation constant
β_{xd}	propagation constant in the x direction inside the dielectric
β_{yd}	propagation constant in the y direction inside the dielectric
β_y	propagation constant in the y direction both inside and outside the dielectric
β_z	propagation constant in the z direction inside and outside the dielectric
β_z	propagation constant in the z direction inside and outside the dielectric
ε_o	dielectric constant of free space, 8.8541878176 … x 10^{-12} F/m
ε_r	Relative dielectric constant to free space
ε_d	dielectric constant of the dielectric
E	Electric Field
f_c	Cutoff frequency
$\overline{F}$	Vector potential function
$F_z(x,y,z)$	Potential function in the z direction
F_{zd}	potential function inside the dielectric
F_{zo+}	potential function outside the dielectric where $x > a/2$

F_{zo-}	potential function outside the dielectric where $x < -a/2$
H	Magnetic field
H or h	Height
P0, P1, P2, P3	Points in a Bézier curve
W	Width
x	Distance along x axis
y	Distance along y axis
z	Distance along z axis
v	Velocity
S	Magnitude of Power Density
S	S parameter
Z_g	Wave impedance of an H-guide
Z_v	Wave impedance inside a vane

Abbreviations

mm	millimeters
dBi	Decibel isotropic, the gain in decibels above an antenna with isotropic gain
PEC	Perfect Electric Conductor
PMC	Perfect Magnetic Conductor
PBG	Photonic Band Gap
DC	Direct Current
EBG	Electromagnetic Band Gap
EBP	Electromagnetic Band Pass
FDTD	Finite Difference Time Domain
FEM	Finite Element Method
HD	High Definition
HFSS	High Frequency Software Simulator

LSE	Longitudinal Section Electric
NRD	Non-Radiative Dielectric
FR4	Fire Retardant substrate
RF	Radio Frequency
TE	Transverse Electric
TM	Transverse Magnetic
TEM	Transverse Electric and Magnetic
FEM	Finite Element Method
HFSS	Ansoft High Frequency Software Simulator, a commercial software package, currently part of the ANSYS Inc. product range.
TIR	Total Internal Reflection
KOH	Refers to KOH Etching, where heated Potassium Hydroxide (KOH) solutions are used.

Chapter 1: Introduction

The introduction discusses the motivation and objectives behind the study of dielectric waveguide transmission lines and antennas. It then concludes with a brief overview of this document.

1.1 Motivation

Recently, wireless radio frequency (RF) / microwave technologies have vastly improved in terms of reliability and technological advancements. It has therefore become perhaps the most popular method for moving information between two points; for example, in terms of cellular telephony vs. land lines, wireless internet vs. wired internet, or even in some remote locations, cable television vs. satellite television. These particular wireless applications have become virtually ubiquitous and are almost taken for granted in most modern cities throughout the world.

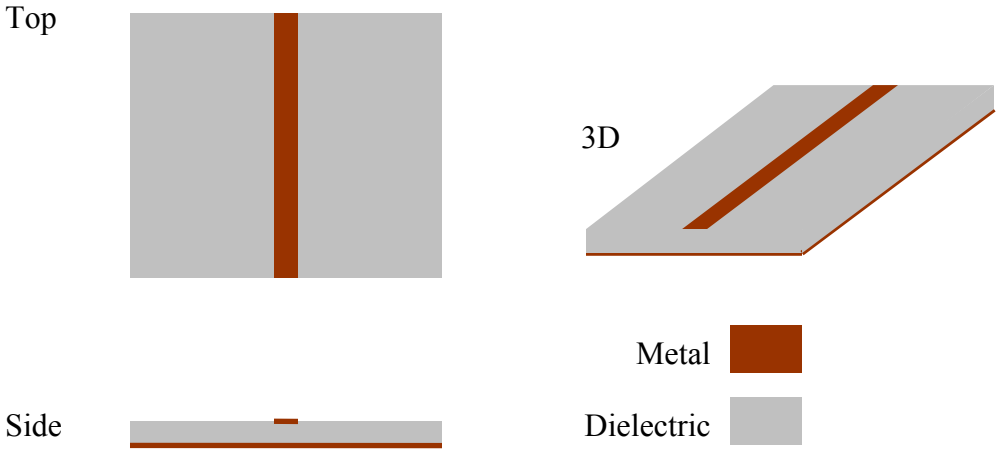

Fig. 1.1 The microstrip line.

The technologies required for transmitting this information through the air must include antennas and microwave circuits, which are in general made up of microwave components connected by a network of transmission lines. Transmission lines are therefore necessary structures which make wireless communications possible. They are the structures which carry energy, signals, and information necessary for modern-day devices. A common transmission line is the microstrip line [1] as shown in Fig. 1.1,

which is suitable for miniaturization in microwave circuits. Another useful transmission line that will be discussed is the dielectric waveguide, which will be discussed primarily in the form of the H-guide [2] as shown in Fig. 1.2. The H-guide consists of a rectangular dielectric block sandwiched by two metallic plates. Since the H-guide is a waveguide, it is well suited for antenna applications. In addition, since the H-guide does not require metallic sidewalls, it is easy to fabricate as compared to traditional waveguides as discussed in [1]. Therefore, if the H-guide may be fabricated in a similar process as the microstrip line, shown in Fig. 1.1, it could be applied to general applications in many devices.

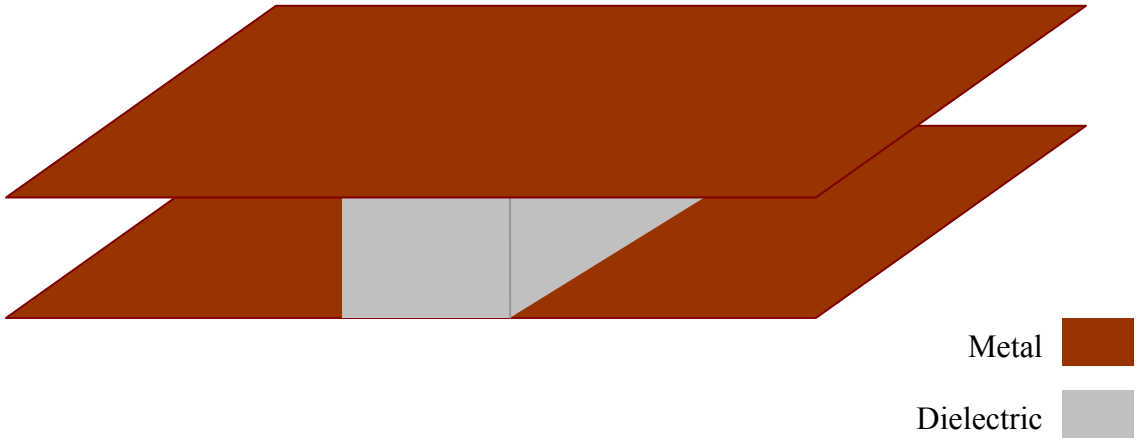

Fig. 1.2 The H-guide consists of a rectangular dielectric block sandwiched by two metallic plates.

Interestingly, periodic structures can also be used to form transmission lines in the form of waveguides within a small bandwidth, termed the "band gap" [3]. These structures have originated with the study of optical devices, and are hence termed Photonic Band Gap (PBG), or photonic crystal [3] structures when applied to optical frequencies. Two dimensional PBG structures (see Fig. 1.3) and devices promise a whole new range of devices that were not previously thought possible, such as waveguides and other structures as discussed in [3]. Bloch [4] and Brillouin [5] [6] have initially suggested that such structures may have unique properties.

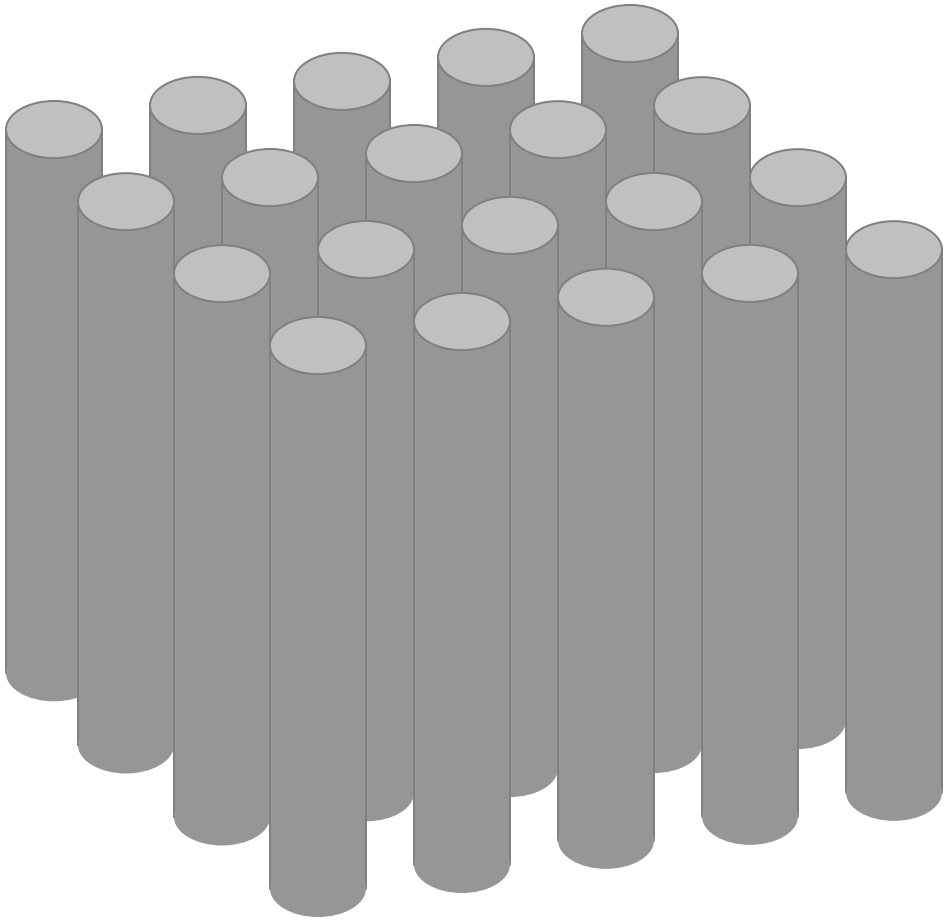

Fig 1.3 A two dimensional PBG structure consisting of dielectric cylinders.

PBG structures have not only been applied to linear materials, in fact, recent research has applied this technology to control the flow of light with a “birefringent nematic liquid crystal” which fills the gaps of a three dimensional PBG structure [7]. Light properties through this structure can then be controlled with the use of an electric field. Other mixed applications include combining PBG materials with semiconductors [8] to control spontaneous emission. These advanced applications show many possible new applications for general PBG structures, which makes this topic ideal for new research. This thesis will concentrate itself around microwave frequencies, where PBG structures are frequency referred to as Electromagnetic Band Gap (EBG) structures.

1.2 Thesis Objective

The objectives of this thesis are to

1) Confirm that the H-guide is a useful, wideband, low loss transmission line at microwave frequencies through simulation and fabrication.
2) Confirm that the dielectric waveguide (or H-guide) can be used to mathematically model dielectric EBG structures and thus give a good estimate of the frequency response of certain two dimensional EBG structures.
3) Demonstrate that the H-guide can be used for new applications with antennas and microwave devices such as a directional coupler.
4) Design a transition structure that allows the integration of H-guide microwave devices, H-guide antennas, EBG structures, and microstrip circuits into a single device.

1.3 Thesis Overview

This document follows with Chapter 2 entitled Background that begins with a description of the dielectric slab waveguide, and includes a literature review of electromagnetic and photonic band gap (EBG and PBG) structures related to the thesis. In addition, the relationship between the dielectric slab waveguide and the H-guide and discussed. We show how it is possible to bind the top and bottom of classic PBG structures with metallic plates, where the height may be much smaller than the wavelength, and discuss existing designs which use this approach.

In Chapter 3, dielectric waveguide structures which apply to this thesis are discussed. "An Electromagnetic Band Pass Waveguide" demonstrates that a wave may propagate inside a periodic structure, where previously periodic structures were used to block waves. "A Via-Less EBP Horn Antenna" demonstrates a microstrip to EBP transition, and the broadside aperture. In addition, we have presented simulated results for a wideband dielectric slab waveguide bounded by metallic plates (H-guide), a structure which provides the foundation for many new wideband devices, such as the H-guide aperture antenna.

In Chapter 4, a new model for accurately predicting the insertion and return loss of a periodic structure is discussed. This model is based on a multiple reflection model, where the final solution represents a z-transform (discrete Fourier transform). Because of this representation, it is theoretically not only possible to find the frequency response of a structure, but to design a structure that meets a certain frequency response.

In Chapter 5, a wideband Bézier-Curve shaped microstrip to H-guide transition is discussed. This transition is necessary to measure the structures in this thesis. Other existing transitions are not wideband, are intended for the NRD, or do not use a simple microstrip line and thin H-guide. The thin H-guide is so small that regularly available substrates may be used, such as FR4, Rogers 6006, or Rogers 5880.

In Chapter 6, a wideband, high gain, low sidelobe H-guide aperture horn antenna is discussed. This antenna employs the transition discussed in Chapter 5 to obtain its wideband characteristics, and the H-guide as discussed in Chapter 3. A "gapped" configuration for the H-guide allows a smooth transition from the H-guide to free-space.

Finally, in Chapter 7, an externally terminated dual directional coupler is investigated. This coupler achieves a directivity of better than 27 dB from 8 to 14 GHz.

In Appendix A, we have provided a detailed derivation of TE modes of an infinite dielectric slab waveguide bounded by metallic plates, where TM modes are more commonly discussed.

In Appendix B, the H-guide is discussed. In Appendix C, the rectangular dielectric waveguide is briefly discussed.

In Appendix D, some qualitative comparisons between different transmission lines are made. Appendix E discusses some issues with simulations in HFSS. Finally, some practical examples are discussed in Appendix F.

Chapter 2: Background

In this chapter, the dielectric waveguide is reviewed in the form of the infinitely large dielectric slab for the TE mode case. Its relationship with the H-guide is then discussed by comparing the structure with an infinite dielectric slab with metallic plates. We then examine some of the history of Photonic Band Gap (PBG) and Electromagnetic Band Gap (EBG) structures and discuss some common applications. Finally, some applications for dielectric waveguides in the form of the Non-Radiative Dielectric (NRD) and fiber optic cables are discussed. The relationship between the dielectric waveguide and periodic structures is discussed in later chapters.

2.1 Dielectric Waveguides

For most engineering applications at microwave frequencies, waveguides consist of hollow, rectangular metallic structures which guide waves through its air core. It is also possible to guide waves within dielectric structures surrounded by air, as analyzed in [9] [10] [11], or to construct novel devices for practical engineering applications [12].

2.1.1 Fiber Optic Cables

Multimode fiber optic cables are another practical application of the dielectric waveguide. In this structure, the cable typically consists of a higher dielectric constant is surrounded by a lower one, as shown in Fig. 2.1. These structures operate on the principle of total internal reflection (TIR) [10], which requires that $\varepsilon_{r1} > \varepsilon_{r2}$. According to this principle, if an incident wave in a higher dielectric constant (core) is incident on a border with a lower dielectric constant (cladding) with an angle greater than the critical angle, the wave will be totally reflected, hence total internal reflection.

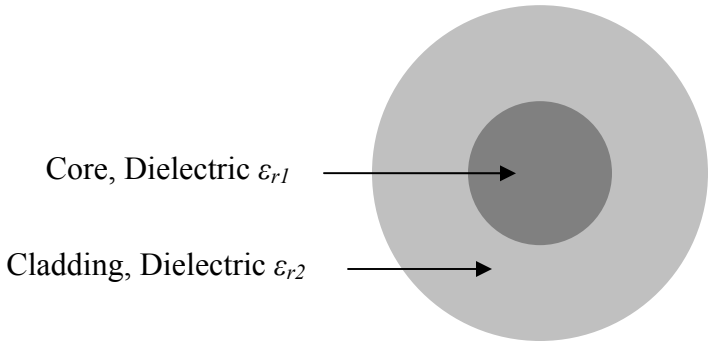

Fig. 2.1 Main elements of a typical multimode fiber optic cable.

2.1.2 The Infinitely Large Dielectric Slab Waveguide

The dielectric slab waveguide has been analyzed using Maxwell's equations and boundary conditions for TM modes, as discussed in [10][11]. In this section we consider the TE mode rectangular problem that consists of an infinitely large slab of dielectric with dielectric constant ε_d, sandwiched between a second dielectric ε_o on both sides in the y direction. Details of this structure are discussed in Appendix A. The structure extends to infinity in the y-z plane, where we examine propagation in the z direction as shown in Fig. 2.2. Because of the infinite size in the y dimension, we can assume that

$$\frac{\partial E}{\partial y} = 0 \tag{2.1}$$

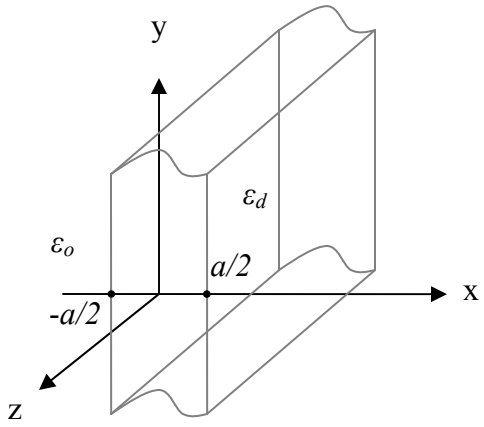

Fig. 2.2 A two dimensional Dielectric Slab Waveguide of width "*a*" with dielectric constant ε_d is infinitely large in the y and z directions. It is sandwiched between a medium with dielectric constant ε_o. We wish to consider the propagation in the +z direction.

Then, from the Appendix, the cutoff frequencies for odd modes [9] [10] [11] is,

$$f_c = \frac{n}{2a\sqrt{\varepsilon_d \mu_d - \varepsilon_o \mu_o}} \tag{2.2}$$

where for odd modes, n = 1, 3, 5, etc…

For even modes, n = 0, 2, 4, etc… where the entire derivation above is repeated [10]. TM modes are found the same way. We note that in Eq. (2.2), the cutoff modes for both the TE and TM modes begin at 0 Hz for TE_0 and TM_0. Again, as in the case for TIR, this equation provides real numbers only if dielectric constant ε_d is larger than dielectric constant ε_o.

2.1.3 The H-Guide: The Infinite Dielectric Slab Waveguide Bounded by Metallic Plates

In this section we consider an infinitely large dielectric slab in the yz plane similar to the previous section, however, bounded by two infinitely large metallic plates in the xz plane as shown in Fig. 2.3(a) and Fig. 2.3(b). This structure is called the H-guide and has been considered in [2] with similar results.

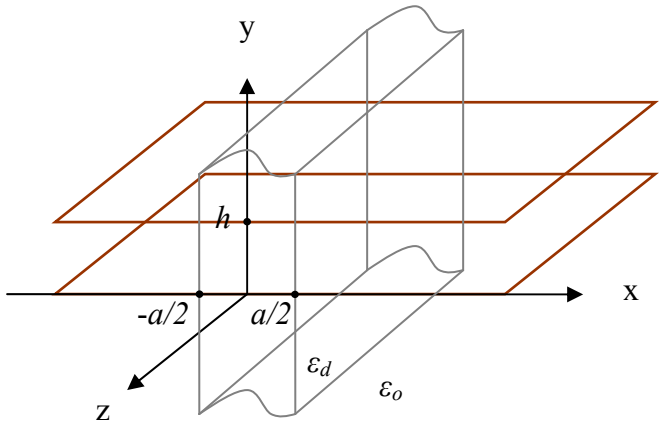

Fig. 2.3(a). A two dimensional Dielectric Slab Waveguide of width a that is infinitely large in the yz plane, cut by two infinitely large metallic plates in the xz direction.

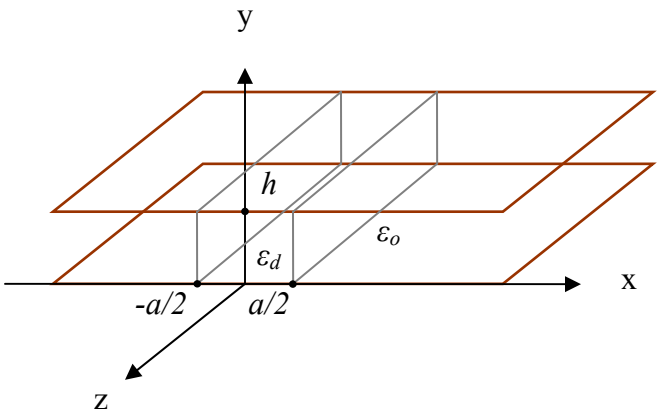

Fig. 2.3(b). The H-guide: The equivalent problem as above. A rectangular dielectric slab extends from $x = -a/2$ to $x = a/2$ and is bounded at $y = 0$ and $y = h$ by metallic plates. The structure continues to infinity in the +z and –z directions.

Details of the H-guide and how a large bandwidth is possible with regular, commonly available substrates are outlined in Appendix B. Losses for different modes through the H-guide for Rogers 5880, FR4, and Rogers 6006 are discussed in Chapters 4, 5, and 7.

In general, optical structures that are based on TIR principles may have losses as low as 0.15 dB / km [13]. In addition, TIR principles may be combined with EBG principles [14] to form new devices that offer new possibilities, such as being more resistant to dielectric breakdown, and permitting more flexibility than conventional optical fibers. In future research, we might apply these concepts to our structures for further improvements in performance.

2.2 Photonic Crystals

Recently, periodic structures in the sub-wavelength range have been applied to materials to form various effectively new material types that were not previously thought possible. These structures have been named Photonic Band Gap (PBG) materials because in the photonic frequency band, a "gap" exists where waves cannot propagate [15], where waves in a small frequency band may be confined to propagate in certain directions only. Typically, these photonic crystals consist of periodic gaps in a suitable light-transmitting substrate of specific shape, depending on the application. In addition, these structures are typically very small [16]. It is only recently that very large three dimension structures have been investigated. One such three dimensional structure includes the woodpile

structure [17], which is formed using the same etching process as for manufacturing semiconductor structures, such as use of a semiconductor dicing saw, KOH etching, or active ion etching [18].

2.2.1 Two Dimensional Photonic Crystal

One such structure is the two-dimensional band gap structure, where gaps may consist of holes drilled within the substrate using lasers in a square lattice pattern such as in Fig. 2.4.

In microwave frequency bands, band gap structures can exist in various formats. In two dimensions, one typical application is to construct a series of long (in terms of wavelengths) dielectric rods arranged in a periodic fashion [19], as shown in Fig. 2.5. These structures might be called PBG materials because of their origins in photonics, however, they have also been called Electromagnetic Band Gap (EBG) structures because of their application to microwave frequency bands.

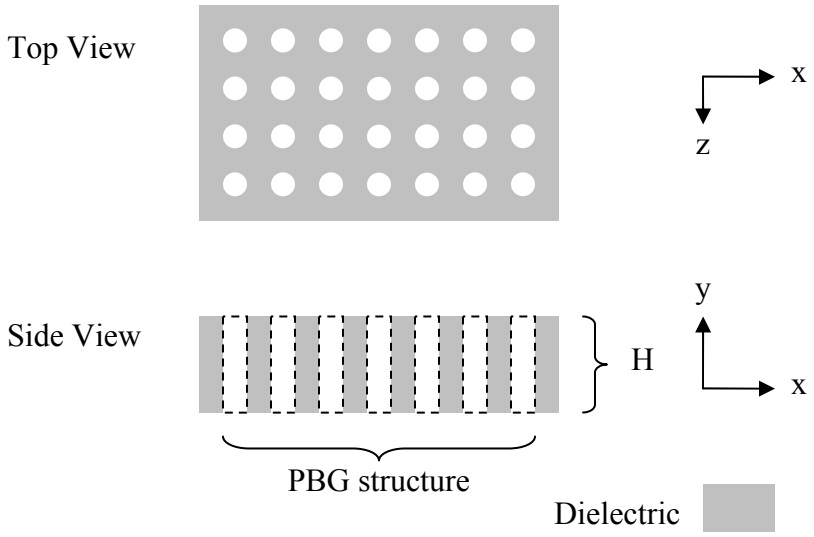

Fig. 2.4 Two Dimensional Photonic Band Gap (PBG) structure in a square lattice pattern. The structure consists of holes (white circles) drilled within a substrate (grey areas), whose height is H.

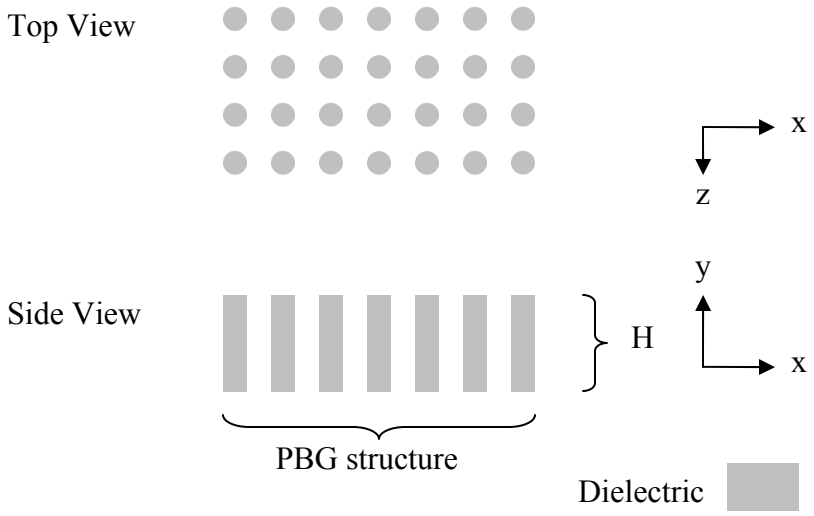

Fig. 2.5 A two dimensional PBG structure for microwave frequencies consisting of dielectric rods (grey cylinders) placed in a square lattice periodic pattern.

In applications such as the two dimensional PBG structure shown in Fig. 2.5 [19], the structure is normally made large in the y-dimension (height H) to approximate an infinitely large structure in that dimension.

2.3 Photonic Band Gap (PBG) Waveguide

Typically, the photonic crystals are used such that the "band gap" mode is used to block waves from passing in certain directions at certain frequencies. "Defects" may be added to photonic crystals to create a contrast with the band gap region and cause localization of energy [20]. A defect is an imperfection in the structure such as that shown in Fig. 2.6. In this application, the defect forces the wave to be guided in a certain direction just like a waveguide [15].

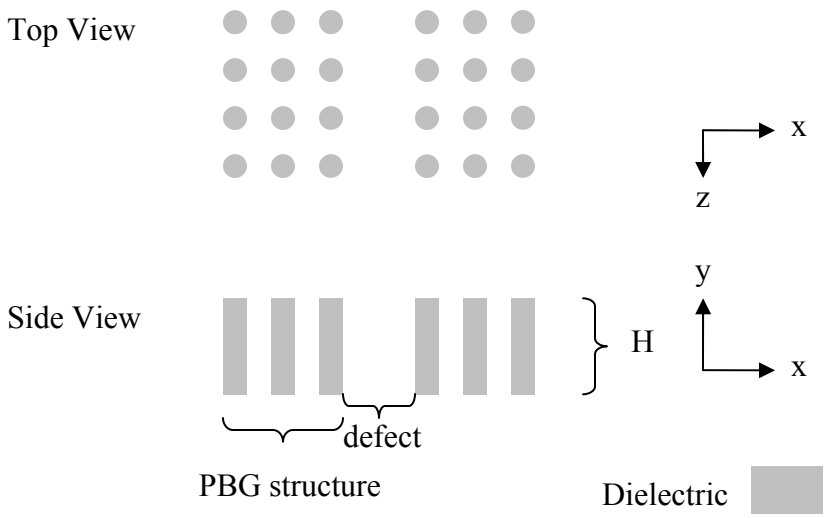

Fig. 2.6 Waveguide application for EBG structure using dielectric rods. The wave travels between the rods in the z direction within the defect.

The inverse structure may also guide waves, where instead of holes in a dielectric, the structure consists of dielectric rods [15] as shown in Fig. 2.7. The EBG waveguide structure has the advantage over structures that make use of total internal reflection (TIR) because this structure may accommodate a sharp bend that was not previously possible [3], as shown in Fig. 2.8.

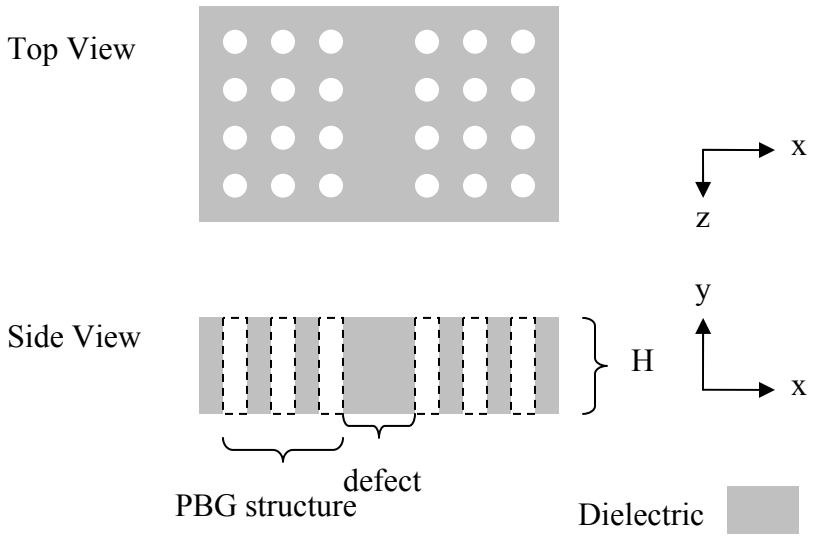

Fig. 2.7 Waveguide application for EBG structure using a two dimensional Photonic Band Gap (PBG) structure in a square lattice pattern. The structure consists of holes (white circles) drilled within a substrate (grey areas), whose height is H.

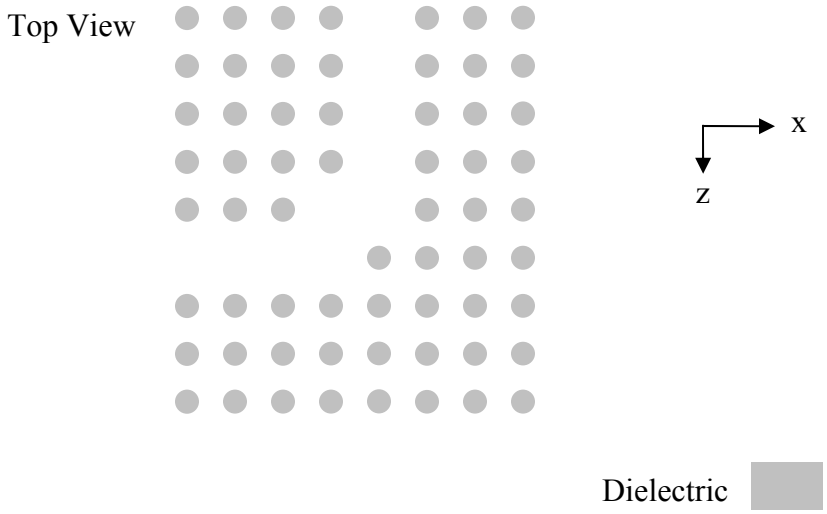

Fig. 2.8 A sharp bend implemented using a PBG waveguide structure.

It is also possible to use woodpile structures to form similar microwave devices, as discussed in [21].

2.3.1 Photonic Band Gap Ring Coupler

Complicated devices may also be fabricated using PBG structures. One such example is the ring coupler, which can couple various amounts of energy from one port to another port depending on geometry [19]. In this example, the researchers have performed experiments in the 27 to 75 GHz range using the Finite Difference Time Domain (FDTD) simulations and have then constructed a prototype to verify results.

The PBG crystal structure consists of a cube of foam dielectric with effective dielectric constant of approximately $\varepsilon_r = 1$, where a square lattice of cylinders is drilled into the foam using a numerically controlled drilling machine to accept a lattice of alumina rods with effective dielectric constant of $\varepsilon_r = 9$ [19] as shown in Fig. 2.9. The lattice consists of 18 x 11 rods that are 1.5 mm in diameter and 5 cm in length. The edges of the crystal are then buffered with a layer of microwave absorber. Two horns with collimating lenses serve as ports for the source and the output.

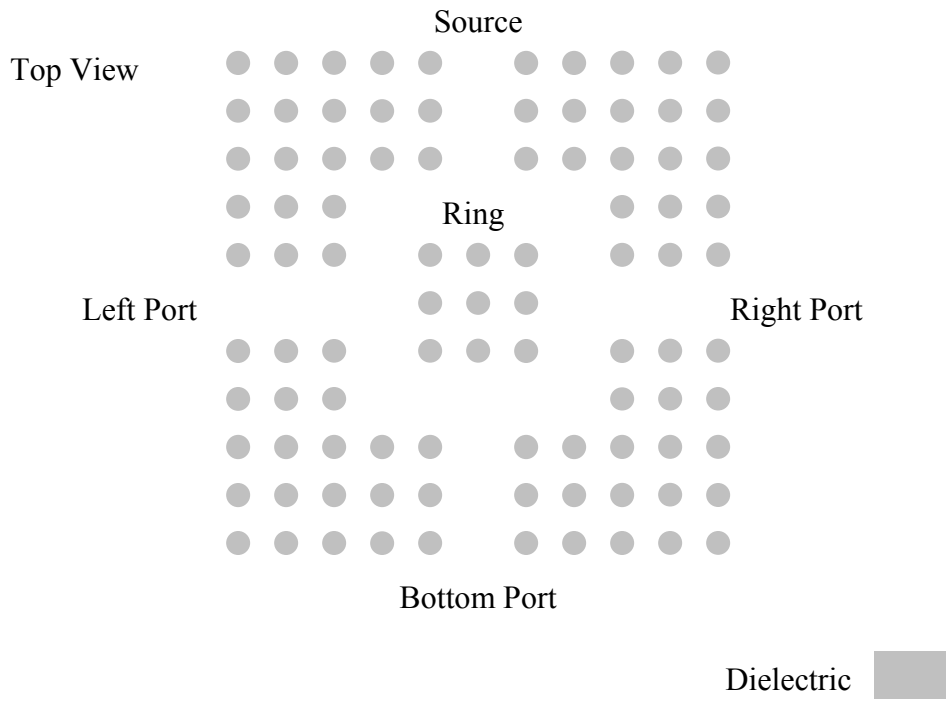

Fig. 2.9 Ring Coupler using dielectric rods.

In this example, we are assuming that the height of the rods is large enough that losses due to obstructions (or termination of the structure) in the vertical direction are neglected. Additional research in this area is found in [22], where researchers use the FDTD method to analyze similar PBG devices.

2.4 A Parallel Plate Analogy

Recently, periodic structures in metallic-bounded substrates have been popularized [6] [23] for microwave applications. At microwave frequencies, metallic structures appear to be perfect electric conductors, or perfect reflectors. This allows us to replace an infinitely large structure with a smaller, more compact one that behaves similarly to the PBG structures discussed above as shown below in Fig. 2.10. The same property has allowed us to consider the H-guide as an infinitely large dielectric slab in the previous sections.

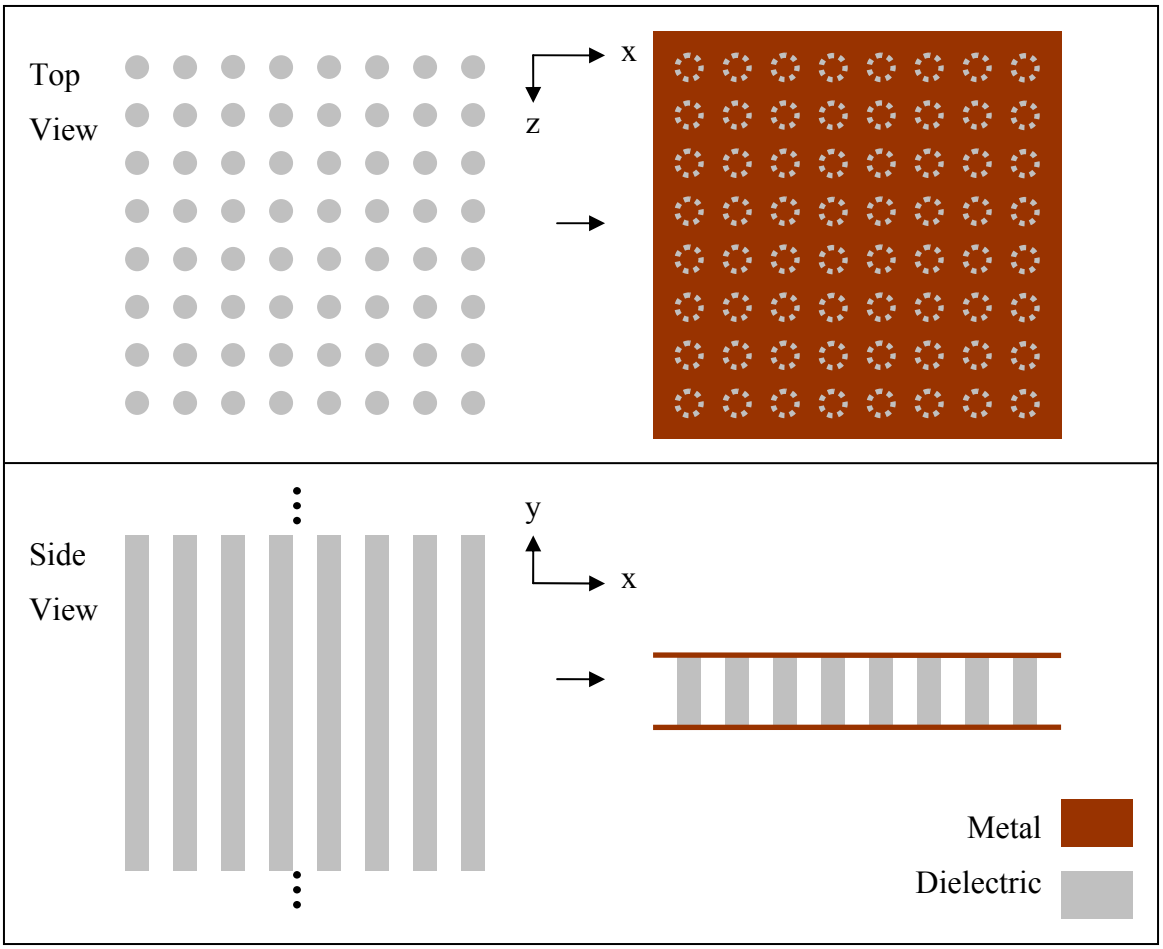

Fig. 2.10 Parallel metallic plates are used to bind a square lattice of dielectric rods to provide a significant reduction in size. On the left are top and side views of a structure that is infinitely tall in height, while on the right there are top and side views where two metallic plates limit the height with a separation less than a half wavelength.

The structure shown in Fig. 2.10 has obvious advantages, most notably the reduction in size in the y-dimension, or height H. We can *approximate* the behavior of an infinitely large y dimension, or height H, by realizing that when bounded by parallel plates that are separated by less than a half-wavelength, the variation of the electric field in the y dimension is approximately zero for TEM and TE_{m0}, which will be shown in the following sections. This can then be written as,

$$\frac{\partial E}{\partial y} \approx 0 \tag{2.3}$$

For a structure that is infinitely large in the y-dimension we also assume zero variation in the electric field as is assumed in (2.1); therefore, we may construct similar devices as for

those that are infinitely large in the y-dimension as discussed in previous sections, while maintaining a very small height of the structure, H.

2.4.1 The PBG Waveguide with Metallic Plates

One PBG waveguide [23] application makes use of metallic plates which bind the top and bottom of the waveguide similarly to [6]. A PBG structure formed using holes in the substrate (dielectric) serves as a border on the left and right sides of the waveguide, while the top and bottom of the waveguide are bordered by the metallic plates as shown in Fig. 2.11.

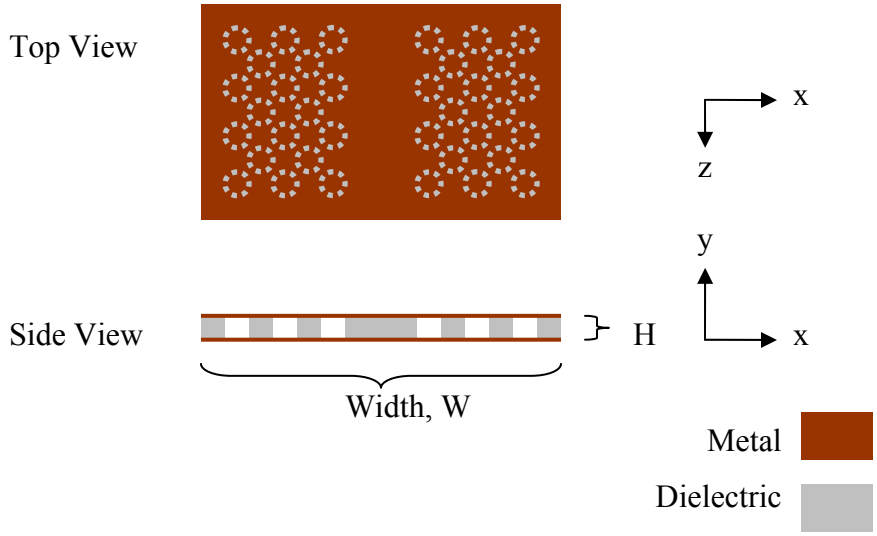

Fig. 2.11 Holes are drilled into the substrate and are then covered with a metallic layer forming a PBG waveguide.

With the waveguide shown above in Fig. 2.8, it is possible to form filters by adding additional posts or holes within the waveguide section [23].

2.5 Some Previous Work

In this section, some previous work relating to this thesis is discussed.

2.5.1 Transition to Dielectric Waveguides

Researchers have previously addressed the need for dielectric waveguide excitation through various different designs. One example is a microstrip to NRD transition discussed in [24] as shown in Fig. 2.12.

Top View

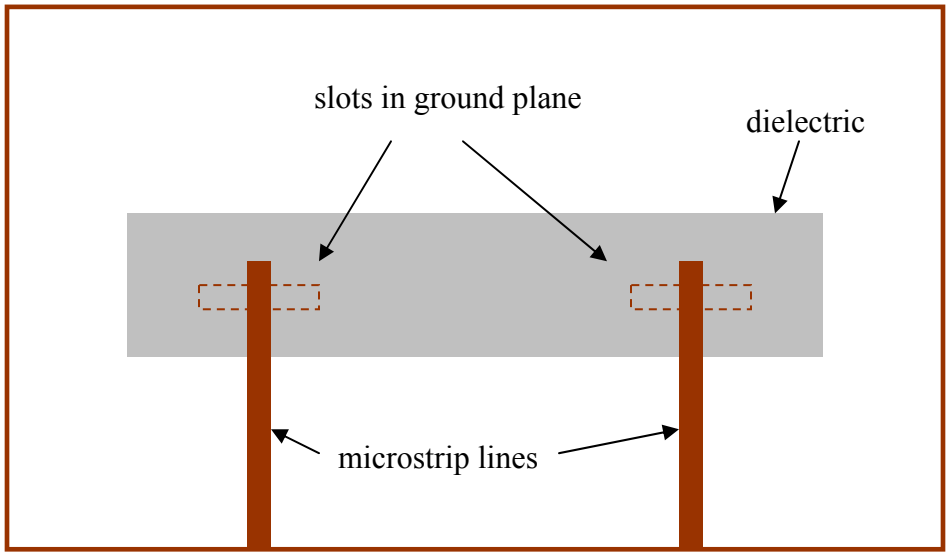

Side View

Fig. 2.12 Transition from microstrip to NRD waveguide.

In Fig. 2.12, a microstrip line terminates in an open circuit and feeds a slot in the ground plane. The transition excites the modes required for NRD waveguide operation.

Another example of a transition is a wideband waveguide to NRD transition proposed in [25] as shown in Fig. 2.13. In this design, a slow taper ensures wideband operation. Note that the top view of a standard air-filled waveguide joins with the side view of the NRD and vice-versa.

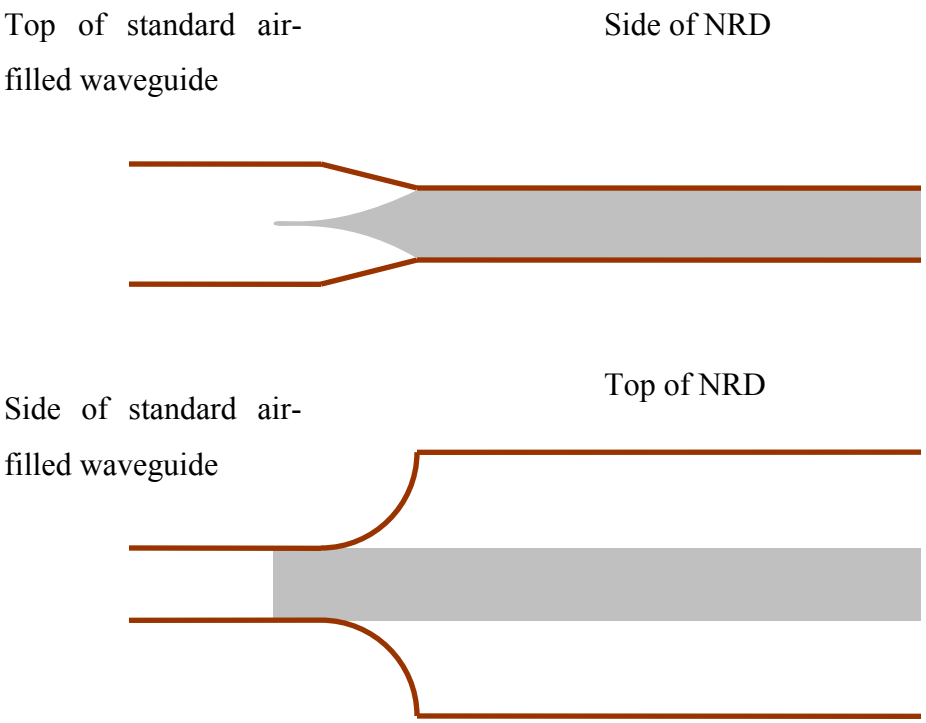

Fig. 2.13 Wideband air-filled waveguide to NRD waveguide transition.

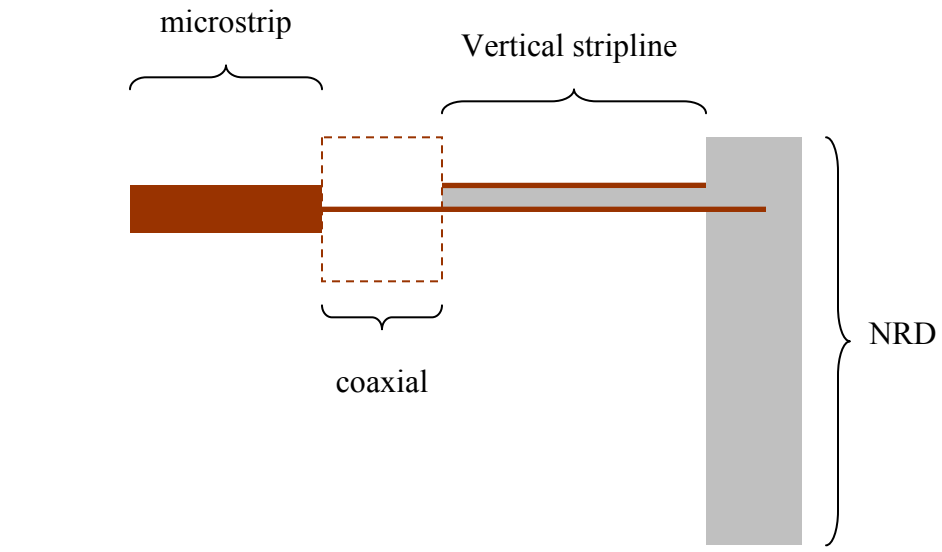

Fig. 2.14 A microstrip to NRD transition for 60 GHz applications.

A third transition design addresses the improvement of the microstrip to NRD transition at 60 GHz [26] [27]. This transition, however, requires that a complete microstrip-

coaxial-vertical-stripline-NRD transition be designed to feed the NRD, as shown in Fig. 2.14.

2.5.2 Dielectric Waveguide Antenna Designs

In this section, various strategies for using dielectric waveguides as antennas are discussed. One example is the multiple slot NRD waveguide, which achieves approximately 10 to 11 dBi of gain with 10 slots, or elements, arranged for broadside radiation [28] [29]. The top sheet of the NRD contains tiny slots at an angle to the NRD. This antenna is shown in Fig. 2.15.

Top View

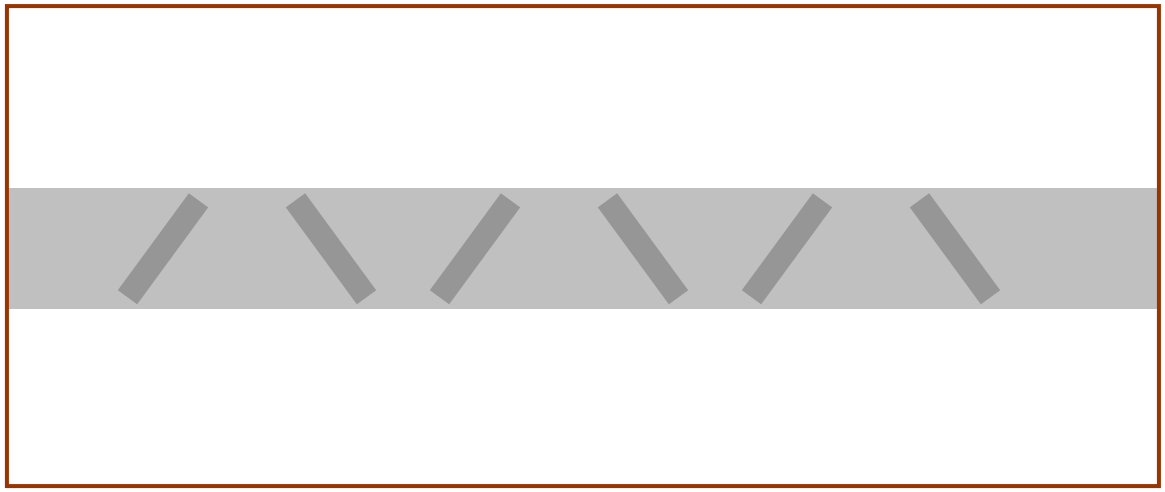

Fig. 2.15 Six Slot Broadside NRD waveguide antenna. Top and bottom metallic plates cover the dielelectric rectangular block. Darker grey areas show where slots are cut into the top metallic plate.

Another example of an antenna that achieves high gain is the leaky wave design proposed in [30]. The structure consists of an NRD dielectric guide cut that is with grooves so that it becomes "leaky". The radiation is then allowed to leak into slots cut along a large ground plane, as shown in Fig. 2.16.

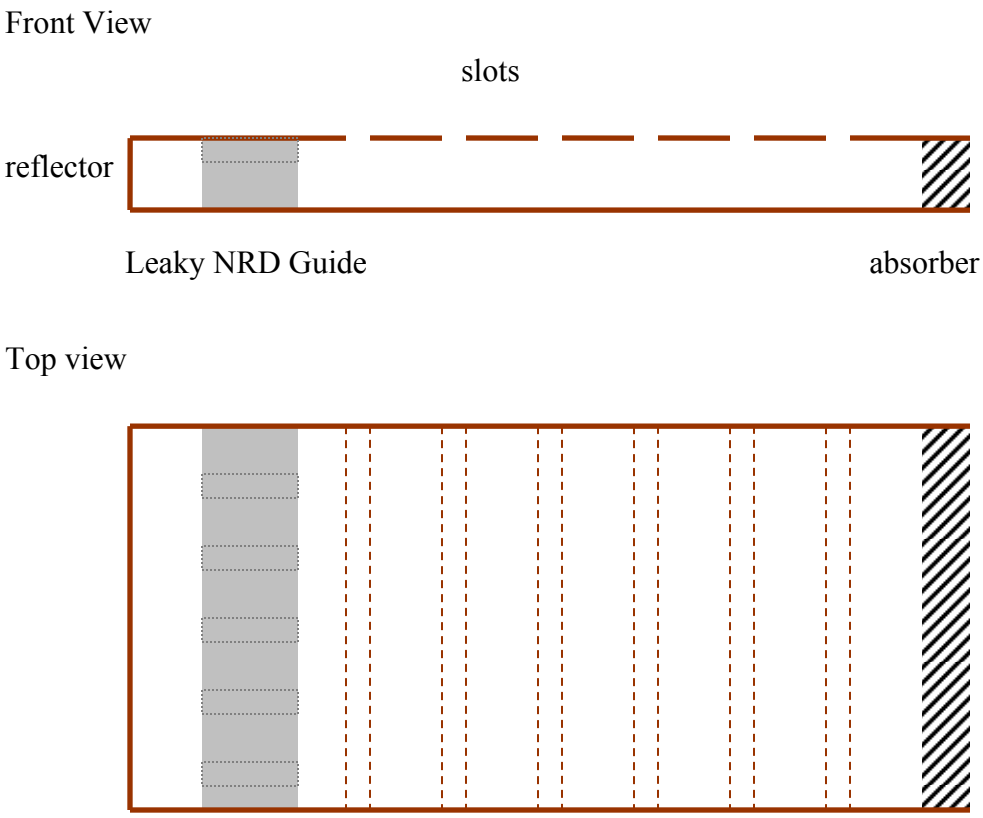

Fig 2.16 A leaky wave NRD antenna.

The antenna shown in Fig. 2.16 measures 290 mm by 165 mm and achieves a peak gain of 32 dB at 23 GHz.

Fig. 2.17 Periodic slots cut into the dielectric of the leaky wave NRD antenna.

From the side, the grooves that have been cut into the NRD dielectric structure are made visible, as shown in Fig. 2.17. This is essentially a periodic structure, which will be discussed in the next section.

2.5.3 Periodic Structures

Several attempts to model periodic structures have been made by using transmission line models [31] [32].

In one such method, the single metamaterial cell is simulated in a commercial software package, then using Bloch wave analysis, the transmission parameters are found through a simplified structure. A close match between simulated and modeled parameters is observed because a numerical simulator has been used for the single unit cell.

In another method, an equivalent circuit diagram is applied to a periodic structure [32], so that transmission parameters in terms of a 2D Brillouin diagram are then easily obtained.

2.5.4 Dielectric Waveguide Couplers

Typical dielectric waveguide directional couplers consist of bent transmission lines whose separation approaches a minimum over a certain distance [33], as shown in Fig. 2.18. Since different modes within the structure couple at different strengths, analysis for multimode dielectric waveguides, such as common fiber optic cables, can be complicated.

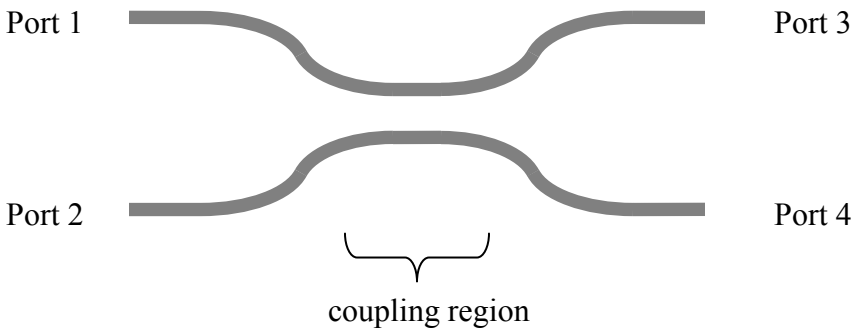

Fig. 2.18 A dielectric waveguide coupler.

2.5.5 Metamaterials and H-guides

Recently, researchers have used the H-guide as a transmission line to investigate propagation through metamaterial structures [34]. These structures are those that may have unexpected properties, such as negative propagation constants. The authors have considered propagation where the regular dielectric slab has been replaced by a double negative material, as shown in Fig. 2.19. One such practical implementation of a double-negative material involves the embedding of many sub-wavelength sized "omega" shaped metallic structures inside the waveguide [35].

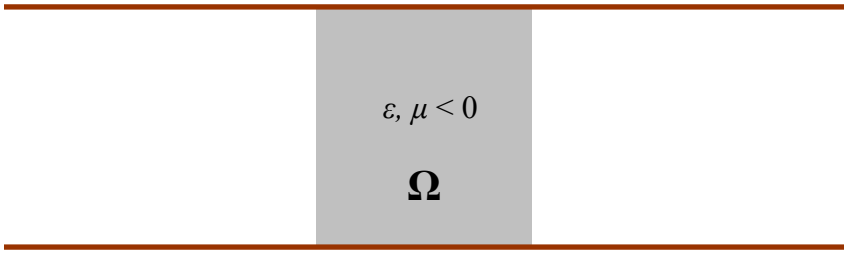

Fig. 2.19 An H-guide with a double-negative dielectric slab.

2.6 Numerical / Analytical Techniques

Many of the structures discussed in this chapter can be modeled using commercial software, such as the Ansoft high-performance software HFSS [36], currently part of the ANSYS, Inc. product range. This structure is well-suited for numerical simulation of complex, passive, three dimensional structures that may include air, dielectrics, or metallic surfaces. A Computer Aided Design (CAD) type environment allows the drawing and viewing of such complex structures, while a powerful numerical software engine analyzes the structure using a user-friendly graphic interface.

HFSS [36] is based on the Finite Element Method (FEM), which is a frequency-domain numerical technique that solves Maxwell's equations. HFSS divides the solution space into thousands of small tetrahedral shapes, whose size and placement depend on the dielectric constant of the materials, placement of sources, proximity to metallic surfaces, etc. A complex software package such as this generally takes several years for one

person to develop and test. This and other equally high-performing software have been commercially available for several years.

The H-guide and its related structures can support frequencies down to 0 Hz, however, are not TEM transmission lines. The consequence of this property is that the size of the propagating wave and its propagation characteristics vary with frequency. This is very problematic for certain simulation techniques, such as the Finite-Difference Time Domain (FDTD) method. The DC component, in particular, is always present in some amount during an FDTD simulation, however, will cause a static DC charge to build up between the two metallic plates of the H-guide. This static DC charge causes problems in FDTD simulations in large-time simulations, which are necessary for simulation of large structures. Frequency domain techniques such as the FEM used in HFSS, however, do not have this problem, which is one reason why it is chosen as the simulation technique for this thesis.

Because the H-guide structure's fields vary with frequency, a waveport must be used to excite the structure. In HFSS, this type of port must be located at the very edge of the solution space. Inside the port, HFSS assumes an infinitely long structure of the same material characteristics as on the face of the port. The fields are then excited using a shape that is found through a two-dimensional electromagnetic solution over the face of the port. The modes that are excited can be chosen, which makes the waveport a very useful simulation tool.

One disadvantage of the waveport is that it must lie at the edge of the solution space so that near fields used to form the far field antenna patterns must exclude the waveport. Another disadvantage is that solutions generated with a waveport are not guaranteed to reveal a true final simulation, because the software enforces only a certain mode (chosen by the user) to exist. This is one of the reasons why the dimensions of the H-guide are chosen so that only the fundamental mode propagates with low losses. Simulation results appear in the following sections while addition considerations for HFSS are included in Appendix E.

2.7 Summary

In this chapter, the background needed to discuss the relationship between the dielectric waveguide, photonic band gap structures, and the H-guide structures is outlined. Some existing dielectric waveguide structures in the form of photonic crystals and the NRD have been discussed, and a short discussion concerning numerical simulations has been summarized. This chapter is only the preface to a more detailed study of these relationships that follows in the next chapters.

The Appendices provide additional information concerning this chapter. Appendix A provides additional information for the dielectric waveguide, while Appendix B explains the H-guide in more detail. Appendix E discussed some numerical simulation techniques needed for the simulations discussed in the following chapters.

Chapter 3: Dielectric Waveguide Structures

In this section, dielectric waveguide structures are investigated. One such structure is the Electromagnetic Band Pass (EBP) waveguide, the second is the H-guide. The relation between the two structures is discussed in more detail in Chapter 5.

3.1 Introduction

In this thesis, new EBG antennas and microwave devices have been proposed for integration with existing microwave components. To gain a feel for the structure's necessary dimensions, closed form solutions are very useful. The following solutions provide us with not only a starting point for numerical simulations, but give us an accurate estimate for the first resonant frequency of the square periodic structure. In addition, the following analysis provides a model that explains propagation through a medium that has a lower average, or effective, dielectric constant that its surrounding structures, where, according to (2.2), the cutoff frequencies are imaginary. This chapter begins with the description of such a medium and one antenna application. The chapter continues with the theoretical analysis of the square periodic H-guide.

3.2 The Electromagnetic Band Pass Waveguide

3.2.1 An "Unexpected" Effective Dielectric Constant

Energy may flow inside a two dimensional crystal lattice at certain frequencies and in certain directions [37]. In fact, at frequencies other than the Band Gap, a wave may propagate within the structure at a certain *effective* dielectric constants. Such effective dielectric constants have been plotted [15]. It is possible to find a bound on the effective dielectric constant by using the Wiener Bound [15] as shown in (3.1).

$$\left(\frac{1}{x_1\varepsilon_1}+\frac{1}{x_2\varepsilon_2}\right)^{-1} \le \varepsilon_{eff} \le x_1\varepsilon_1 + x_2\varepsilon_2 \tag{3.1}$$

where ε_α is the effective dielectric constant and x_1 and x_2 are the volume fractions of the material.

We have simulated the square periodic structure shown in Fig. 3.1 and have shown that propagation is possible within this structure. Some preliminary results appear in [38]. The effective dielectric constant within the electromagnetic band pass (EBP) structure is, however, less than the dielectric constant of the substrate according to (3.1). If the dielectric constant is less than the dielectric constant of the surrounding substrate, then *guided propagation should not be possible*! We may see this by examining Eq. (2.2), where the cutoff frequency of a dielectric waveguide becomes imaginary when the dielectric constant of the dielectric becomes less than the surrounding material, in this case, air. This leads us to believe that a certain effective dielectric constant that is unexpected may exist. Of course, we have excluded unguided propagation such as those due to parallel-plate waveguides.

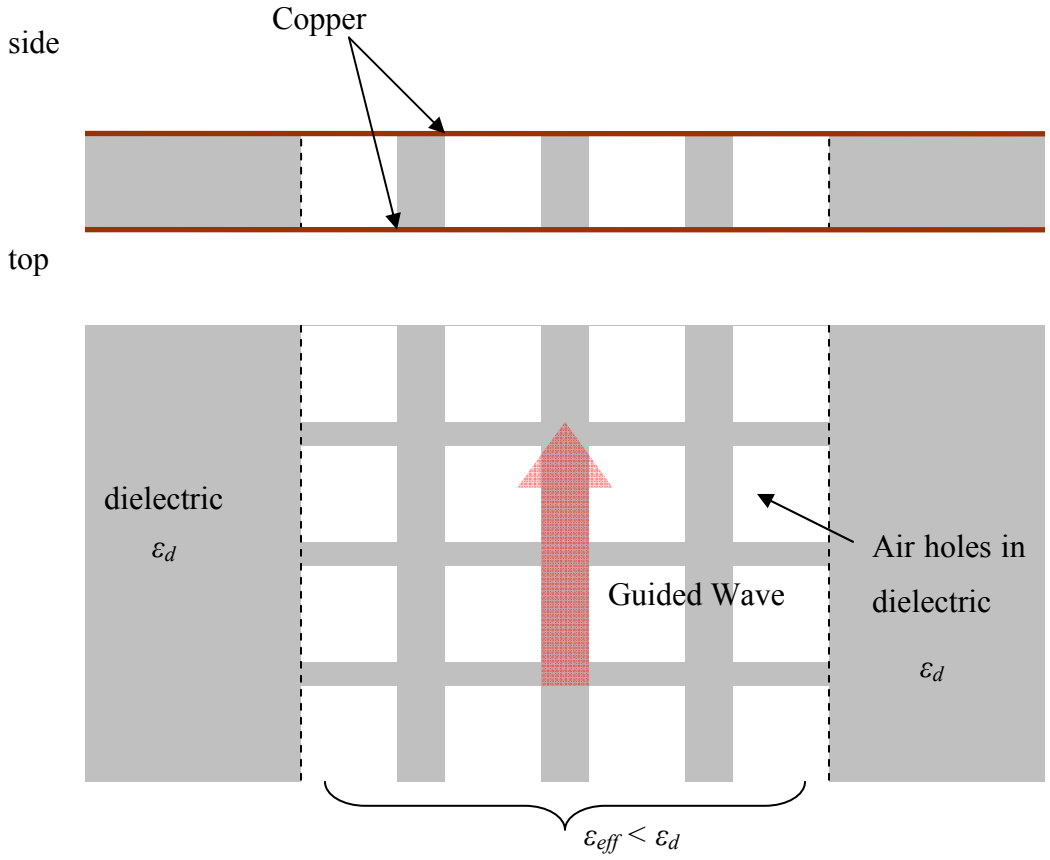

Fig. 3.1 An Electromagnetic Band Pass (EBP) waveguide.

The EBP structure has been simulated and is shown in Fig. 3.2, as discussed in [38], except with square holes instead of circular holes.

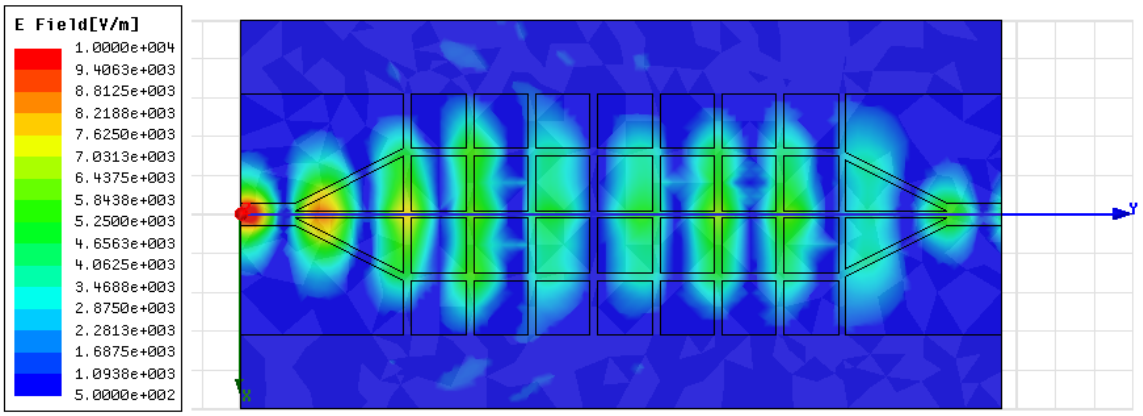

Fig. 3.2 An EBP Waveguide for microwave frequencies. Square holes are drilled within the substrate, where propagation may occur within the holes instead of within the solid substrate. The structure acts as a Band Pass structure within a certain bandwidth.

Some of the energy is lost due to leakage as shown in Fig 3.2. The leakage appears as electric fields outside the EBP waveguide in the center where the holes exist. A model for the propagation through this structure is discussed in the next chapter.

3.2.2 A Via-Less EBP Horn Antenna

Before the theoretical analysis of the previous structure is investigated in the next chapter, one application of the structure in the form of an EBP-fed planar horn antenna will be discussed [39]. Since no metallic vias are required, this has the obvious advantage that simplicity is maintained while cost is lowered. In a typical metallic via process, a hole is drilled as a first step, and then must be electro-plated or riveted in a second step. Reducing the number of steps in any manufacturing process decreases possibilities for manufacturing defects, lowers final production cost, decreases equipment cost, and decreases material costs, thereby increasing profits.

In this theoretical design, an EBP structure is used as a medium to guide an electromagnetic wave within the substrate. Details of how this is possible are discussed in Chapter 4. The structure consists of a series of periodic holes drilled within the substrate that is bounded on the top and bottom by metallic layers, where no metallic via has been used as shown in Fig. 3.3. The EBP structure is in turn excited with a

microstrip line, where a new microstrip to dielectric waveguide transition is discussed in detail in Chapter 5. The resulting antenna is only 1.575 mm thick and achieves a 7.2 dBi peak gain. Even though the performance of this structure has not been fully optimized, this example demonstrates concepts to be discussed in this thesis.

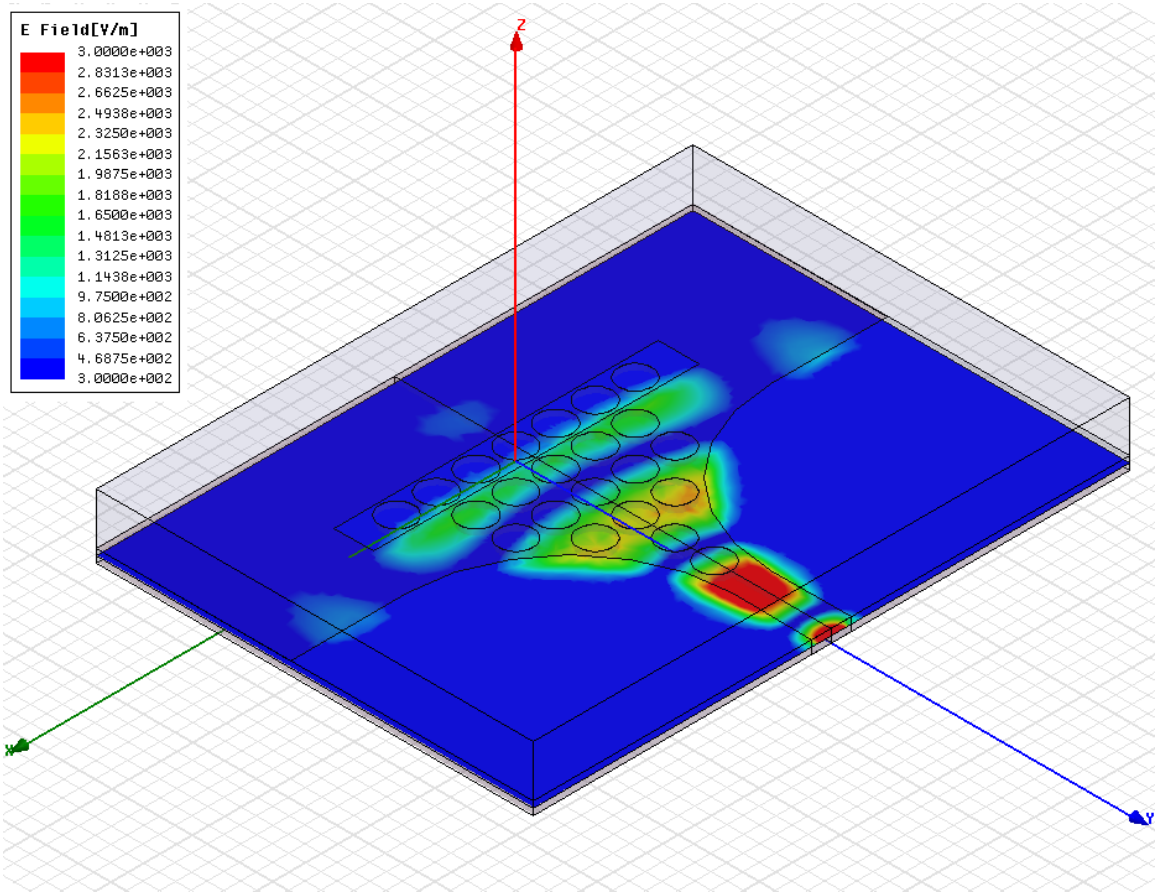

Fig. 3.3 A Via-less EBP horn antenna. A microstrip line transitions into an EBP structure, which feeds a single radiating slot.

3.2.3 The H-guide: A Wideband Dielectric Slab Waveguide Bounded by Metallic Plates

In this section we present simulated results for an H-guide that is essentially a wideband dielectric slab waveguide bounded by metallic plates. By applying concepts in Appendices A and B, we have simulated the structure shown in Fig. 3.4. The substrate consists of Rogers 5880 with a dielectric constant of 2.2 and thickness of 1.575 mm,

bounded on the top and bottom by metallic plates. A single, thin column of dielectric 10.0 mm wide guides the wave and is surrounded by two larger columns of air. The structure is 100 mm by 100 mm in the x-y plane. The columns of air were assumed infinitely wide in the analysis in Appendix B. In this case, their finite width limits the lower frequency response of the TE_{00} mode. The cutoff frequency for the TE_{10} mode is 13.7 GHz, as found in Appendix B.

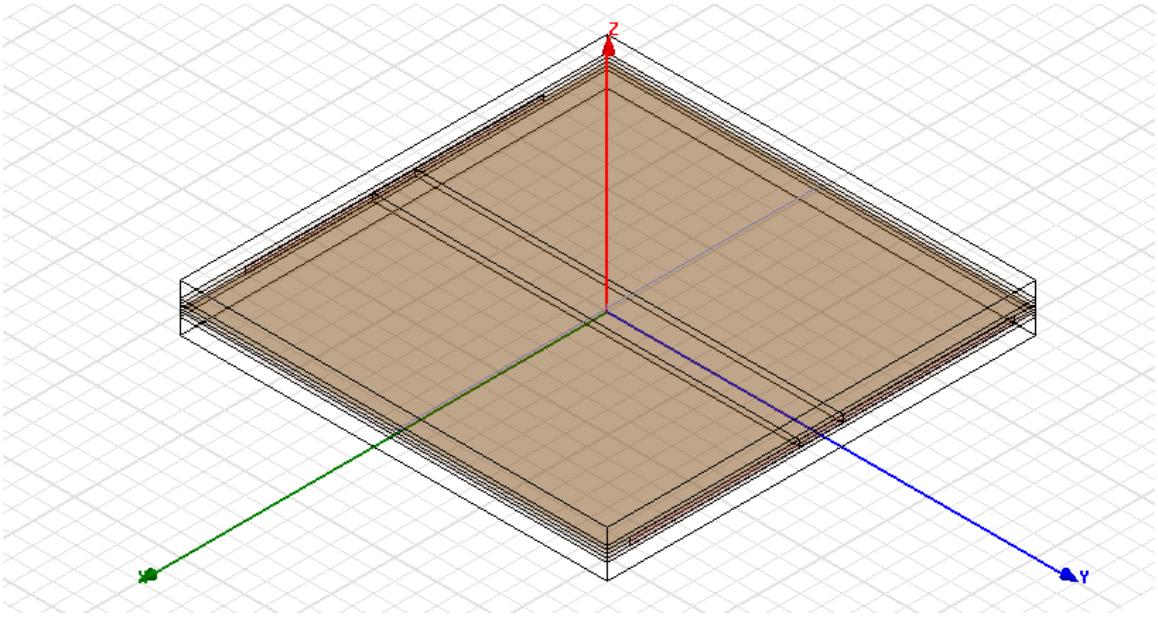

Fig. 3.4 Structure for a wideband dielectric slab waveguide (H-guide) bounded by copper plates.

It is possible to form an array of dielectric slabs within the metallic plates, or H-guides, to form a wideband EBP structure, where each column is parasitically coupled to the other. The single H-guide, however, will be considered in the following sections.

If copper losses are taken into account, the total loss through a structure that is 10 cm long does not change significantly. In Fig. 3.5, the transmission parameters through the 100 cm long structure with a 10 mm wide Rogers 5880 H-guide is plotted. The cutoff frequency for the TE_{10} mode (from Eq. (2.2)) is 13.7 GHz, which is marked approximately with a dotted line.

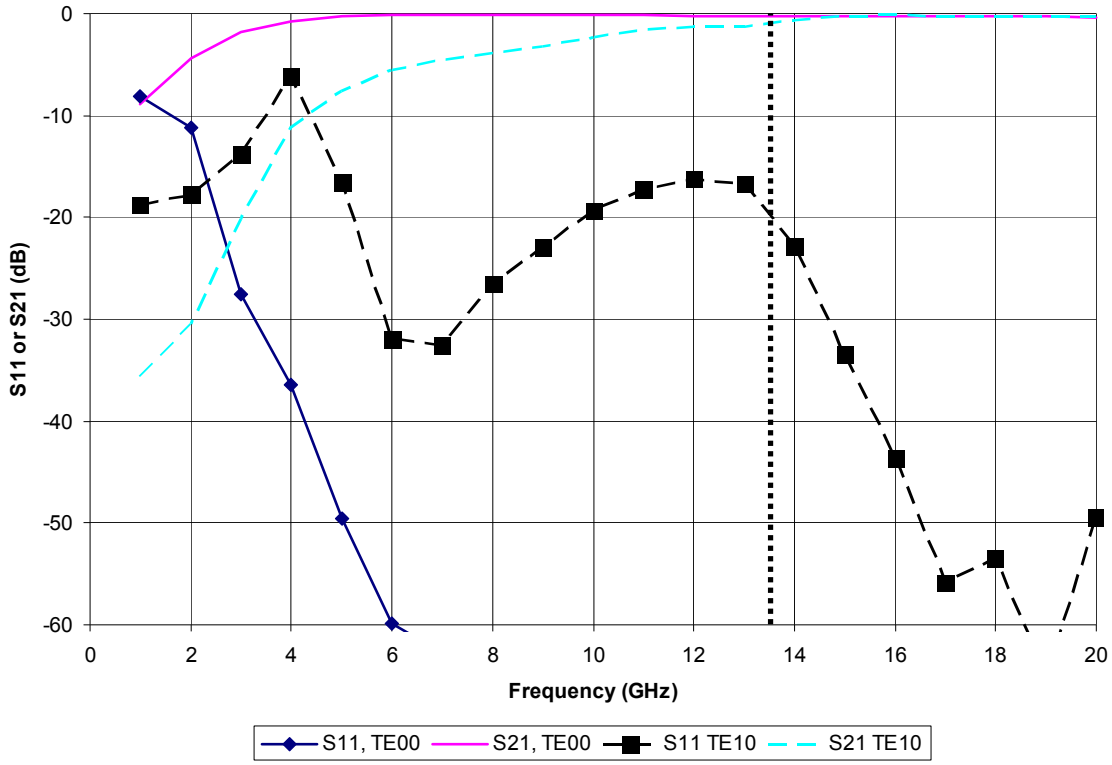

Fig 3.5 Simulated S Parameters for a wideband dielectric slab waveguide (H-guide) bounded by **copper** metallic plates S11 and S12 are plotted for the fundamental mode, TE_{00}, and first odd mode, TE_{10}.

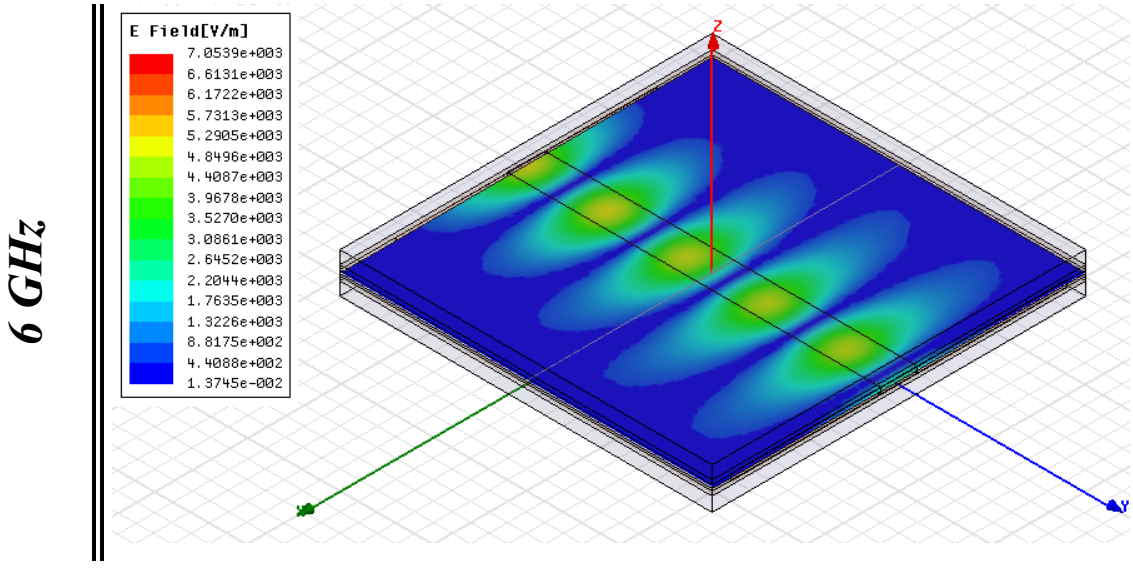

9 GHz

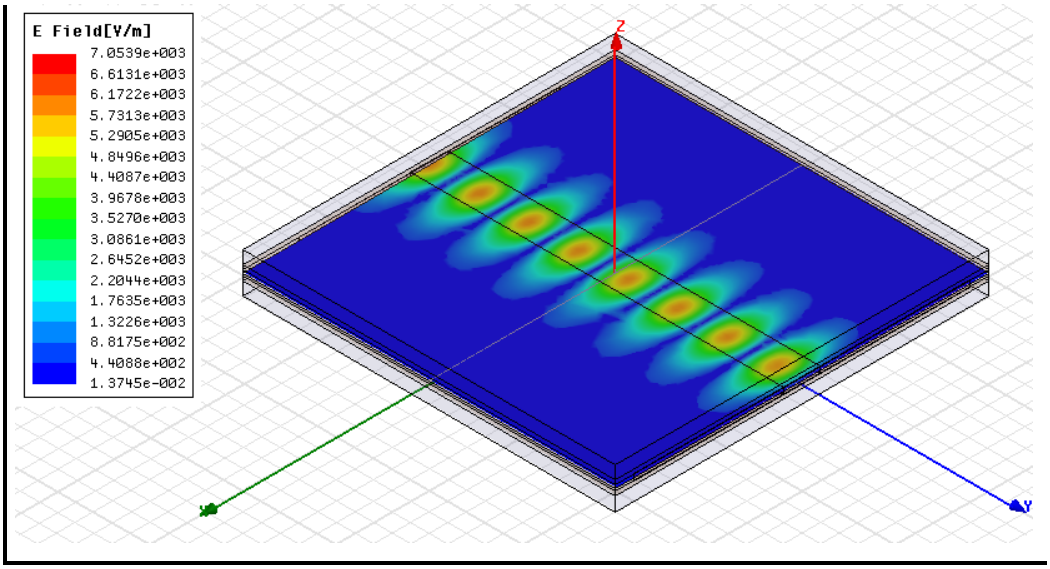

12 GHz

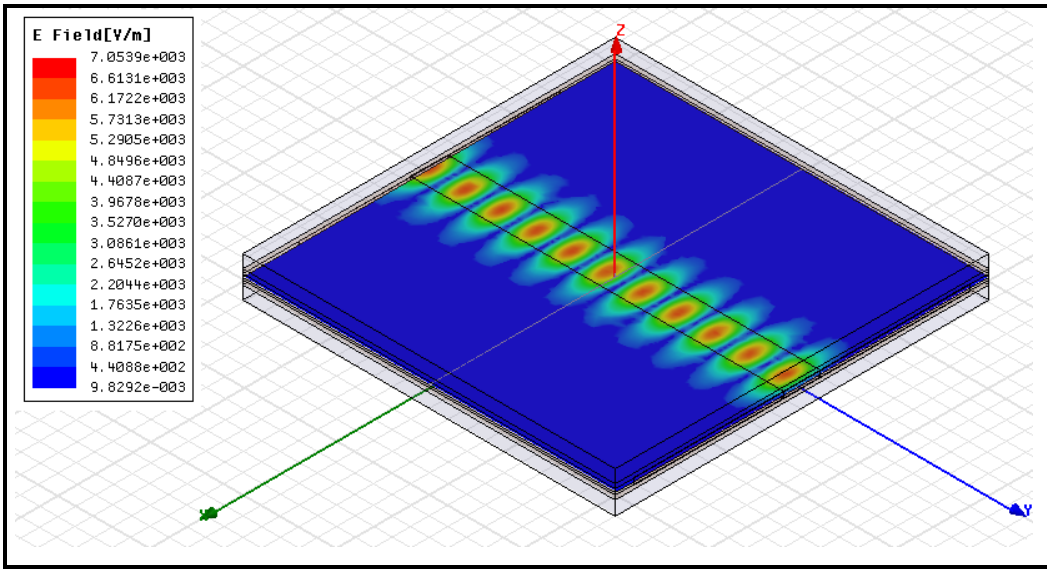

15 GHz

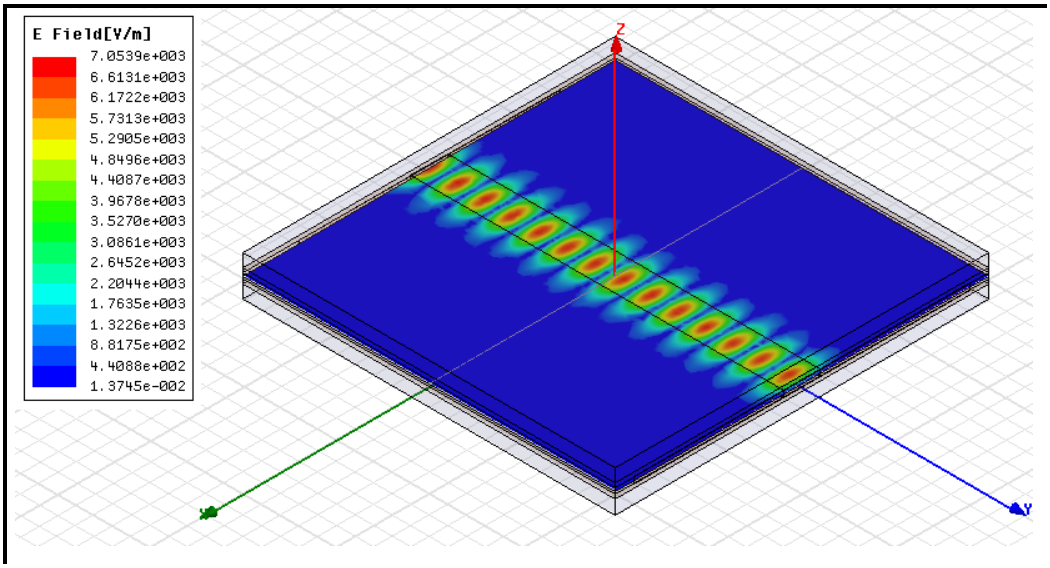

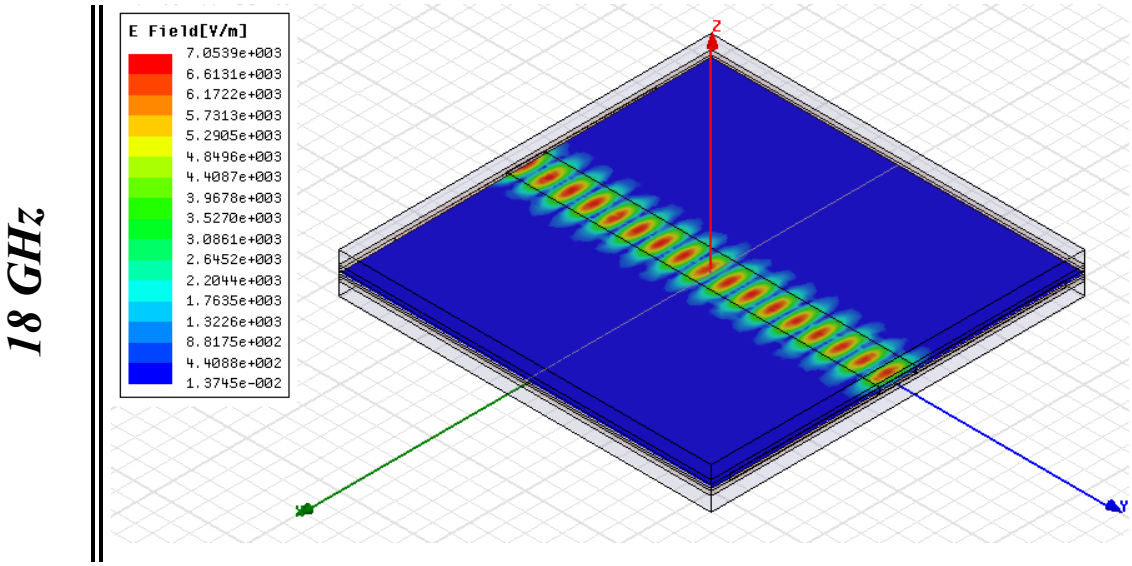

Fig. 3.6 Magnitude of the electric field within the H-guide structure at 6, 9, 12, 15, and 18 GHz.

In Fig. 3.6, the magnitude of the electric field within the H-guide is shown at different frequencies when the fundamental mode is excited with a waveport.

3.3 Summary

In this chapter, several waveguides have been presented in the form of simulated results. An explanation for the propagation through a periodic "Electromagnetic Band Pass" (EBP) structure is presented in the next chapter, Chapter 4. Measured results for the propagation through the H-guide structure are presented in Chapter 5, since they require microstrip to H-guide transitions for measurements. An optimized horn antenna structure, whose performance is vastly improved as compared to the planar horn structure discussed in this chapter, is discussed in Chapter 6.

Chapter 4: Analysis of a Square Periodic H-guide

In this chapter, a new method for the analysis of periodic structures is presented. This method allows for "back of the envelope" designs, where in general, previous analysis methods require computer simulation or computer programming.

4.1 Introduction

The H-guide [2], and later the Non-Radiative Dielectric (NRD) [40], has been the subject of recent work such as leaky wave antennas [41], or mm-wave circuits [42]. Since, the H-guide is capable of supporting a lowest cutoff frequency of 0 Hz [43], the H-guide may be more appropriate for lower frequency applications than the NRD. The single-mode H-guide, however, is not limited to lower frequencies as we discuss applications up to 18 GHz in this section.

The dielectric Electromagnetic Band Gap (EBG) structures to be discussed in this chapter consist of a square lattice array of circular [44] or square shaped air holes drilled into a substrate, which are subsequently covered with infinitely large metallic ground planes. Such structures exhibit what is known as a band gap, or region of frequencies where propagation is not allowed, as illustrated in Fig. 4.1.

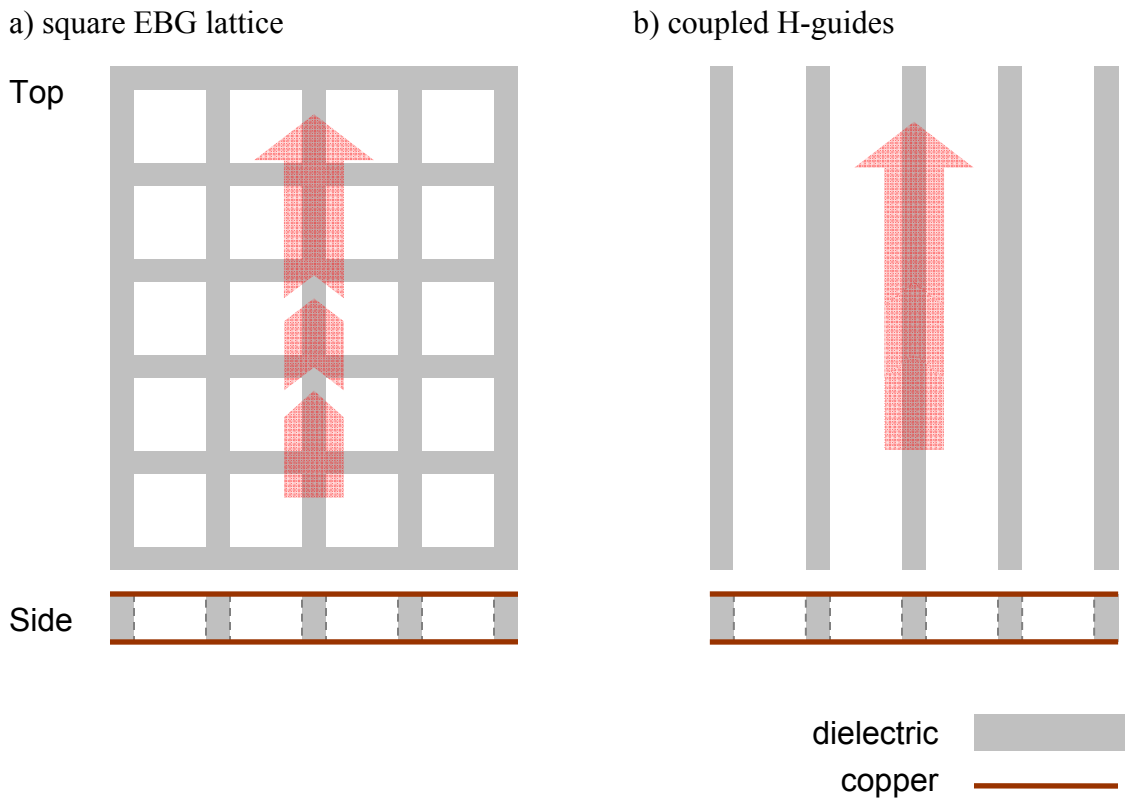

Fig. 4.1 (a) Typical square lattice EBG Structure embedded in a substrate. (b) coupled H-guide equivalent.

Typically, analyses of such structures is performed using a numerical simulator to obtain S-parameters for one period, then applying Floquet's theorem to find an effective propagation constant β through the lattice [44] [31]. When β is imaginary propagation is not allowed [15]. The method presented in this chapter allows the determination of "how much" energy is passed or blocked by a finite-length periodic structure, not simply an "on or off" condition. In addition, this method provides an accurate Fourier, or z-transform representation of dielectric periodic structures, which greatly simplifies the determination of the frequency response, or conversely, the design of a structure that meets a certain frequency response.

Square EBG structures, as shown in Fig. 4.1(a), can be thought of as multiple, coupled H-guides which pass through periodic vanes, as shown in Fig. 4.1(b). Such an analogy can be useful in determining transmission and reflection coefficients through the structure by use of a transmission line model. In addition, if the square periodic H-guide is operated

in the pass band region instead of the band gap region, a much larger bandwidth than typical band gap devices becomes available. Typical bandgap devices operating in their bandgap region have a bandwidth of roughly 20 to 30% [45], while the proposed structure in this chapter operates from 7.5 to 18 GHz in the pass band region.

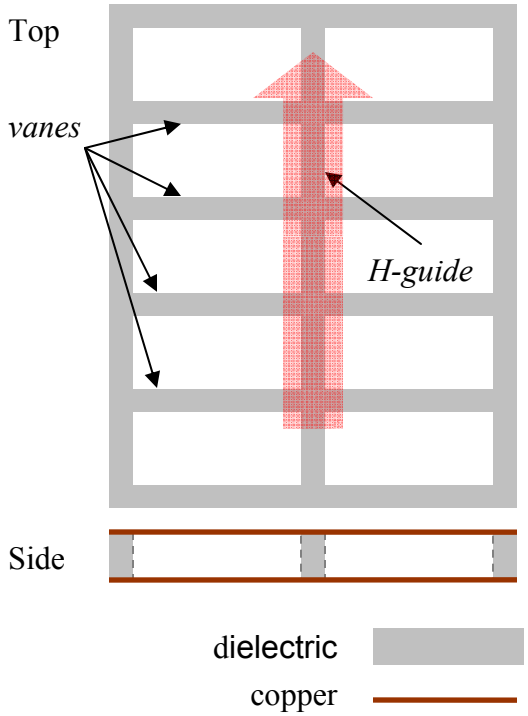

Fig. 4.2 A simplified square lattice EBG Structure with single H-guide.

The new configuration of the H-guide supported by periodic vanes, as shown in Fig. 4.2, is very similar to dielectric Electromagnetic Band Gap (EBG) structures since they both consist of a dielectric slab with periodic air gaps. A simple transmission line model and its validation for the S-parameter analysis of such a structure, using numerically simulated and measured results, are presented in the following sections. Preliminary simulated results have briefly been presented in abstract form in [46].

4.2 Wave Impedance and Guide Wavelength of the H-guide

To avoid ambiguity with different notations found in other references, the electric and magnetic fields in the TE_{00} mode, sometimes called the LSE_{00} or LSE_{01} mode are first

described. This is the dominant mode propagating in the structure since the width, *a*, of the dielectric is chosen to be thin enough to force a single-mode as shown in Fig. 4.3.

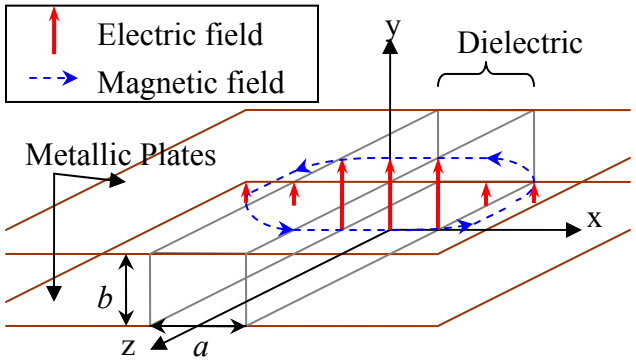

Fig. 4.3 The H-guide structure.

The fields for the odd potential (even) modes inside the dielectric are [10] [11] [40]

$$E_x = 0$$
$$E_y = \frac{1}{\varepsilon_d} A_d h_n \cos(h_n x) e^{-j\beta_g z} \tag{4.1}$$
$$E_z = 0$$

$$H_x = \frac{A_d h_n \beta_g}{\omega \mu_d \varepsilon_d} \cos(h_n x) e^{-j\beta_g z}$$
$$H_y = 0 \tag{4.2}$$
$$H_z = \frac{-jA_d}{\omega \mu_d \varepsilon_d} \left(\beta_d{}^2 - \beta_g{}^2\right) \sin(h_n x) e^{-j\beta_g z}$$

The fields outside the dielectric, for $x > a/2$ are,

$$E_x = 0$$
$$E_y = -\frac{A_o p}{\varepsilon_o} e^{-px} e^{-j\beta_g z} \tag{4.3}$$
$$E_z = 0$$

$$H_x = \frac{A_o p \beta_g}{\omega \mu_o \varepsilon_o} e^{-px} e^{-j\beta_g z}$$
$$H_y = 0 \tag{4.4}$$
$$H_z = \frac{-jA_o}{\omega \mu_o \varepsilon_o} \left(\beta_o{}^2 - \beta_g{}^2\right) e^{-px} e^{-j\beta_g z}$$

The wave impedance is defined using the electric and magnetic fields that are perpendicular to the direction of propagation, as in the case for a plane wave travelling in free space, then, inside air portion of the H-guide

$$Z_g = \frac{E_y}{-H_x} = \frac{\omega\mu_o}{\beta_g} \tag{4.5}$$

The wave impedance for a wave inside a vane, where p_d represents the attenuation constant in the x-direction within the vane, is given by

$$Z_v = \frac{E_y}{-H_x} = \frac{\omega\mu_d}{\beta_v} \tag{4.6}$$

The guide wavelength for even TE modes in the H-guide can be found by solving the following equations for h_n, the n^{th} solution to the equations [40] [11],

$$pa = h_n a \tan\frac{h_n a}{2}$$

$$(pa)^2 + (h_n a)^2 = (\varepsilon_r - 1)(k_o a)^2 \tag{4.7}$$

and where variable "*a*" is the width of the dielectric as shown in Fig. 4.3.

h_n is then substituted into the characteristic equation inside the dielectric to find λ_g, the guide wavelength for the n^{th} solution is

$$\beta_g{}^2 = \varepsilon_r k_o{}^2 - h_n{}^2 \tag{4.8}$$

$$where\ \ k_o = \frac{2\pi}{\lambda_o},\ \ \beta_g = \frac{2\pi}{\lambda_g}$$

4.3 Analysis Model for a Single Vane

In this section, we show that we may apply the theory of small reflections [10] [11], which typically applies to a plane wave incident on a multiple dielectric slab layer interface. This analysis takes multiple reflections within the vanes into account; however, it does not consider the excitation of higher order, evanescent modes in the H-guide that are excited by discontinuities, or leakage from the H-guide into each vane as shown in Fig. 4.4. These higher order modes are very small when the width of the vanes "*d*" is small compared to the guide wavelength. In addition, since the width of the vanes "*d*" is small, the reflected wave coming back from a vane appears to come from a single

interface, instead of from the H-guide-to-vane-to-H-guide interface. Finally, a third assumption is that the "mutual coupling" between vanes is small, meaning the air spacing is greater than the distance d so that the structure does not appear to be a large parallel plate waveguide.

Despite these assumptions, a very good approximation to the frequency response below the first resonant frequency may still be calculated for a single-mode H-guide with thin periodic vanes. The goal here is to obtain an approximation of the reflected wave without the need for computer simulation, or piecewise integration, not to obtain an exact result.

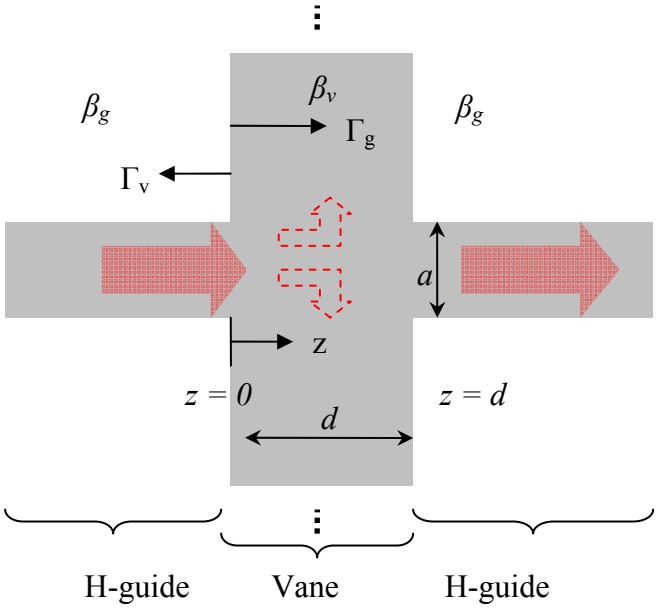

Fig. 4.4. Reflection from a single vane. Leakage from the H-guide is shown with dotted arrows.

Assume that a wave travelling through the periodic structure in Fig. 4.2 has a wave velocity of v_g within sections between vanes, and slows to a velocity of v_v within the vanes themselves, where $v = \omega / \beta$. The wave velocity within the vanes is then assumed to be the same as in a parallel plate waveguide. The reflection from a single vane as shown in Fig. 4.4 can then be approximated, where Γ_{gv} is equal to $-\Gamma_{vg}$. For a good dielectric (lossless), using Eq. (4.5) and (4.6) where $\mu_v = \mu_0$, we can approximate the reflection coefficient to be

$$\Gamma_{vg} = \frac{Z_v - Z_g}{Z_v + Z_g} = \frac{\beta_g - \beta_v}{\beta_g + \beta_v} \qquad \beta_v = \omega\sqrt{\mu\varepsilon}$$
$$\Gamma_{in} = \frac{\Gamma_{vg} + \Gamma_{gv} e^{-j2\beta_v d}}{1 + \Gamma_{vg}\Gamma_{gv} e^{-j2\beta_v d}} = \frac{\Gamma_{vg}\left(1 - e^{-j2\beta_v d}\right)}{1 - \Gamma_{vg}^{\ 2} e^{-j2\beta_v d}} \quad where \quad \beta_g = \frac{2\pi}{\lambda_g} \tag{4.9}$$

λ_g is found by solving Eq. (4.7) and (5.8) [40] [11]. Notice that when distance d is small, the input reflection approaches 0, as expected. This structure can be simulated using wave ports in HFSS as shown in Fig. 4.5, where leakage from into the vanes is shown in Fig. 4.6.

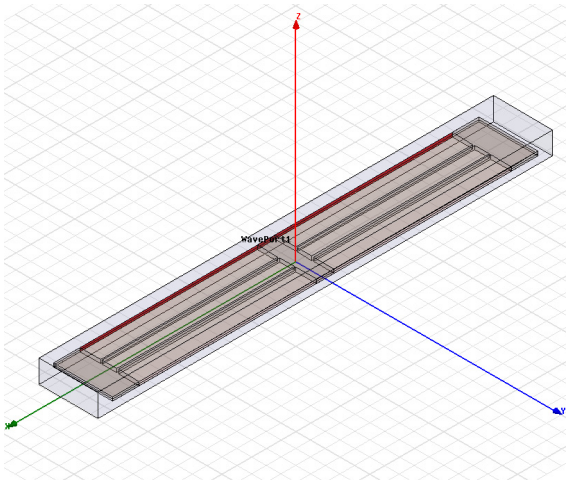

Fig 4.5 Model vs HFSS simulation for double vanes in 50 mil thick Rogers 6006. The H-guide is 6 mm wide, and the vane is 0.5 and 1.0 mm. A finite structure is simulated, where the airbox surround entire structure with air gaps on the sides of the structure. *a* = 6 mm, *s* = 5 mm, *d* = 0.5 mm. Rogers 6006, ε_r = 6, *h* = 1.27 mm.

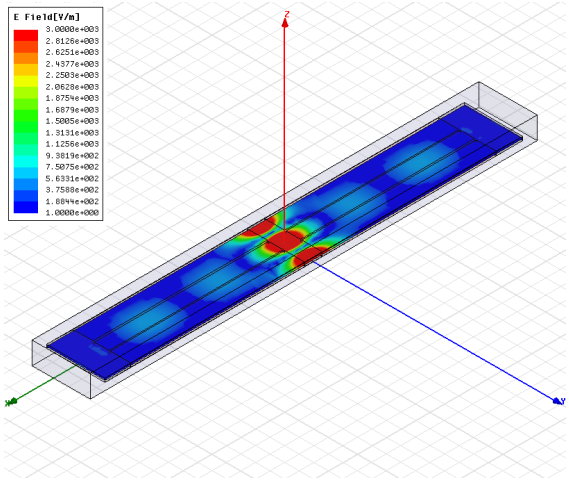

Fig 4.6 Leakage from the main H-guide into the vanes is clearly visible with exaggerated scaling.

An alternate view of Eq. (4.9) is that the single vane can be modeled as a very wide H-guide, as shown in Fig. 4.7. The wave velocity in a very wide H-guide approaches the same wave velocity as in a parallel plate waveguide. It is easier and faster to calculate the wave velocity in a parallel plate waveguide as opposed to a second very wide H-guide, therefore the parallel plate waveguide model is used in the following sections.

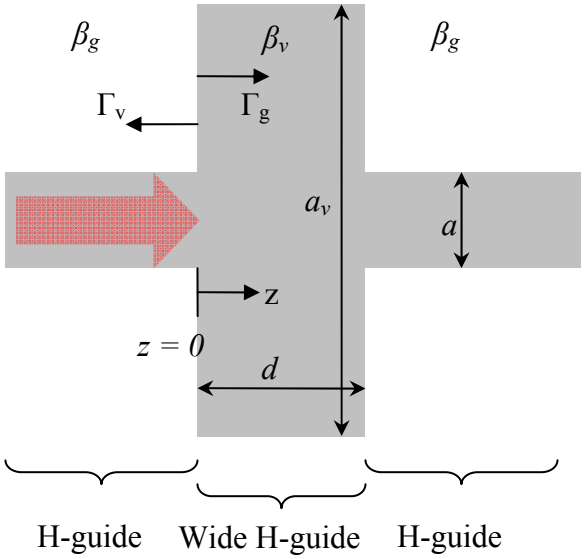

Fig. 4.7 Alternative model for finding the wave velocity within the vanes. Dimension "*a*" is the width of the H-guide, while dimension "a_v" is the width of the wide H-guide section, where "a_v" becomes large.

For a more accurate result, it is possible to use a numerical software simulation for the single vane, and then substitute these results into the following sections. For the sake of presenting a complete mathematical model, however, the method presented in this section is used in the following sections.

4.4 Reflection from Double Vanes

To model the reflection from two vanes, consider a power-corrected multiple reflection model, where we use a power transmission method to find the power lost as the wave travels through the structure, whose advantages will be clear in the following discussion. We start by labeling each region between vanes as regions 1, 2 and 3, as shown in Fig. 4.8. Consider the transmission from Region 1 to inside the vane at $z = 0$ as illustrated in

Fig. 4.8. The first part of the reflection at $z = 0$ is given by Γ_{21}, taking multiple reflections within the vane into account. The magnitude of the power transmitted into the first vane at $z = 0$ is proportional to

$$S_{v1} = \left(1 - |\Gamma_{21}|^2\right)$$
$$\sqrt{S_{v1}} \propto \sqrt{1 - |\Gamma_{21}|^2} \tag{4.10}$$

where Γ_{21} was given by Eq (4.9).

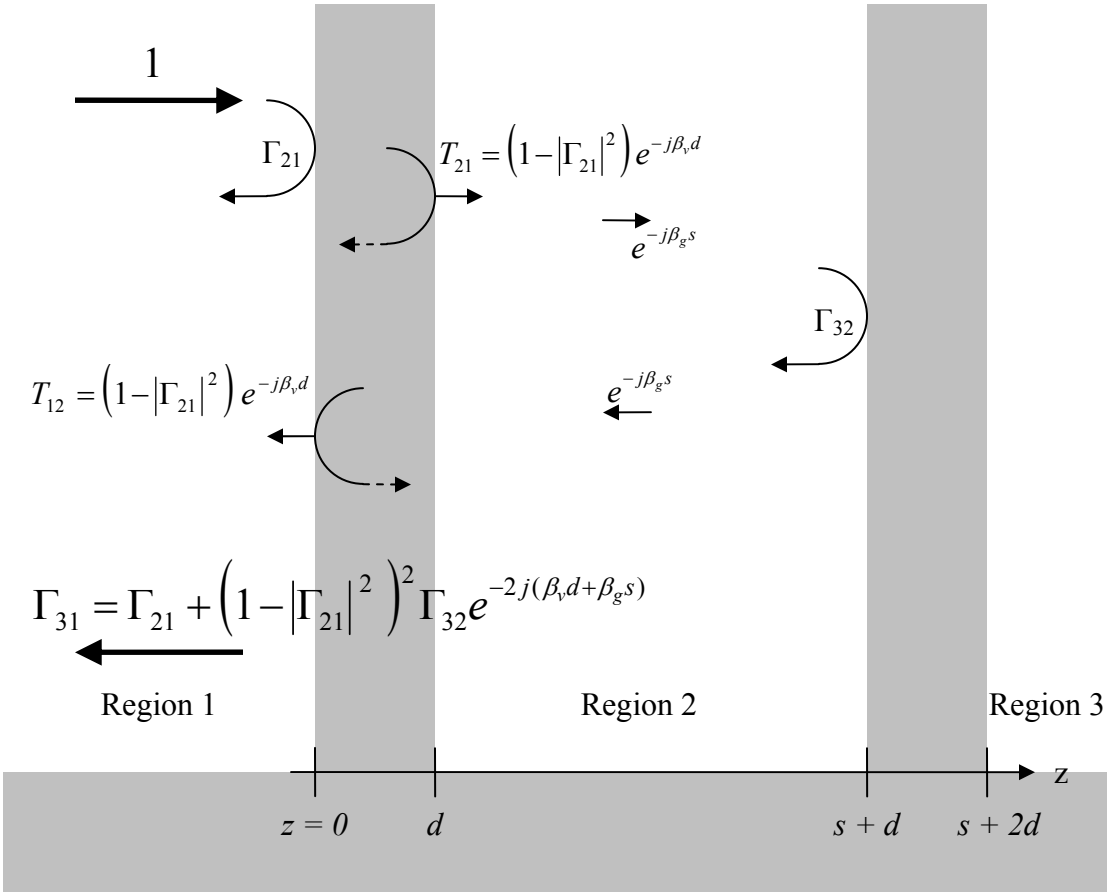

Fig. 4.8 First order power-corrected reflection model for double vanes.

Now, consider the transmission from the vane back into Region 2 at $z = d$. The wave experiences a reflection coefficient equal to $-\Gamma_{21}$; however the magnitude of the power transmitted is again given by

$$S_{1v} \propto \left(1 - |\Gamma_{21}|^2\right)$$
$$\sqrt{S_{1v}} \propto \sqrt{1 - |\Gamma_{21}|^2} \tag{4.11}$$

The transmission coefficient from Region 1 to Region 2 (from $z = 0$ to $z = d$) is then given by

$$T_{21} = \left(1 - |\Gamma_{21}|^2\right) e^{-j\beta_v d} \tag{4.12}$$

where the phase shift experienced by the wave as it travels from $z = 0$ to $z = d$ has been added. As the wave travels from $z = d$ to $z = d + s$, an additional phase shift of $e^{-j\beta_g s}$ is experienced, while a reflection of Γ_{32} occurs at the interface at $z = d + s$. In total, adding all the contributions, a first order approximation for the reflected wave can be expressed as

$$\Gamma_{31} = \Gamma_{21} + \left(1 - |\Gamma_{21}|^2\right)^2 \Gamma_{32} e^{-2j(\beta_v d + \beta_g s)} \tag{4.13}$$

A comparison of Eq. (4.13) to simulated results with HFSS [36] is shown in Fig. 4.9. The location of the nulls matches simulated results reasonable accurately, however, the magnitude of the reflection coefficient decreases at higher frequencies due to leakage at the discontinuities.

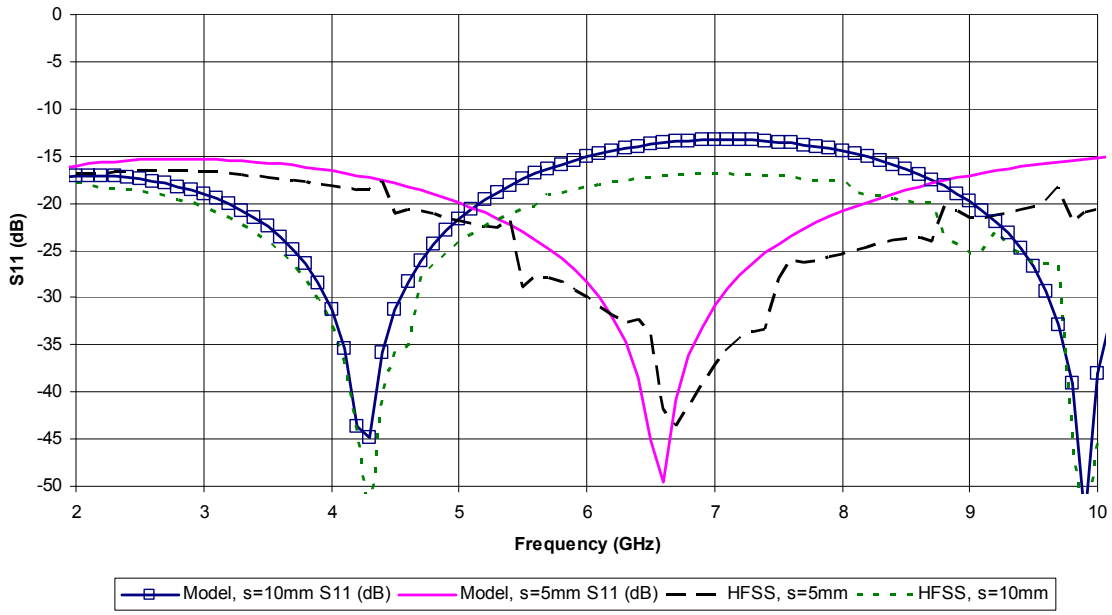

Fig. 4.9 Comparison of first order reflection model with HFSS simulation for double vanes. Substrate is 50 mil thick Rogers 6006. H-Guide is 6 mm wide, vanes are 1 mm wide and separated by a distance of 5 and 10 mm. Width of air gap on either side of the H-guide is 60 mm.

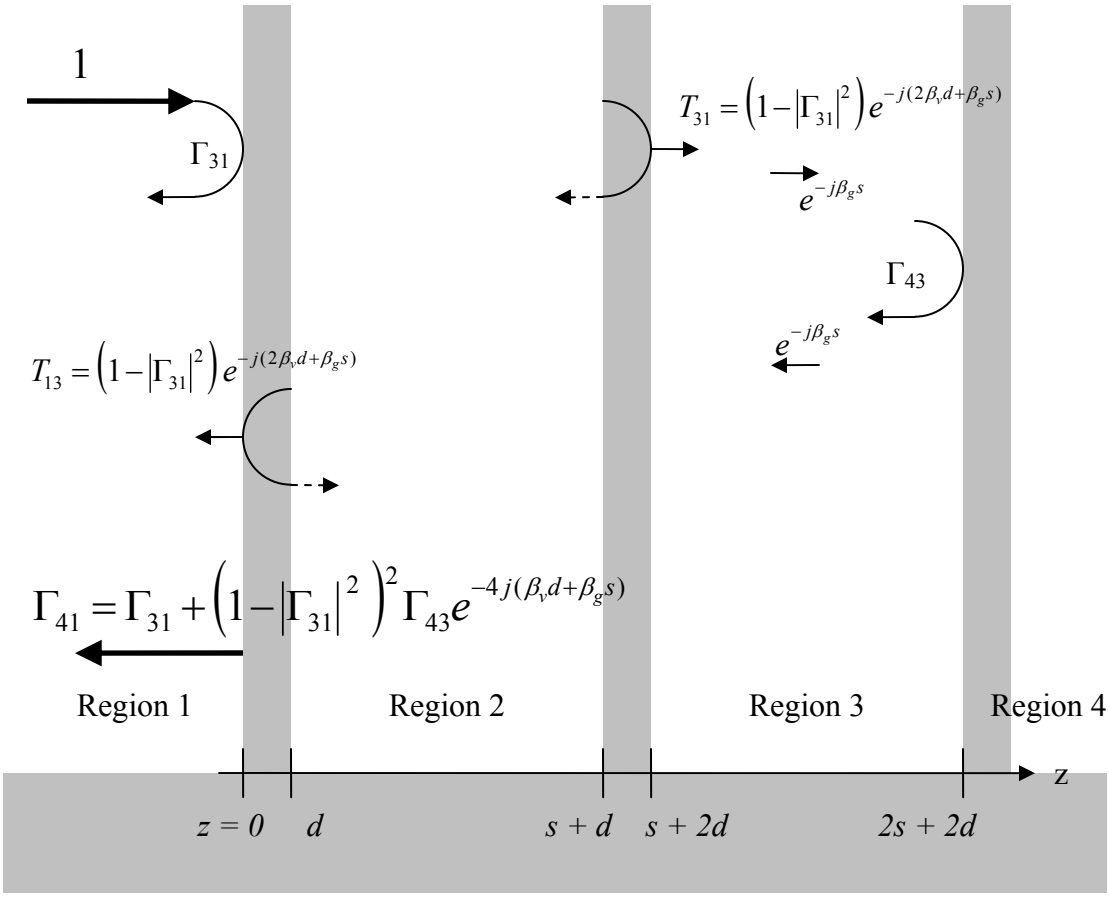

Fig. 4.10 First order power-corrected reflection model for three vanes.

4.5 Reflection from Multiple Vanes

This method can be cascaded to find the reflection from three or more vanes as shown in Fig. 4.10. This is where using a power-correction method is most beneficial since the magnitude and phase can be considered separately and so we may apply the method to multiple reflections using a cascaded system, without a significant increase in complexity. The reflection from 3 vanes will be given by

$$\Gamma_{41} = \Gamma_{31} + \left(1-\left|\Gamma_{31}\right|^2\right)^2 \Gamma_{43} e^{-2j(\beta_v(d_1+d_2)+\beta_g(s_1+s_2))} \tag{4.14}$$

The full equation can be written as

$$\Gamma_{41} = \Gamma_{21} + \left(1-\left|\Gamma_{21}\right|^2\right)^2 \Gamma_{32} e^{-2j(\beta_v d_1+\beta_g s_1)} + \left(1-\left|\Gamma_{31}\right|^2\right)^2 \Gamma_{43} e^{-2j(\beta_v(d_1+d_2)+\beta_g(s_1+s_2))} \tag{4.15}$$

Where,

$$\Gamma_{21} = \frac{\Gamma_{vg}\left(1-e^{-j2\beta_v d_1}\right)}{1-\Gamma_{vg}^{\ 2} e^{-j2\beta_v d_1}},\ \Gamma_{32} = \frac{\Gamma_{vg}\left(1-e^{-j2\beta_v d_2}\right)}{1-\Gamma_{vg}^{\ 2} e^{-j2\beta_v d_2}},\ \Gamma_{43} = \frac{\Gamma_{vg}\left(1-e^{-j2\beta_v d_3}\right)}{1-\Gamma_{vg}^{\ 2} e^{-j2\beta_v d_3}},\ \text{etc…} \tag{4.16}$$

This sum can be generalized for multiple vanes and written as a sum, when $d = d_1 = d_2 = \ldots = d_N$, and $s = s_1 = s_2 = s_3 = \ldots = s_N$, in the form

$$\Gamma_{N1} = \Gamma_{21} + \sum_{n=2}^{N} \left(1 - \left|\Gamma_{n1}\right|^2\right)^2 \Gamma_{(1+n)(n)} e^{-2j(n-1)(\beta_v d + \beta_g s)} \tag{4.17}$$

This may also be written in a compact form as

$$\Gamma_{N1} = \sum_{n=1}^{N} \left(1 - \left|\Gamma_{n1}\right|^2\right)^2 \Gamma_{(1+n)(n)} e^{-2j(n-1)(\beta_v d + \beta_g s)}$$
$$where \tag{4.18}$$
$$\Gamma_{11} = 0$$

The transmission line is assumed to be matched at the beginning and the end of the structure. This sum can easily be computed by considering that at each step, only the magnitude of the previously summed terms and simple squared and subtraction operations need to be performed. An alternate mathematical representation for Eq. (4.18) is discussed in Section 4.8.

The spacing required for a maximum reflection coefficient (resonance) can be solved by examining the phase term:

$$s = \frac{n\pi - \beta_v d}{\beta_g} \quad where\, n = 1,2,... \tag{4.19}$$

When the distance d is small, the spacing required approaches λ_g / 2 for maximum reflection, and λ_g / 4 for minimum reflection.

Neglecting the power lost through the structure by removing the bracketed term in (4.18), we obtain the same result as in [11], where $\theta = \beta_g d + \beta_v s$

$$\Gamma_{N1} = \sum_{n=1}^{N} \Gamma_{(1+n)(n)} e^{-2j(n-1)(\beta_v d + \beta_g s)} \tag{4.20}$$

Writing multiple reflections in the form of Eq. (4.20) has some computational advantages such as having fewer computational operations, being represented as a Fourier transform, used for filter designs as discussed in [11], or for doing *inverse operations*. When doing inverse operations, the nonlinearity of propagation constants β_g and β_v must be taken into account through techniques similar to pre-warping.

Eq. (4.20) is, however, not as precise as Eq. (4.18). This is because the magnitude of Eq. (4.20) may exceed 1 for a large number of reflections, since it does not take the power lost through the structure into account. Eq. (4.20) is the sum of first order reflected waves only as discussed in [11] and illustrated in Fig. 4.11.

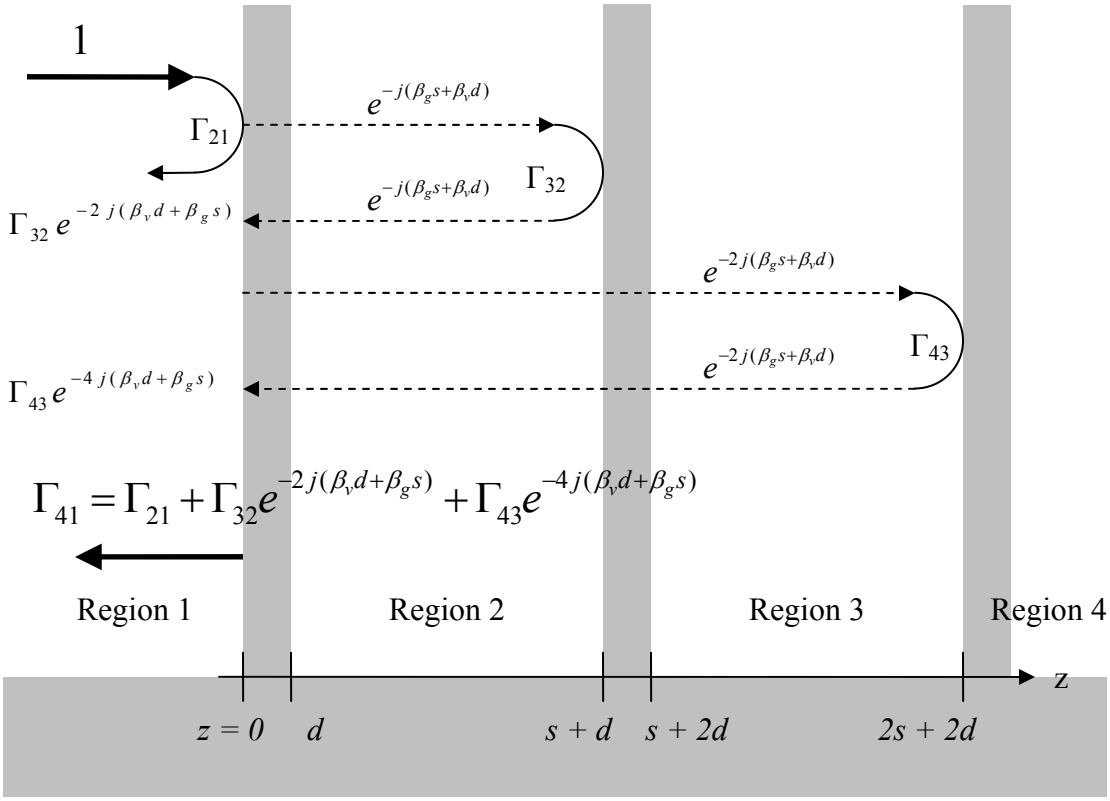

Fig. 4.11 First order non-power-corrected model for three vanes.

Once we know the reflection coefficient from Eq. (4.18), where $\Gamma < |1|$, we can then find the transmission coefficient as follows,

$$|T_{N1}| = 20\log_{10}\left(\sqrt{1-\left(10^{\Gamma_{N1}/20}\right)^2}\right)$$
$$|T_{N1}| = 10\log_{10}\left(1-\left(10^{\Gamma_{N1}/10}\right)\right) \tag{4.21}$$

A comparison of the reflection and transmission coefficients in Rogers 6006 substrate is shown in Fig. 4.12. A short parametric study using 6 vanes in Rogers 6006 is shown in Fig. 4.13, and Fig. 4.14 where a good agreement is shown between Eq. (4.18) and HFSS simulations.

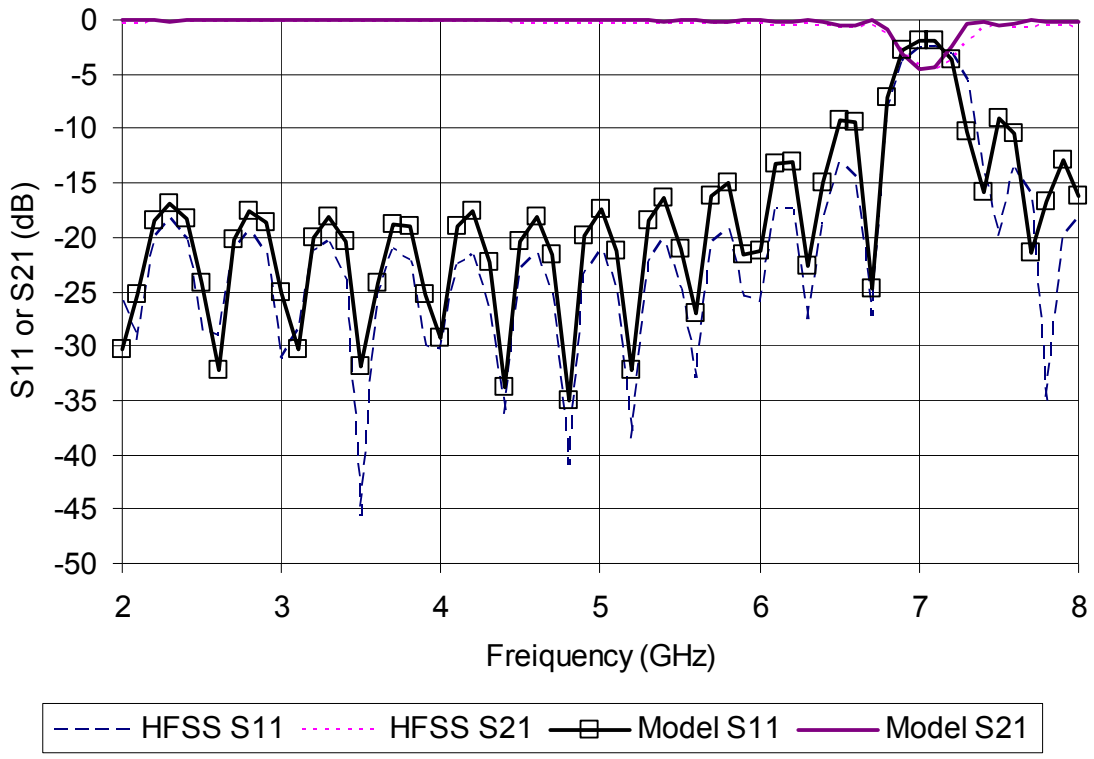

Fig. 4.12 Comparison of first order multiple reflection model with HFSS simulation for 15 vanes. Substrate is 50 mil thick Rogers 6006. H-Guide is 6 mm wide, vanes are 1 mm wide separated by a distance of 10.3 mm.

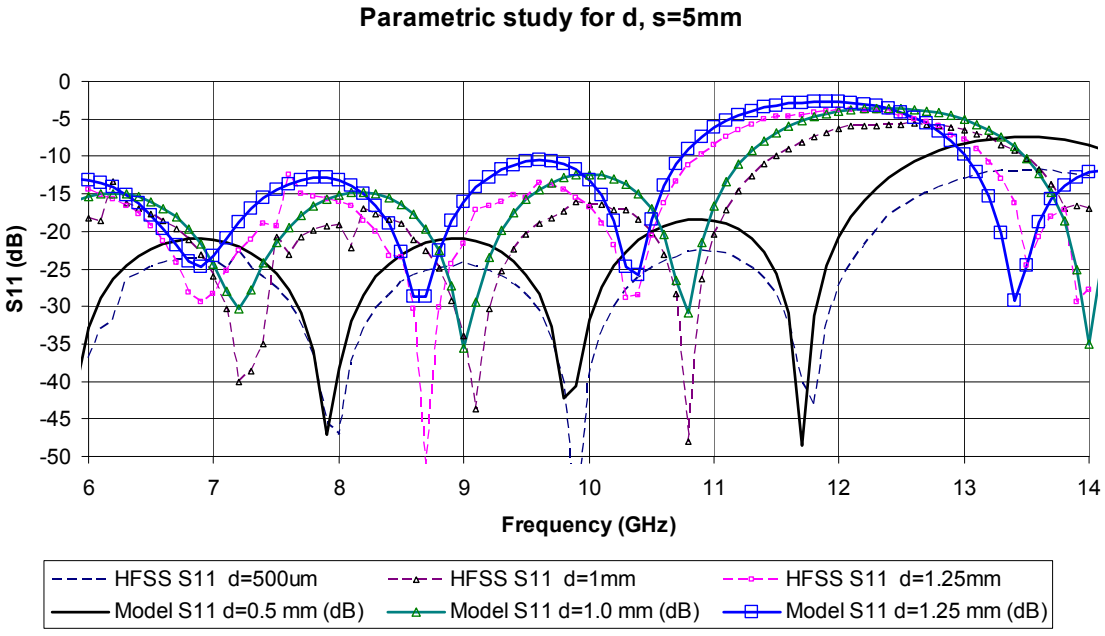

Fig. 4.13. Parametric study of variation in d with fixed spacing s = 5 mm. a = 4 mm, h = 1.27 mm.

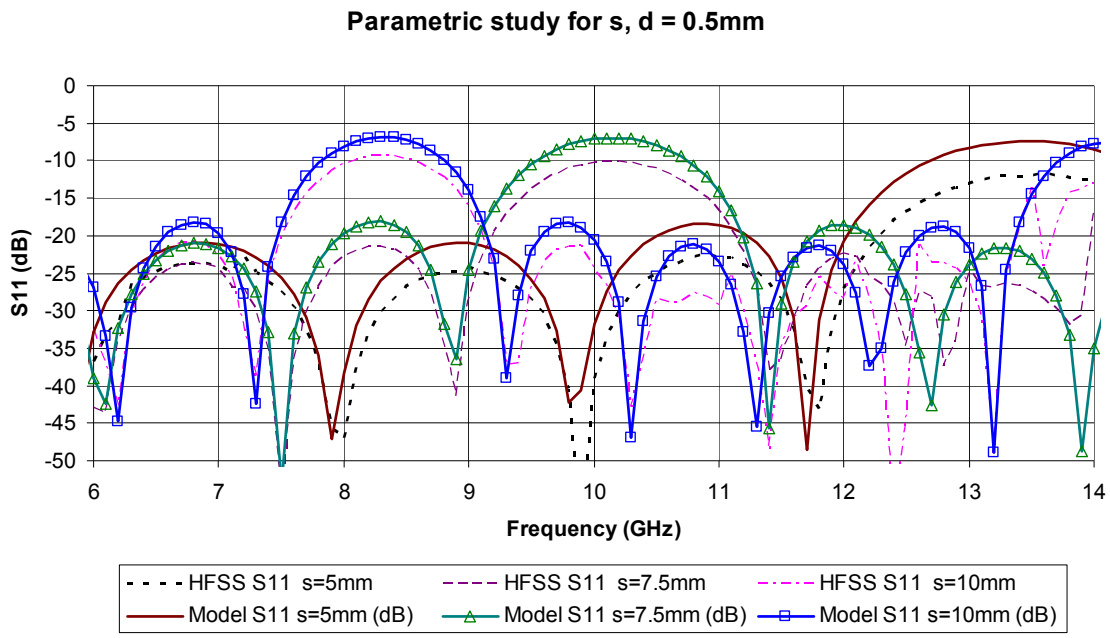

Fig. 4.14 Parametric study of variation in s with fixed spacing d = 0.5 mm. a = 4 mm, h = 1.27 mm.

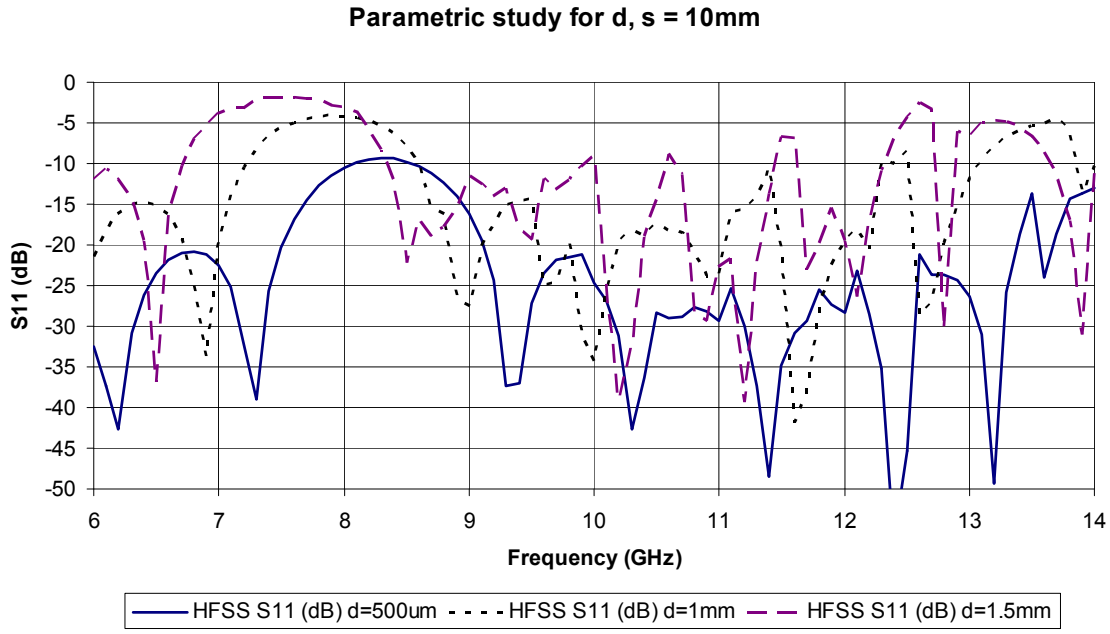

Fig. 4.15 HFSS Simulation results past the first resonant frequency. Spacing is fixed at 10 mm, and d is varied from 0.5 mm to 1.5 mm. Return loss is erratic past 8 to 9 GHz because multiple reflections begin to appear.

In Fig. 4.15, the HFSS simulation results past the first resonant frequency are shown. Since the simulated frequency response in this range is so erratic, this behavior is not of

interest. We further examine the accuracy of Eq. (4.18) in the next section at and below the first resonant frequency.

4.6 Design, Simulation, vs. Measurements

An H-guide made of a 10 mm wide section of dielectric is formed out of 62 mil (1.575 mm thick) Rogers 5880 (ε_r = 2.2). The waveguide is predominantly single-mode up to the cutoff frequency of the second mode (TE_{10}, m = 1, odd) at 13.7 GHz according to equations in [11] for an infinitely large dielectric slab waveguide. The guide wavelength, λ_g, for even TE modes within a single H-guide can be found by solving the equations for h_n, the n^{th} allowed even mode following procedures in [40] [11], using Eq. (4.7), where at 13.7 GHz, λ_g found to be equal to 16.4 mm. The guide wavelength as a function of frequency is plotted in Fig. 4.16.

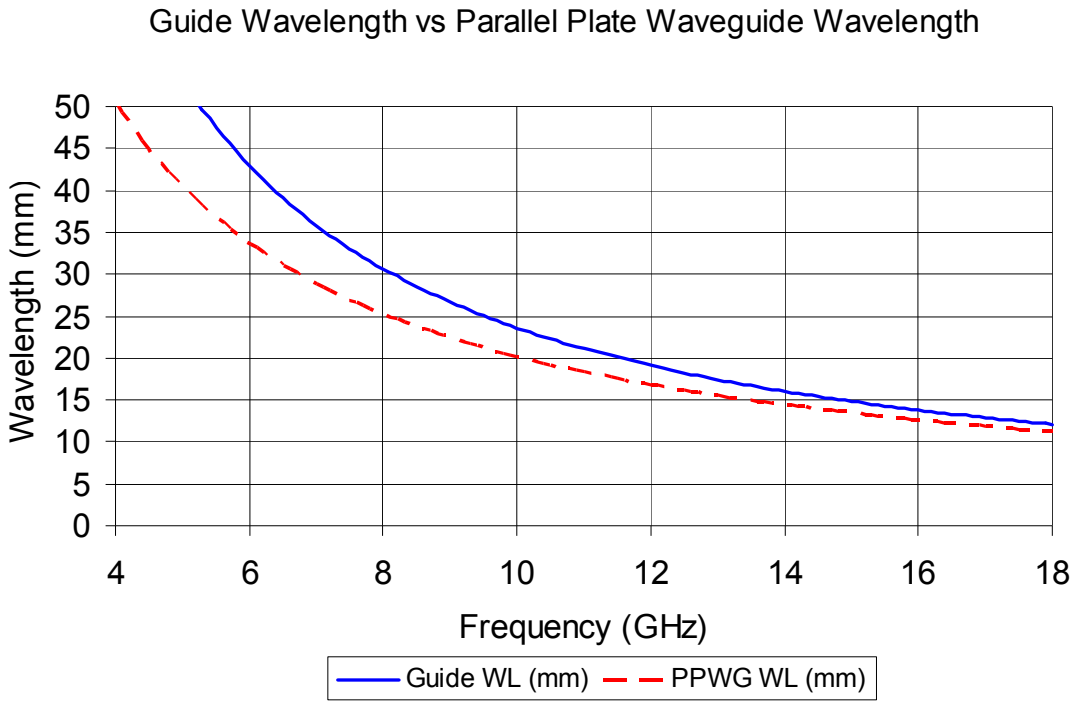

Fig. 4.16 Guide Wavelength for a 10 mm wide H-guide in Rogers 5880 as compared to a parallel plate waveguide wavelength in the same substrate.

Applying Eq. (4.19), for a vane thickness, d, of 1.0 mm, a required spacing, s, of 5.0 mm for a first resonant frequency at 18 GHz, the maximum desired frequency. The insertion loss is therefore relatively smooth from 8 to 18 GHz since no resonance occurs. The frequency response can be plotted using Eq. (4.18) and compared to a numerical

simulation using [36] as shown in Fig. 4.17. We observe a slight difference of approximately 0.1 GHz in resonant frequencies of the nulls between the model and simulated results.

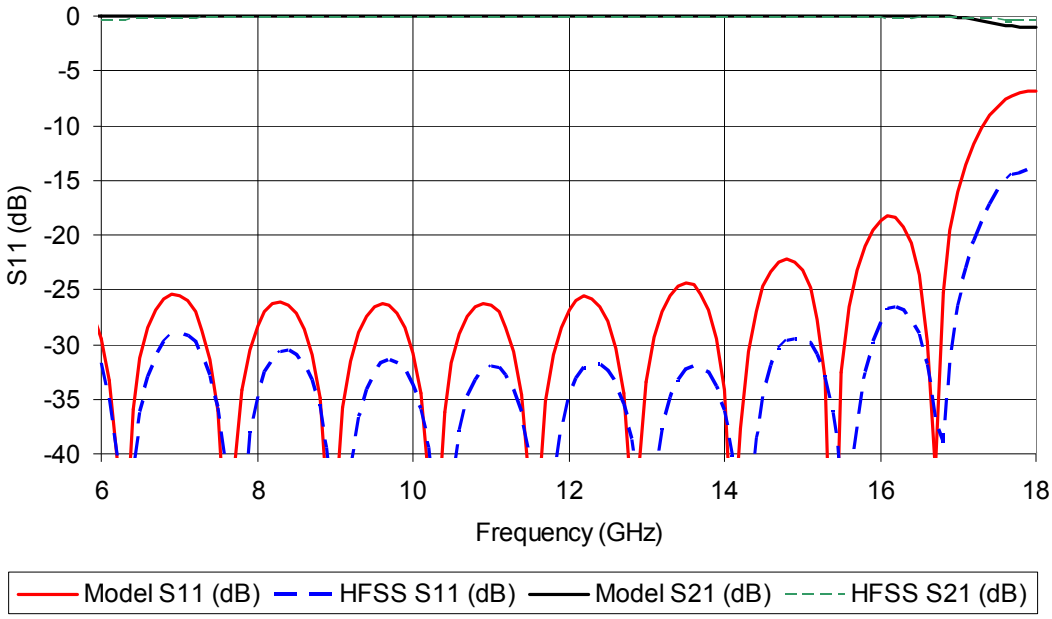

Fig. 4.17 Frequency response plotted using power-corrected multiple reflection model compared to simulated results using waveport-fed H-guides in HFSS [8] using the Rogers 5880 substrate. The substrate is Rogers 5880, the spacing between vanes is 5 mm, and each vane is 1 mm wide. In this case, side absorbing boundary conditions replace the dielectric side walls and the external air gap, which removes small ripples in the return loss.

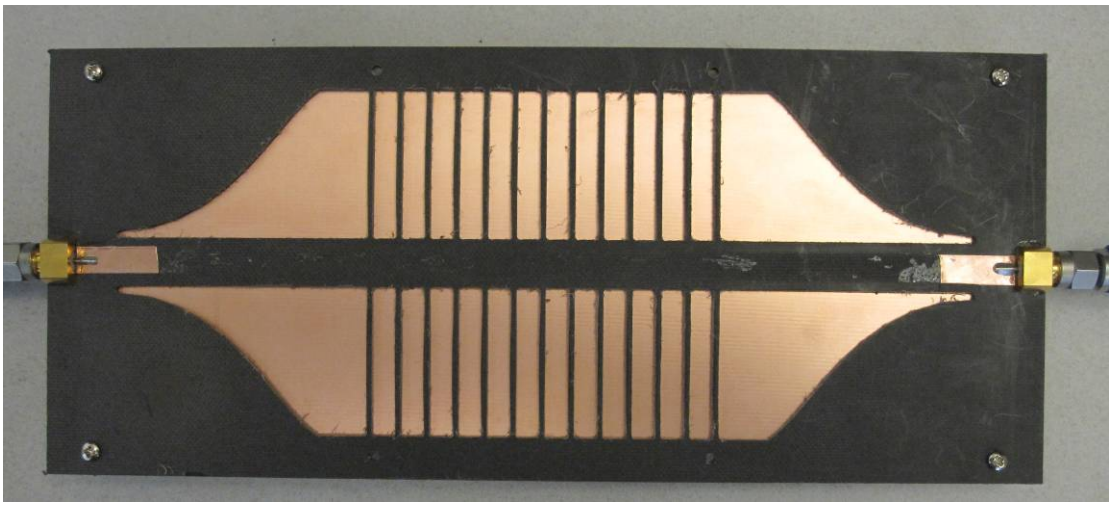

Fig. 4.18 Photograph of periodic section of prototype using the Rogers 5880 substrate just before the top metallic plate was replaced for testing. A microstrip line is made of copper tape with conductive adhesive and was used to measure the performance of the

coaxial to microstrip transitions. For the H-guide reading, the microstrip line section in the center was removed as shown.

A prototype of the structure shown in Fig. 4.18 was fabricated and measured. Eq. (4.18) and Eq. (4.21) are plotted against measured results as shown in Fig. 4.19. However, in this case, the relatively poor measured return loss (10 dB) above 10 GHz is due to a non-optimized coaxial to microstrip line transition as compared to [47]. The poor return loss less than 7 GHz is due to limitations in the microstrip to H-guide transition as can be seen by the loss in insertion loss and the increase in return loss in simulated results as shown in Fig. 4.19. The general trend, however, in the return loss can be seen, meaning there are no significant peaks in the return loss due to resonant frequencies until 18 GHz.

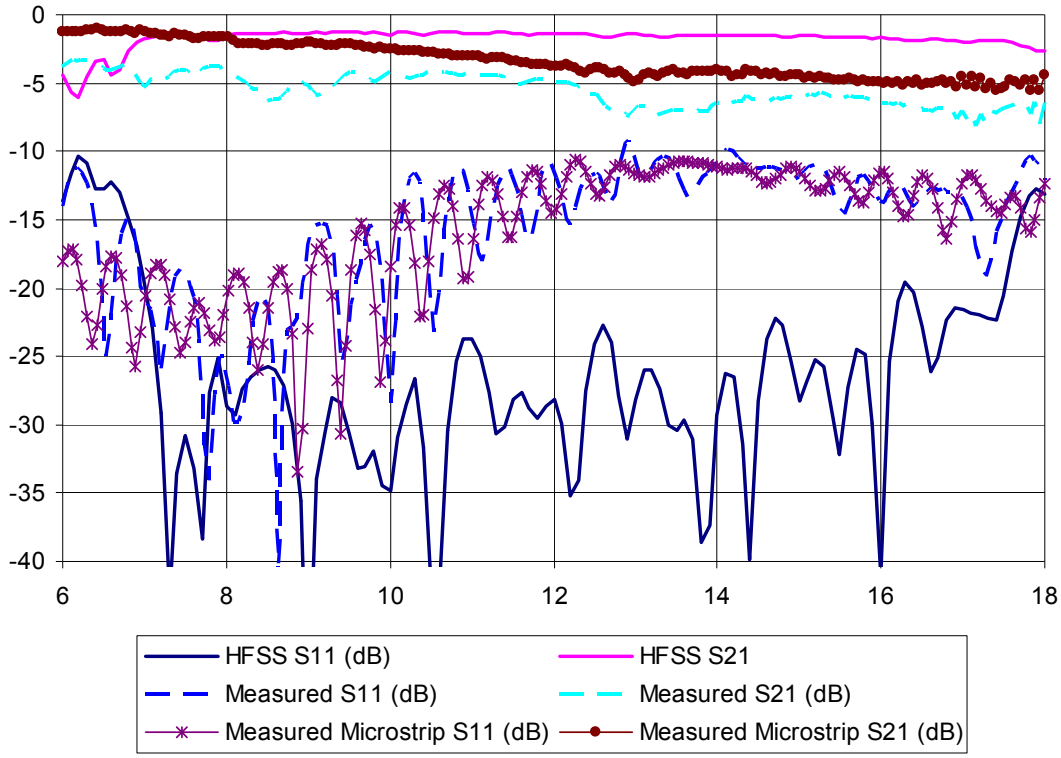

Fig. 4.19 Frequency response of the insertion and return loss of simulated results using microstrip to H-guide feeds in HFSS, compared to measured results using the Rogers 5880 substrate.

4.7 Arbitrary Spacing

In this section, the return loss of a structure with arbitrary spacing is presented. In this case, s_n corresponds to the n^{th} spacing between vanes according to Table 4.1. The

resulting comparison for one case is shown below in Fig. 4.20, which is the same case as shown in Fig. 4.12.

n	Case 1: Spacing, s_n in mm	Case 2: Spacing, s_n in mm
1	8	7
2	7	8
3	5	9
4	7	3
5	8	10

Table 4.1 Spacing Between Vanes

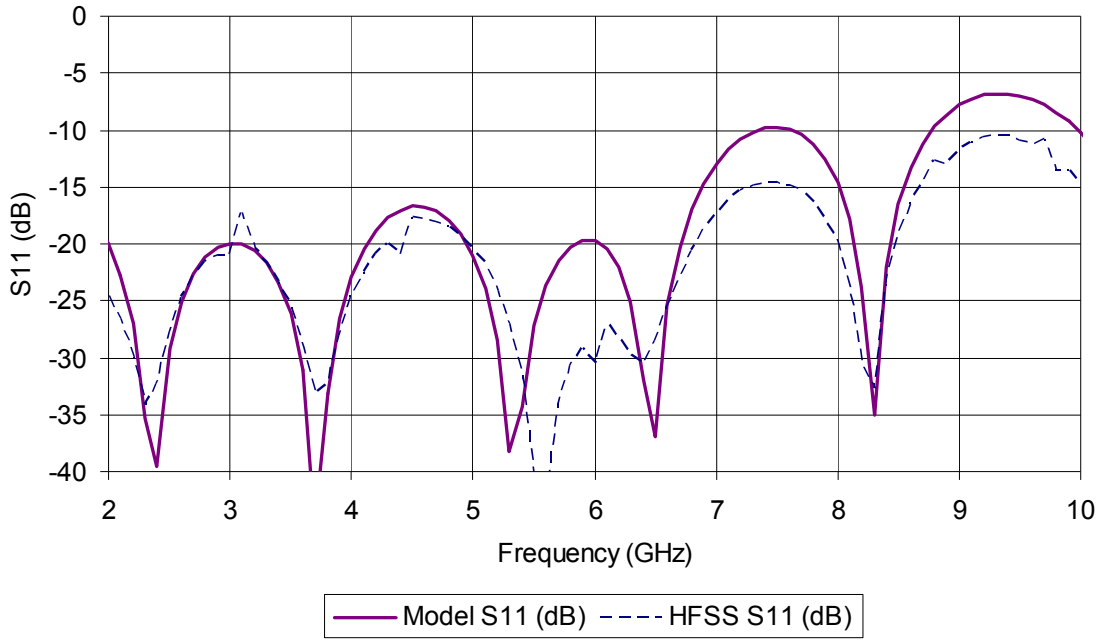

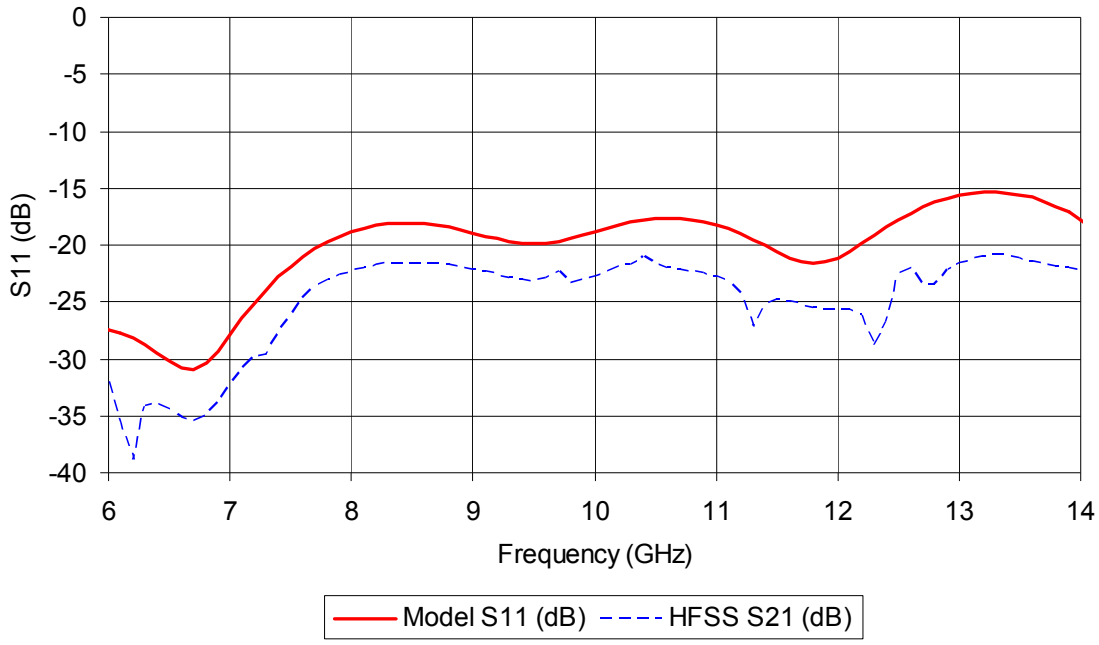

Fig 4.20 Comparison of first order multiple reflection model for arbitrary spacing with HFSS simulation for 6 vanes according to Table 4.1 for Case 1 (top) and Case 2 (bottom). Substrate is 50 mil thick Rogers 6006. H-Guide is 6 mm wide, vanes are 1 mm wide.

The magnitude of the electric field within the structure is shown in Fig. 4.21.

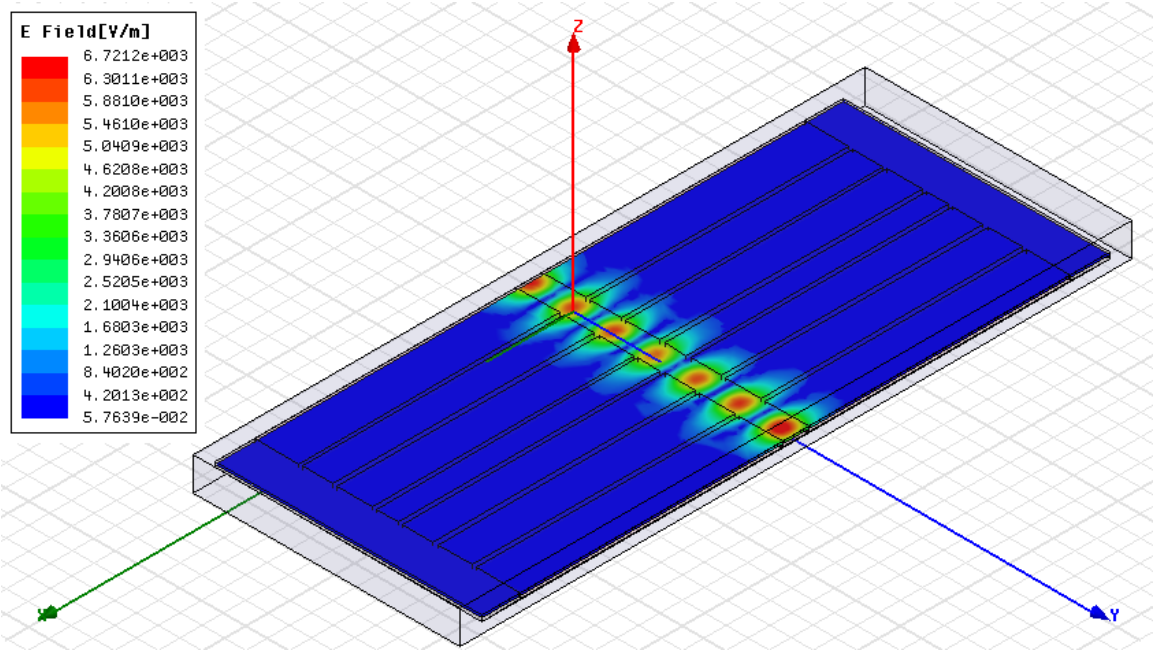

Fig. 4.21 Magnitude of electric field within structure for arbitrary spacing between vanes at 8 GHz for Case 1.

Alternatively, improved results could have also been obtained by simulating the single vane with a commercial software simulator such as HFSS, or using any other numerical techniques.

4.8 Alternate View: *Power-Corrected Reflection Model Alternative View*

For a double interface (3 medium) problem, which is the same problem as the single vane in Fig. 4.4, the reflection seen at the input may be written as [11]

$$\Gamma_{in} = \Gamma_{21} + T_{12}T_{21}\Gamma_{32}e^{-2j\theta}\sum_{n=0}^{\infty}\Gamma_{12}{}^{n}\Gamma_{32}{}^{n}e^{-2jn\theta} \tag{4.22}$$

Let us apply the geometric series,

$$\sum_{n=0}^{\infty} r^n = \frac{1}{1-r} \tag{4.23}$$

Then, Eq. (A1) becomes

$$\begin{aligned}\Gamma_{in} &= \Gamma_{21} + T_{12}T_{21}\Gamma_{32}e^{-2j\theta}\frac{1}{1-\Gamma_{12}\Gamma_{32}e^{-2j\theta}} \\ &= \frac{\Gamma_{21}\left(1-\Gamma_{12}\Gamma_{32}e^{-2j\theta}\right)}{1-\Gamma_{12}\Gamma_{32}e^{-2j\theta}} + \frac{T_{12}T_{21}\Gamma_{32}e^{-2j\theta}}{1-\Gamma_{12}\Gamma_{32}e^{-2j\theta}} \\ &= \frac{\Gamma_{21} - \Gamma_{21}\Gamma_{12}\Gamma_{32}e^{-2j\theta} + T_{12}T_{21}\Gamma_{32}e^{-2j\theta}}{1-\Gamma_{12}\Gamma_{32}e^{-2j\theta}}\end{aligned} \tag{4.24}$$

Now, let us replace T_{12} with $1 + \Gamma_{12} = 1 - \Gamma_{21}$ and T_{21} with $1 + \Gamma_{21}$, and Γ_{12} with $-\Gamma_{21}$

$$\begin{aligned}\Gamma_{in} &= \frac{\Gamma_{21} + \Gamma_{21}{}^{2}\Gamma_{32}e^{-2j\theta} + \left(1-\Gamma_{21}\right)\left(1+\Gamma_{21}\right)\Gamma_{32}e^{-2j\theta}}{1+\Gamma_{21}\Gamma_{32}e^{-2j\theta}} \\ &= \frac{\Gamma_{21} + \Gamma_{21}{}^{2}\Gamma_{32}e^{-2j\theta} + \left(1-\Gamma_{21}{}^{2}\right)\Gamma_{32}e^{-2j\theta}}{1+\Gamma_{21}\Gamma_{32}e^{-2j\theta}} \\ &= \frac{\Gamma_{21} + \Gamma_{32}e^{-2j\theta}}{1+\Gamma_{21}\Gamma_{32}e^{-2j\theta}}\end{aligned} \tag{4.25}$$

Substituting the phase change over medium 2, $\theta = \beta_2 d$, the corresponding equation for reflection becomes [11]

$$\Gamma_{in} = \frac{\Gamma_{21} + \Gamma_{32}e^{-j2\beta_2 d}}{1+\Gamma_{21}\Gamma_{32}e^{-j2\beta_2 d}} \tag{4.26}$$

When Γ is small, this can be approximated as [11]

$$\Gamma_{in} = \Gamma_{21} + \Gamma_{32}e^{-j2\beta_2 d} \tag{4.27}$$

which forms the basis for the non-power corrected multiple reflection model.

Alternatively, the following can also be written,

$$\begin{aligned}\Gamma_{in} &= \Gamma_{21} + T_{12}T_{21}\Gamma_{32}e^{-2j\theta}\frac{1}{1-\Gamma_{12}\Gamma_{32}e^{-2j\theta}} \\ &= \Gamma_{21} + \frac{(1-\Gamma_{21})(1+\Gamma_{21})\Gamma_{32}e^{-2j\theta}}{1-\Gamma_{12}\Gamma_{32}e^{-2j\theta}} \\ &= \Gamma_{21} + \frac{(1-\Gamma_{21}{}^2)\Gamma_{32}e^{-2j\theta}}{1-\Gamma_{12}\Gamma_{32}e^{-2j\theta}}\end{aligned} \tag{4.28}$$

If the denominator is considered small, this can be approximated as

$$= \Gamma_{21} + (1-\Gamma_{21}{}^2)\Gamma_{32}e^{-2j\theta} \tag{4.29}$$

Which is the reflection at the first interface, plus the reflection at the second interface corrected for power lost as the wave crosses the first interface twice, and phase. We can conclude that the power-correction model presented in this chapter is simply a better approximation to the multiple reflection model from [11] than Eq. (4.27).

Using similar cascade techniques as in Eq. (4.18), Eq. (4.29) can be generalized as a sum as shown in Eq. (4.30).

$$\begin{aligned}&\Gamma_{N1} = \sum_{n=1}^{N}\left(1-\left|\Gamma_{n1}\right|^2\right)\Gamma_{(1+n)(n)}e^{-2j(n-1)\theta_n} \\ &\textit{where} \\ &\Gamma_{11} = 0\end{aligned} \tag{4.30}$$

Eq. (4.30) is discussed in more detail in Example 4 of Appendix F, where an exponential taper is compared to an alternate method.

4.9 Summary

In this section, an efficient analysis method based on a power-corrected multiple reflection model for the square periodic H-guide structure has been presented and discussed. Comparison with numerically simulated results, show a very close match.

The successful design and measurement of a square periodic H-guide structure using the microstrip to thin H-guide transition in Rogers 5880 substrate has also been discussed, where the absence of any strong nulls is observed. Finally, an alternate mathematical view of the method has been found and is also included here.

Chapter 5: A Bézier-Curve Shaped Microstrip to H-Guide transition

To physically measure the H-guide and show that the low loss and wide bandwidth as discussed in Chapter 3 is possible, a new transition structure was designed, simulated, then measured. This chapter describes this transition in detail.

5.1 Introduction

An obvious choice of common transmission lines to excite the single TE_{00} mode in the thin H-guide is the microstrip line, because of the small vertical dimension of 1.575 mm ($\approx \lambda / 10$) proposed in the previous section. Transitions such as those proposed in [24] and similar transitions are intended for Non-Radiative Dielectric (NRD) structures [40], cannot excite the intended H-guide TE_{00} mode, require two separate low-loss substrates, and are inherently narrowband because of their resonant behavior. The solution proposed here is a non-resonant, wideband, low-loss Bézier-curve shaped microstrip to H-guide transition using low-loss Rogers 5880 substrate, previously discussed in our paper [48] using low-cost FR4 substrate.

5.2 The Wedge Radial Waveguide

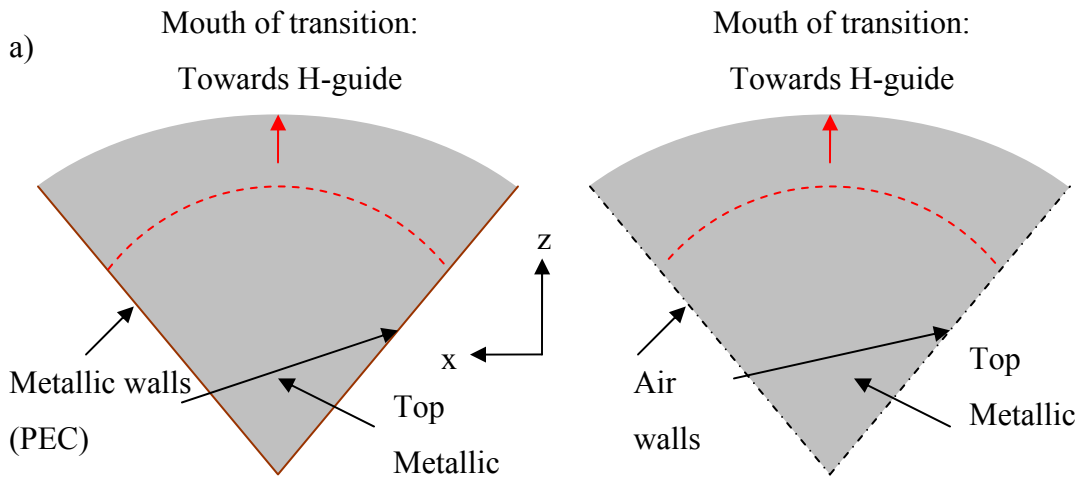

Fig. 5.1 Top view of the Wedge Radial Waveguide. Cylindrical waves are the preferred modes a) side metallic walls, b) air walls.

Consider the air-filled metallic wedge radial waveguide shown in Fig. 5.1(a). On the left and right walls, metallic boundaries, or perfect electric conductors (PEC), enforce the tangential electric fields to be zero. The dominant mode in such a structure is a radial mode [9] [11]. A line of equal phase is shown as a dotted line in the figure for propagation in the +z direction. For the design of a transition to the fundamental H-guide TE_{00} mode, this is not an efficient choice, since both the microstrip line and the H-guide do not have side metallic walls. The transition from the mouth of this transition to and H-guide would therefore be very abrupt.

Now, consider the same waveguide-based transition, with a height of 1.575 mm and filled with air, except with virtual perfect magnetic conductors (PMC) instead of PEC for walls, as shown in Fig. 5.1(b). The virtual PMC boundaries enforce the magnetic fields to be zero, and hence again, radial waves are the preferred modes of operation. The lines of equal phase will be identical for propagation in the +z direction, however, no metallic side edges are needed, thus improving the transition from the microstrip to the H-guide. Only a fraction of the waves that are leaving the mouth of the transition, however, are propagating in the desired +z direction towards the H-guide. Most waves propagate at an angle to that axis, which is energy that will be lost at the transition.

5.2 Profiled Radial Waveguide

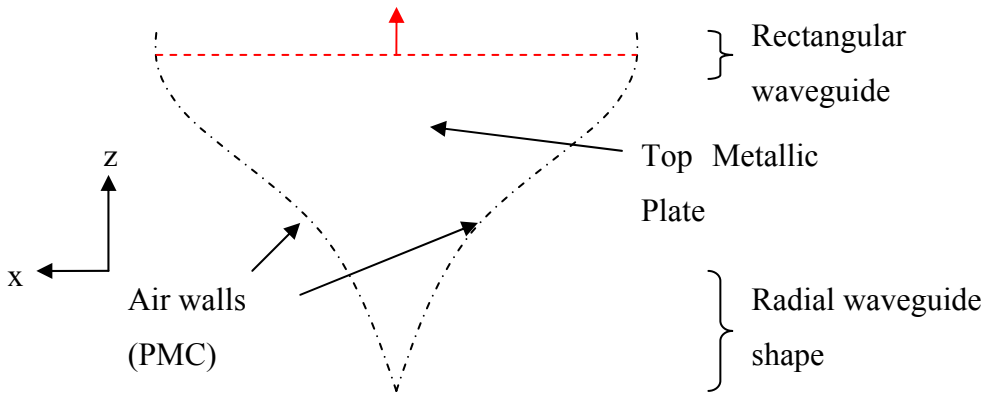

Fig 5.2 A typical profiled horn antenna shape.

A typical profiled transition shape shown in Fig. 5.2 that is discussed in [48] is used as a solution to encourage the propagation of planar, equal phase waves at the mouth of the transition, as opposed to radial waves. Planar waves, as opposed to radial waves, are preferred (less lossy) at the mouth of the transition because the rectangular waveguide shape in this region prefers (modes with least loss) planar waves. The smooth transition from radial waveguide to rectangular waveguide requires a profiled shape, as shown in Fig. 5.2.

5.3 Bézier Curve Profile

To form the required profiled shape, several different formulas have been studied by researchers [49], such as sine squared, exponential, hyperbolic, or polynomial curves. In this design, however, a class of cubic spline curves, called the Bézier curve, is used. The Bézier curve is flexible enough to approximate various different curves while maintaining a smooth shape and allows the specification of the slope, or direction, at both sides of the transition.

The parametric form of the cubic Bézier curve [50] using a 3rd degree Bernstein polynomial over points P0 through P3 is given by

$$\overline{B}(x,z,t) = (1-t)^3\overline{P}_0 + 3t(1-t)^2\overline{P}_1 + 3t^2(1-t)\overline{P}_2 + t^3\overline{P}_3 \tag{4.1}$$

where the parameter, t, varies between 0 and 1

To examine the direction of the curve at its endpoints, consider the derivative of B with respect to t.

$$\frac{d\overline{B}(x,z,t)}{dt} = -3(1-t)^2\overline{P}_0 + \left(-6t(1-t) + 3(1-t)^2\right)\overline{P}_1 + \left(-3t^2 + 6t(1-t)\right)\overline{P}_2 + 3t^2\overline{P}_3$$

$$\left.\frac{d\overline{B}(x,z,t)}{dt}\right|_{@t=0} = -3\overline{P}_0 + 3\overline{P}_1 \tag{4.2}$$

$$\left.\frac{d\overline{B}(x,z,t)}{dt}\right|_{@t=1} = -3\overline{P}_2 + 3\overline{P}_3$$

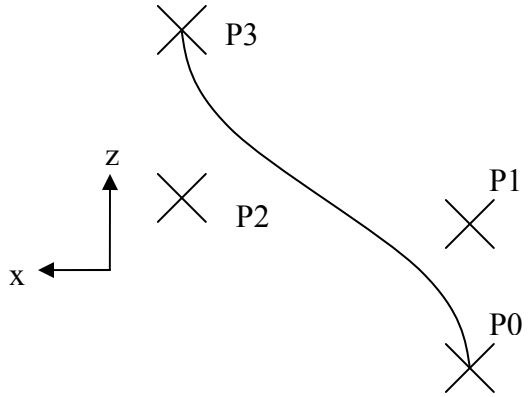

Fig. 5.3 Bézier curve control points.

At the endpoints, where the parameter t is 0 or 1, the direction of the Bézier curve can be found by taking the difference between the two points, P0 and P1, or P2 and P3, respectively. Consequently, as shown in Fig. 5.3, by putting P0 and P1 in line with the +z axis, the beginning of the curve becomes parallel to the +z axis. The same property is applied to points P2 and P3 as shown in the same figure.

5.4 Transition Design

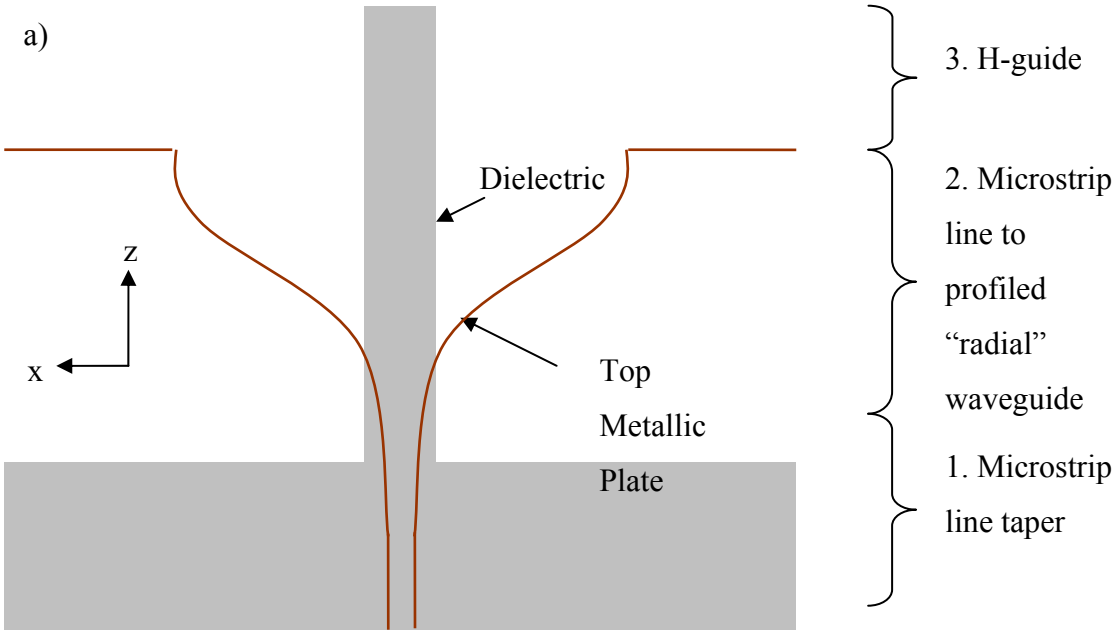

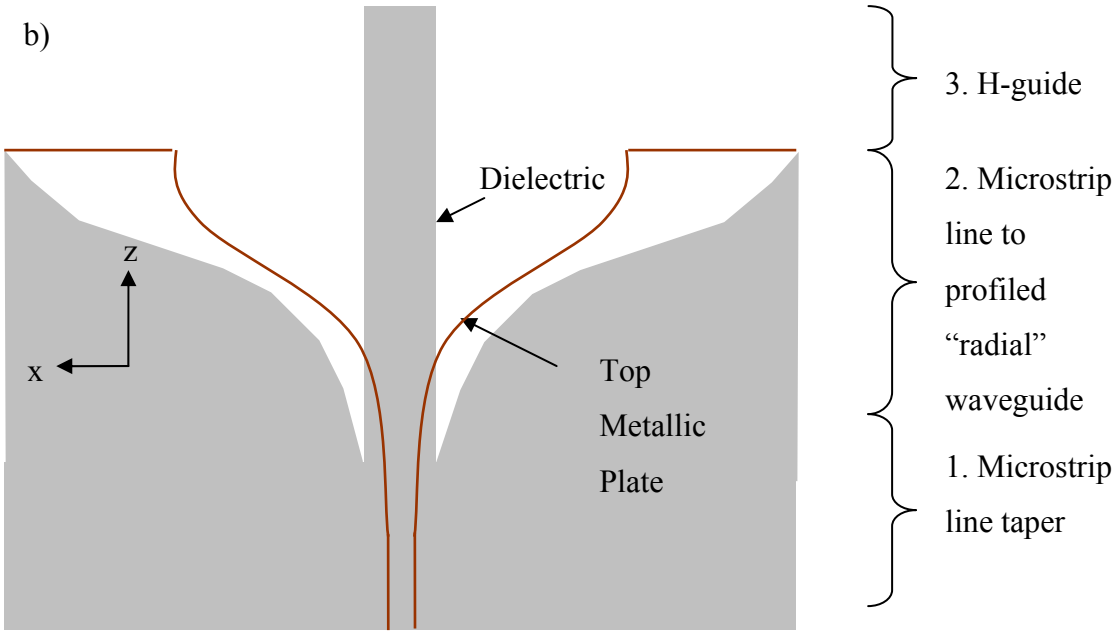

Fig. 5.4 a) Our originally proposed transition [48], b) improved dielectric taper transition.

To form a smooth transition from a microstrip line to an H-guide, it is easiest to consider the transition in several stages as shown in Fig. 5.4. The microstrip line tapers slowly into a wide microstrip line in section 1. To maintain a smooth transition, the slope in this section is enforced to be parallel to the direction of the microstrip line. In section 2, the microstrip line crosses over the dielectric and the profiled "radial" waveguide as described in Fig. 5.2 begins. Section 3 is the H-guide. At the beginning of this section, the slope of the transition is enforced to be parallel to the direction of the H-guide to form the rectangular waveguide section of the transition. In addition, in the improved transition in Fig. 5.4 (b), Sections 1 to 2 are smoothed by slowly tapering the air gap in the dielectric as compared to the abrupt air gap we originally proposed in [48] and shown in Fig. 5.4 (a). This taper in the dielectric improves the return loss for the transition.

The electric field inside the substrate, halfway between the bottom and top sheets, is shown in Fig. 5.5. A photograph of the first transition is shown in Fig. 5.6.

a) 4 GHz

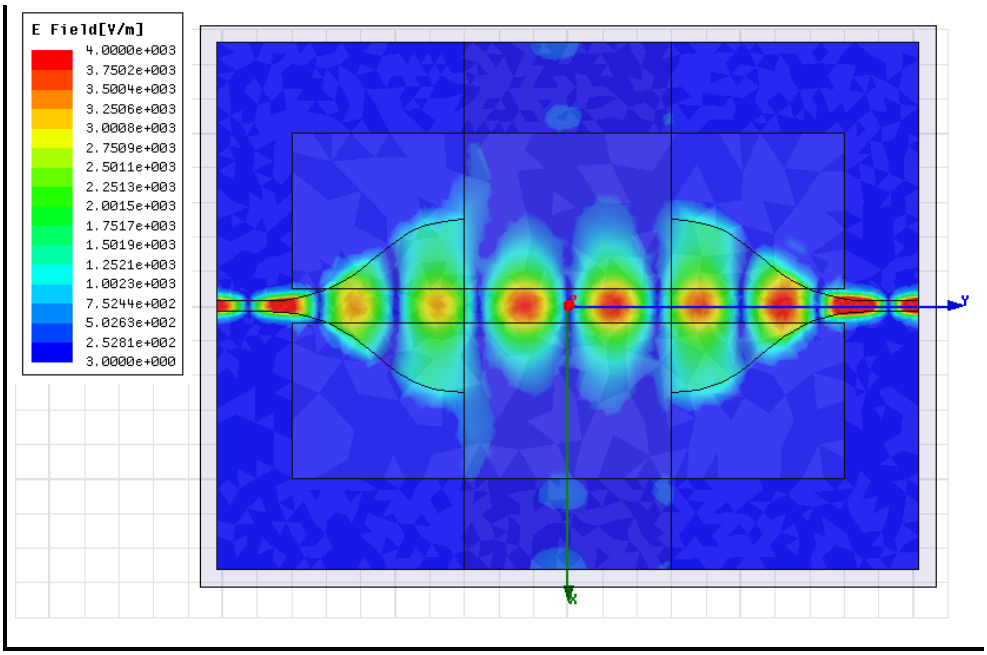
E Field[V/m]
4.0000e+003
3.7502e+003
3.5004e+003
3.2506e+003
3.0008e+003
2.7509e+003
2.5011e+003
2.2513e+003
2.0015e+003
1.7517e+003
1.5019e+003
1.2521e+003
1.0023e+003
7.5244e+002
5.0263e+002
2.5281e+002
3.0000e+000

b) 5 GHz

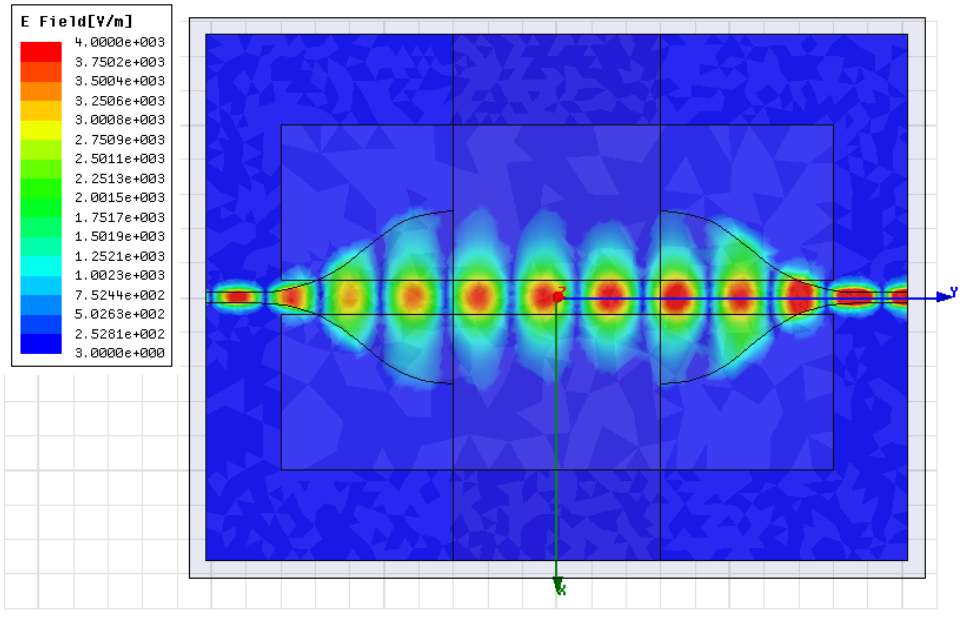
E Field[V/m]
4.0000e+003
3.7502e+003
3.5004e+003
3.2506e+003
3.0008e+003
2.7509e+003
2.5011e+003
2.2513e+003
2.0015e+003
1.7517e+003
1.5019e+003
1.2521e+003
1.0023e+003
7.5244e+002
5.0263e+002
2.5281e+002
3.0000e+000

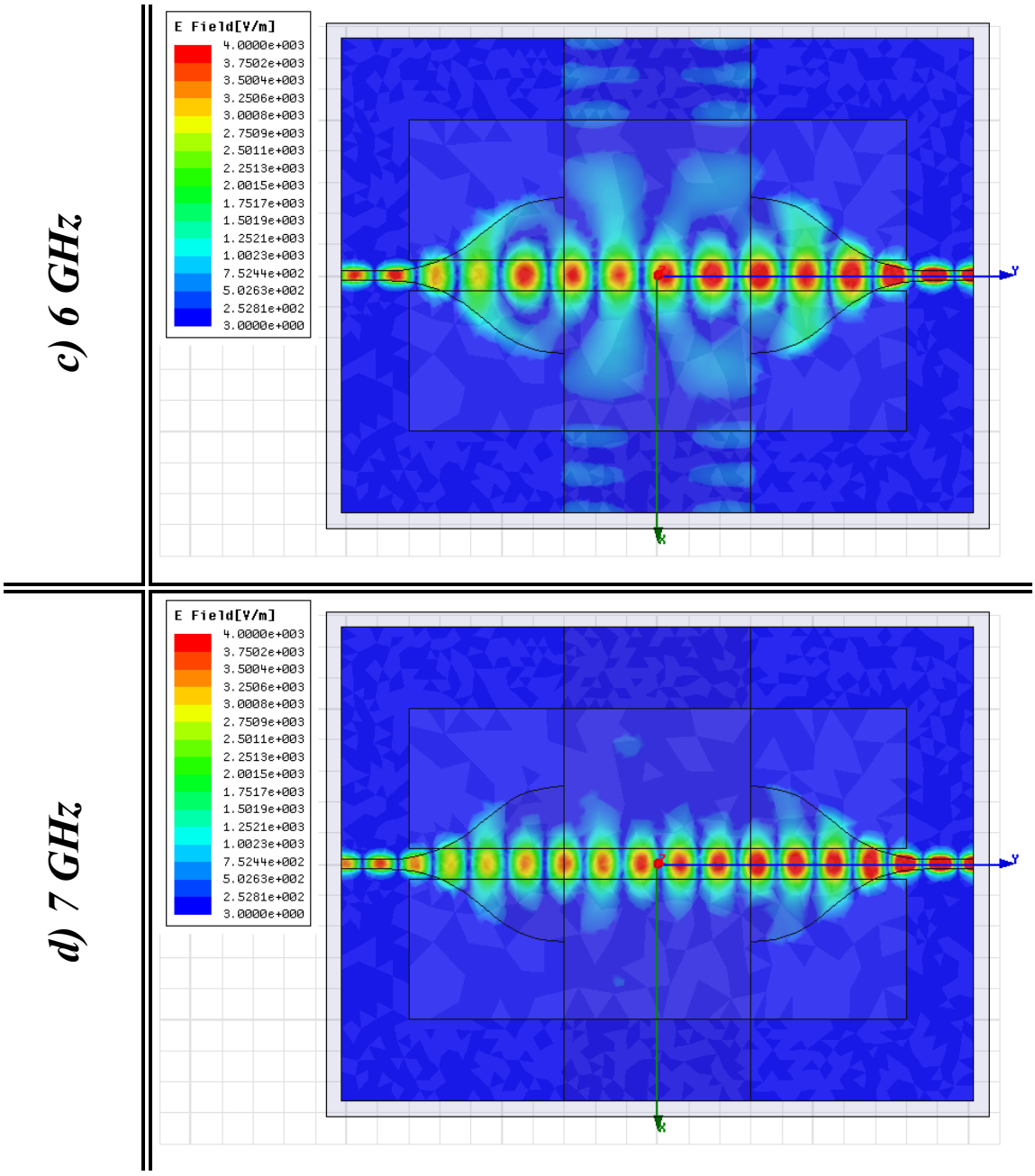

Fig. 5.5 Simulated magnitude of the electric field within the substrate for the FR4 microstrip to H-guide transition using HFSS. Losses in the FR4 substrate are taken into account. In Fig. 5.5 (c) at 6 GHz, some leakage from the H-guide is apparent, however, most of the energy is directed towards the output port.

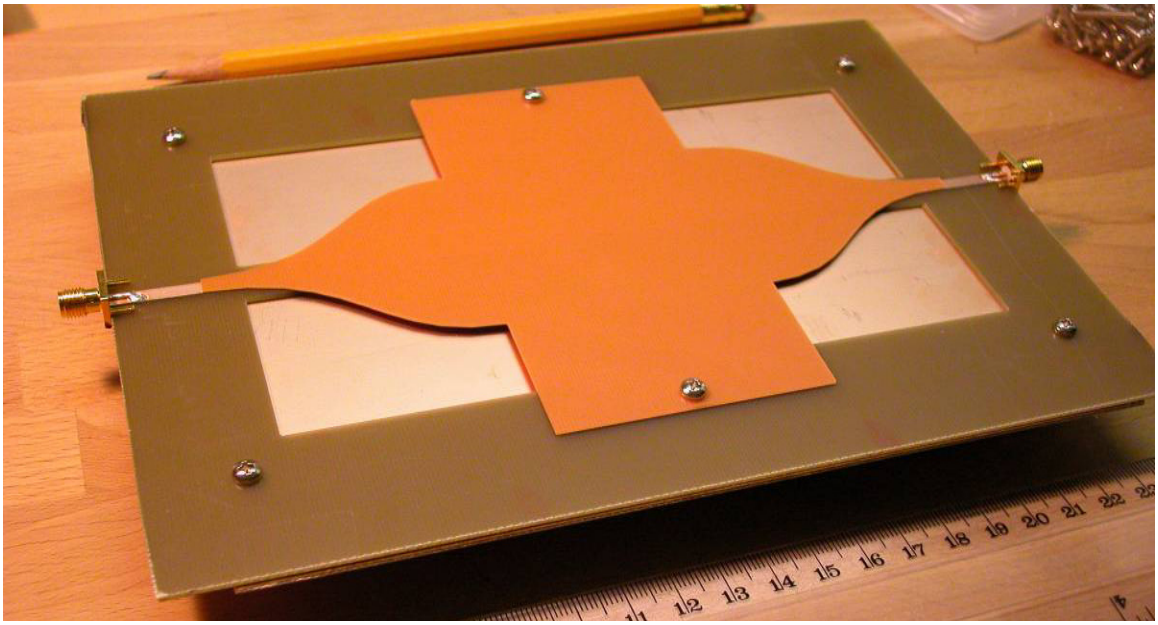

Fig. 5.6 Photograph of the first microstrip to H-guide transition using FR4 substrate.

Measured results for the prototype in Fig. 5.6 are compared to simulation in Fig. 5.7. A reasonably close match is observed, however, losses become greater as the frequency increases.

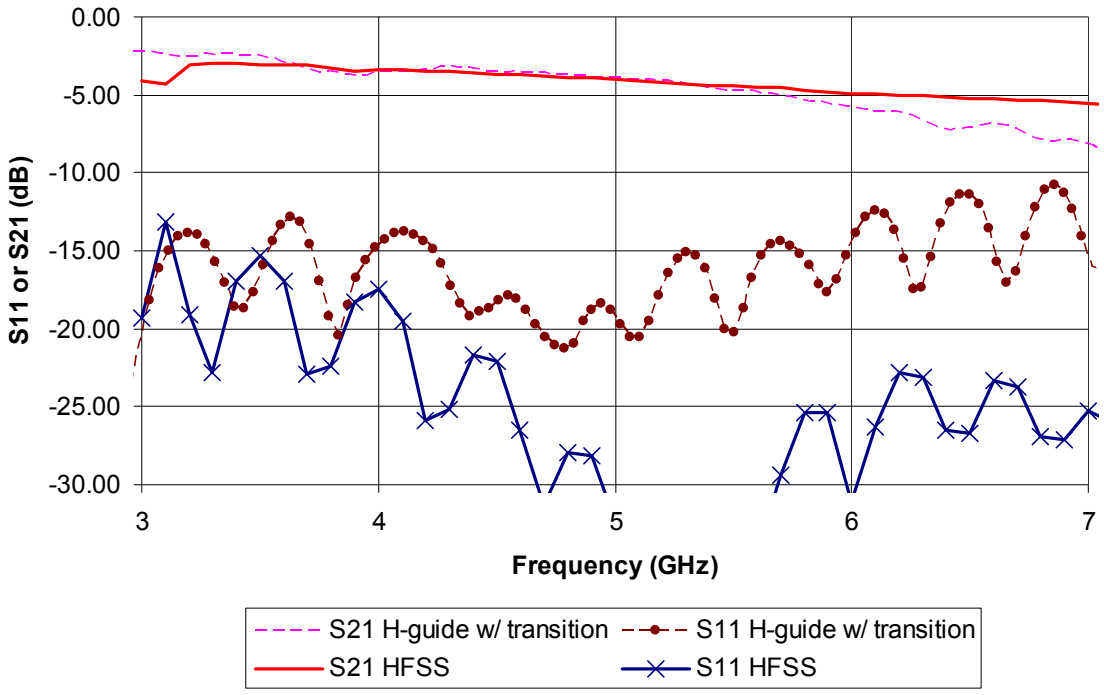

Fig 5.7 Comparison of measured insertion (-S21) and return loss (-S11) compared to simulated insertion and return loss using HFSS.

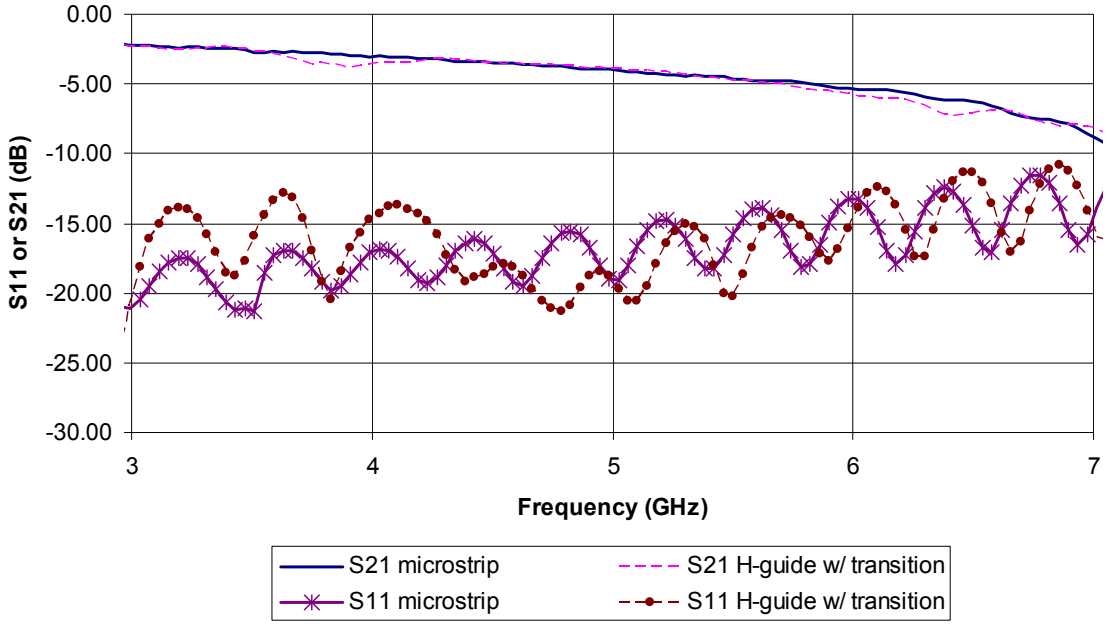

Fig. 5.7 Comparison of raw data for measured microstrip line compared to raw measured data for a back-to-back microstrip line to H-guide to microstrip line transition.

In Fig. 5.7, the raw measured data for the microstrip to H-guide transition is compared to raw measured data for a microstrip line of the same length and same connectors. The transmission and return losses are very similar, meaning almost no energy is lost within the microstrip to H-guide transition. Most of the differences seen in Fig. 5.6 from 5 to 7 GHz are due to losses in the coaxial to microstrip line connectors.

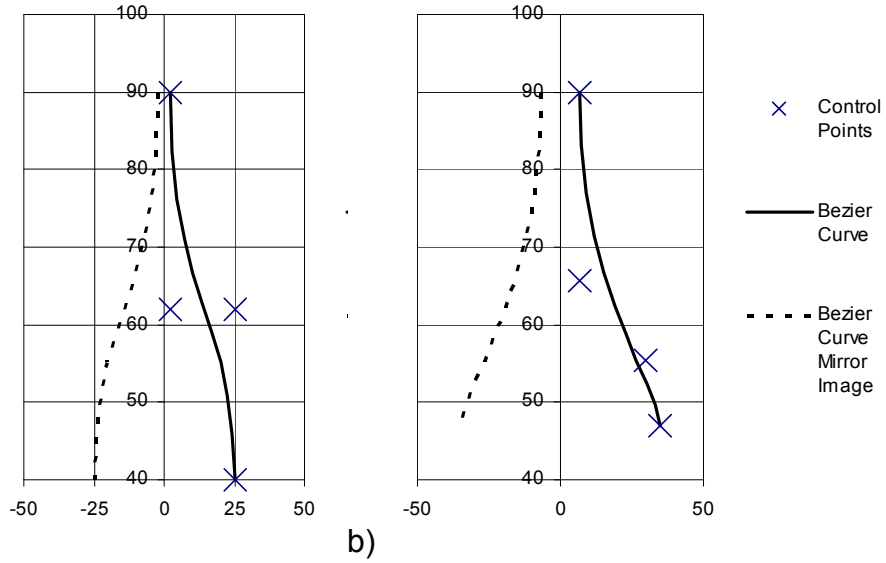

Fig. 5.8. Dimensions for the inner and outer curve. a) Bézier curve control points P0 (2.425, 90.0), P1 (2.425, 62.0), P2 (25.0, 62.0), and P3 (25.0, 40.0) are shown, where

units are in mm. b) Dimension of the Bezier transition board cutouts. Bézier curve control points P0 (6.6, 90.0), P1 (6.6, 65.25), P2 (30.0, 55.3125), and P3 (35.0, 47.0) are shown, where units are in mm.

Dimensions for the inner and outer curves for the improved transition shown in Fig. 5.4 (b) are shown in the caption in Fig. 5.8. A three-dimensional exploded diagram of one of the first the fabricated back-to-back transition prototypes using low-loss Rogers 5880 substrate is shown in Fig. 5.9.

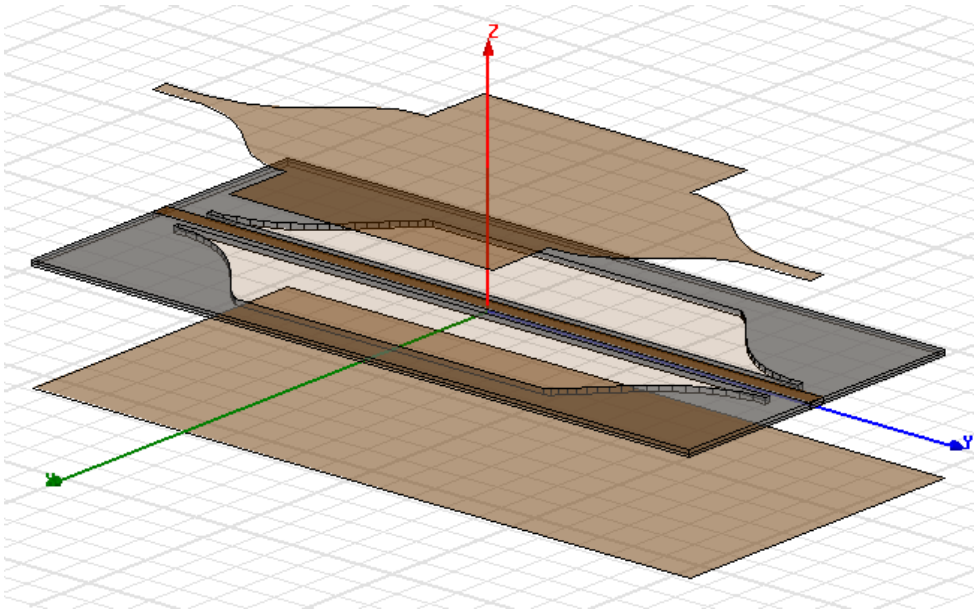

Fig. 5.9 Three dimensional exploded view of transition prototype using low loss Rogers 5880 substrate.

A photograph of the assembled prototype and measurements of insertion and return loss are shown in Fig. 5.10 below.

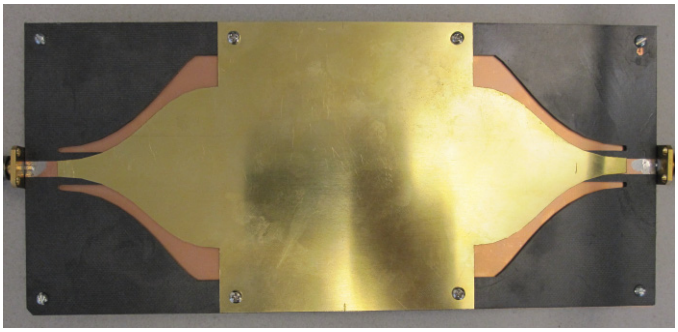

Fig. 5.10 Assembled prototype using low-loss Rogers 5880 substrate.

The raw measured insertion and return loss of the prototype shown in Fig 5.10 is compared to simulated results in Fig. 5.11. Some additional losses are due to fabrication errors and the back-to-back coaxial to microstrip line connectors used.

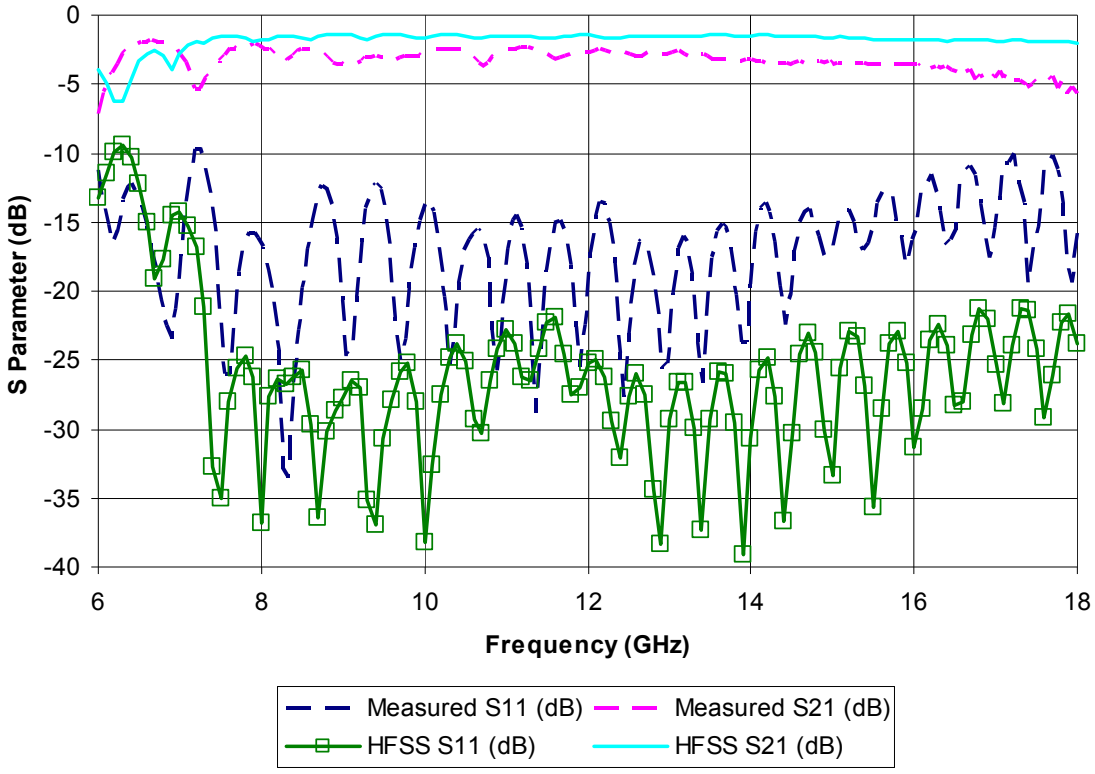

Fig. 5.11 Measured insertion and return loss is compared to simulated results for the transition using Rogers 5880 substrate as shown in Fig. 5.4 (b).

The electric field within the structure was simulated and plotted in Fig. 5.12. From these plots, some leakage is apparent, which has caused non-idealities for the antenna design in the next chapter. The design was a compromise between size and performance since a larger size has a smoother transition, and thus less leakage and wider bandwidth.

a) 10 GHz

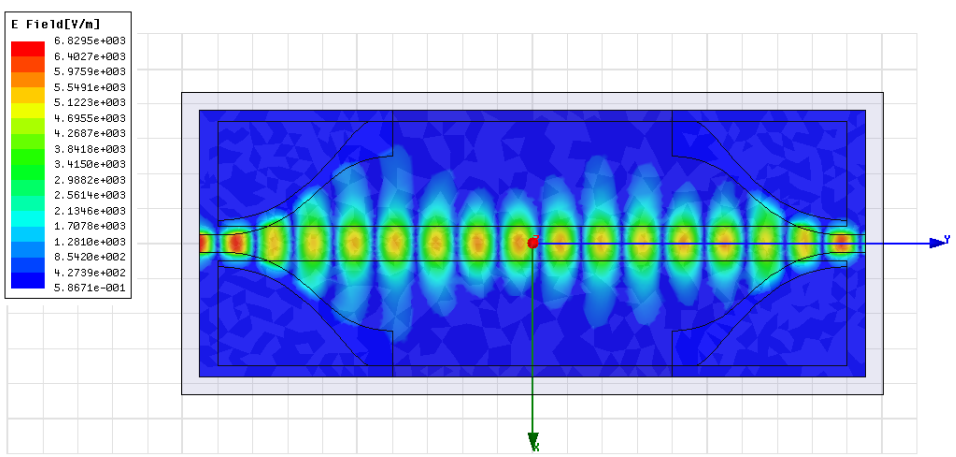

b) 12 GHz

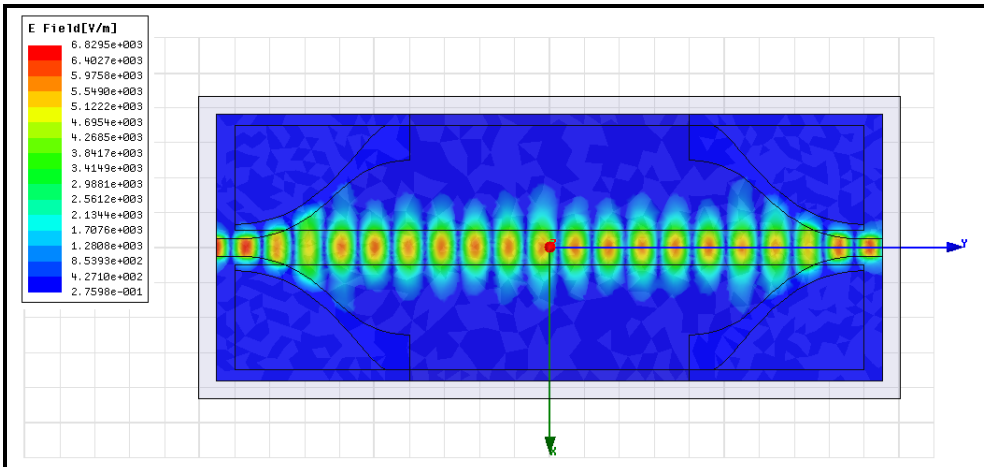

c) 14 GHz

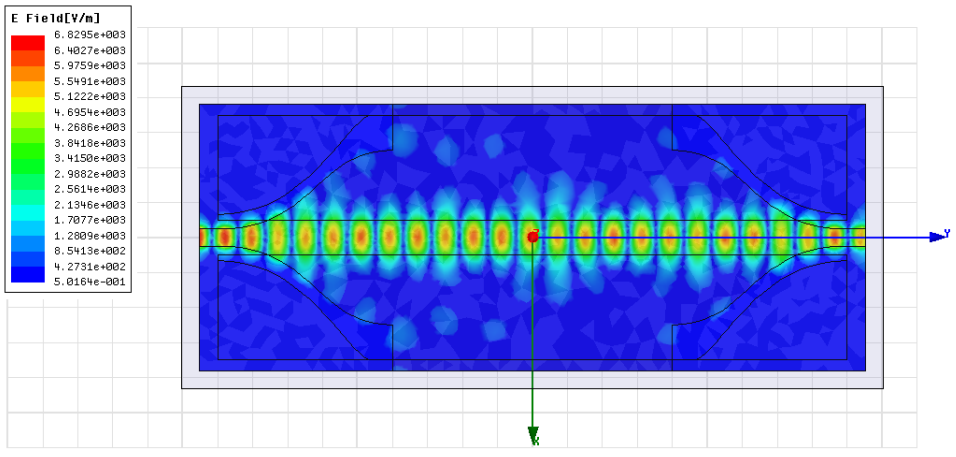

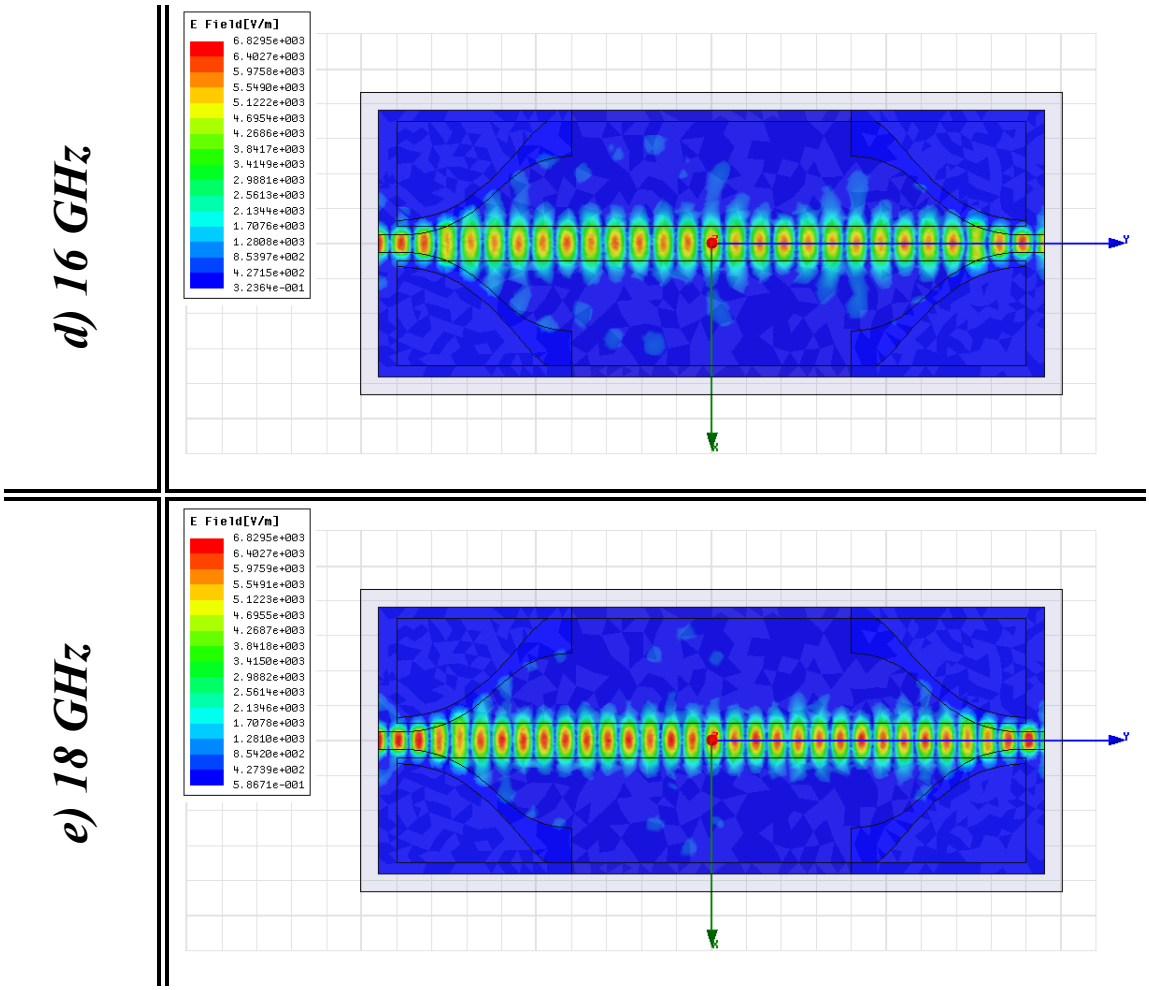

Fig. 5.12 Magnitude of electric field within microstrip to H-guide transition in Rogers 5880. Some leakage is apparent.

5.5 Summary

In this chapter, the design of the Bézier curve shaped microstrip to H-guide transition has been discussed. Two prototypes have been discussed; the first using low-cost, lossy FR4 substrate, and the second using low-loss Rogers 5880 substrate. Measured data has shown that the device is wideband and relatively low loss.

Chapter 6: Analysis and Design of H-guide Aperture Antennas

In this chapter the dielectric waveguide aperture horn antenna is discussed. Simulated results from a recent conference paper are discussed, as well as a new antenna design.

The H-guide, originally proposed by Tischer [2], has been applied to antenna designs in various forms. The H-guide structure is shown in Fig. 6.1. Note that if the drawing is turned on its side, it forms the letter "H".

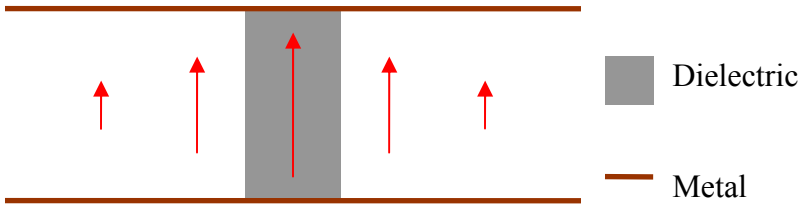

Fig 6.1. The H-guide. The magnitude and direction of the electric field is represented by arrows.

Several antennas have been fabricated using the H-guide approach, such as slot based antennas [51] [52] [53], or leaky wave antennas [41][54]. In this section we present a new endfire-based design without any slots. In the following sections, the design and obtained results are presented and discussed.

6.1 Gapped H-Guide

In this section, we discuss a "gapped" H-guide, where an air gap is added to the top of the dielectric portion of the H-guide. The structure is shown in Fig. 6.2.

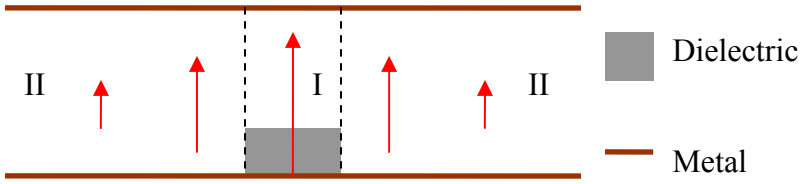

Fig. 6.2. Gapped H-Guide. The magnitude and direction of the electric field is represented by arrows.

There is sufficient difference in the effective dielectric constant in region I compared to region II. This difference allows the structure to support guided propagation in a similar fashion as the groove guide [55] [56] [57] or other related guided structures. Therefore, if an air gap is added between the dielectric and top metallic plate, the effective dielectric constant of the dielectric is simply reduced, so that guided propagation is still possible.

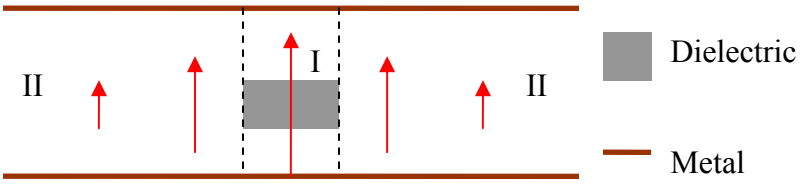

Fig. 6.3. Double Gapped H-Guide. The magnitude and direction of the electric field is represented by arrows.

Similarly, if dual air gaps are added, as shown in Fig. 6.3, guided propagation is also possible. This has the advantage of being completely symmetric, as well as being a better match to free space at the mouth of the horn.

6.2 H-Guide Aperture Antenna design

Previous dielectric horn antenna designs, such as the ones that is discussed in [49][58], use a different approach than will be discussed here. In [58], for example, dielectric lies on the metallic walls of the tapered metallic structure; while in this design, the dielectric lies in the center. In [49], the horn is fed by a dielectric-filled rectangular waveguide, while this horn is fed by an H-guide. An H-guide aperture horn antenna, which operates with electric fields parallel to periodic metallic bars, but without a center dielectric in the tapered section, can be found in [60].

The structure shown in Fig. 6.2 has been applied to an H-guide aperture horn antenna design as shown in Fig. 6.4, which we presented previously in [61]. Here, the fields are guided by the dielectric in the horizontal plane, as an H-guide, then tapering slowing into a gapped H-guide. In the vertical plane, fields are guided by the metallic plates. The

antenna radiates primarily at the mouth of the horn, or at the end of the gapped H-guide as shown in Fig. 6.4, not along its edges.

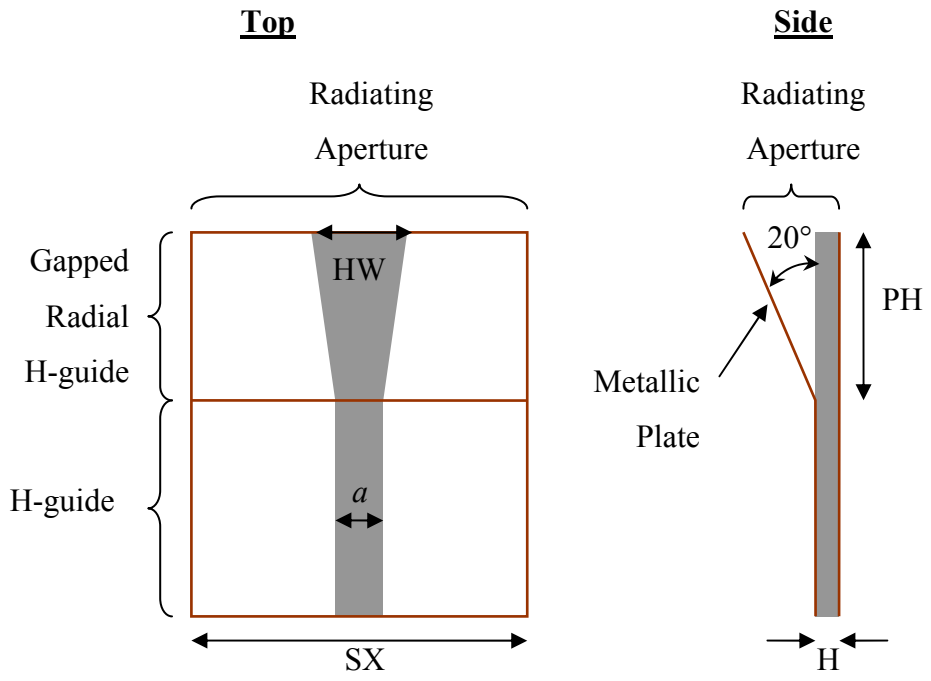

Fig. 6.4. H-guide aperture horn antenna. Substrate is Rogers 5880. *a* = 10 mm, H = 1.575 mm, PH = 100 mm, HW = 22 mm, SX = 100 mm. The radiating aperture is at the front of the horn only. In the horizontal plane, fields are guided by the dielectric. In the vertical plane, fields are guided by the metallic plates.

Fig 6.5 shows the magnitude of the electric field within the structure at 9 and 15 GHz when excited using a waveport. Here, the magnitude distributions shows that fields travel from the input port to the mouth of the horn.

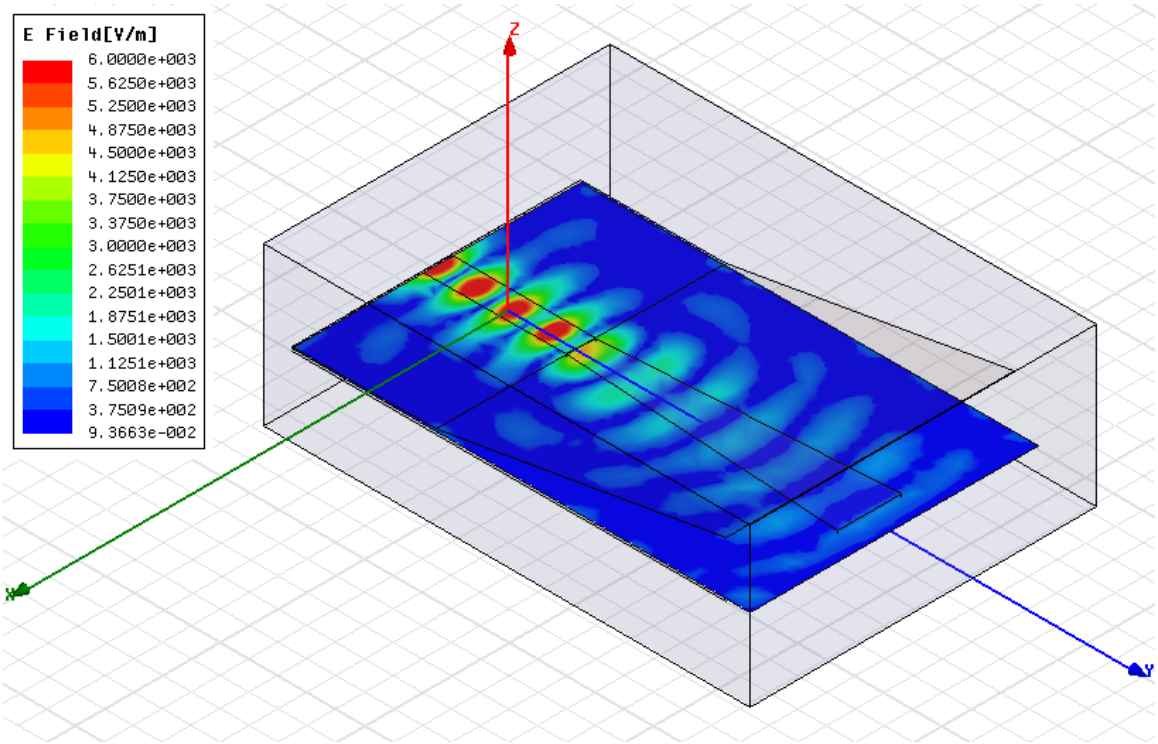

Fig. 6.5(a) Magnitude of the Electric Field within the dielectric/air portion of the H guide and partial H-guide at 9 GHz.

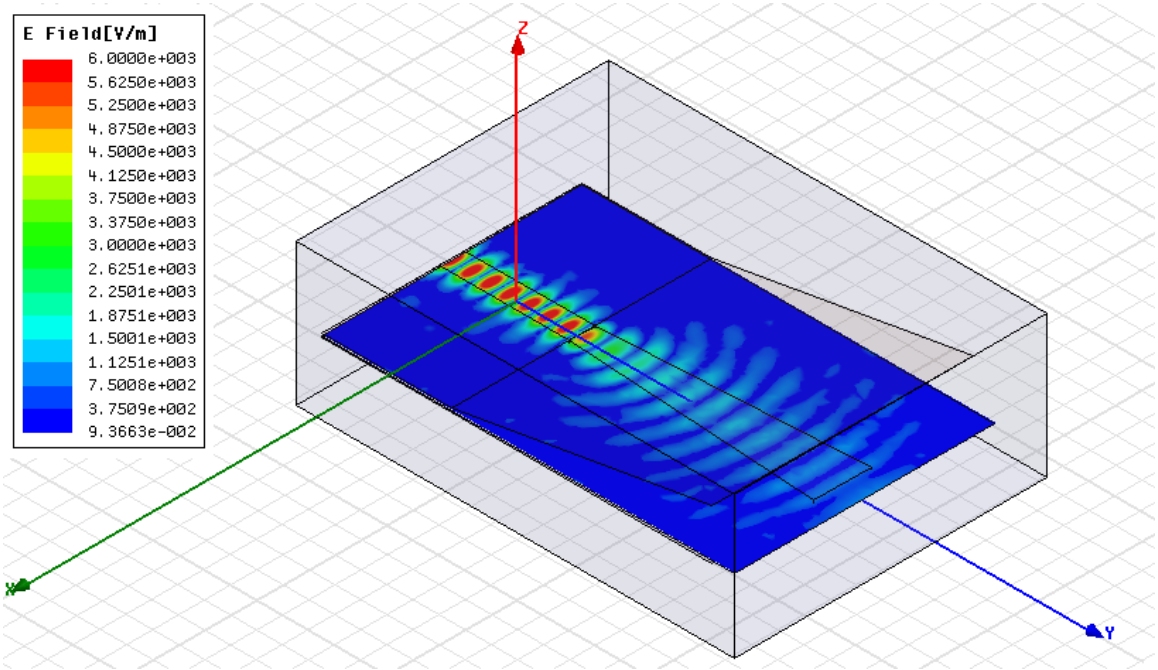

Fig. 6.5(b) Magnitude of the Electric Field within the dielectric/air portion of the H guide and partial H-guide at 15 GHz.

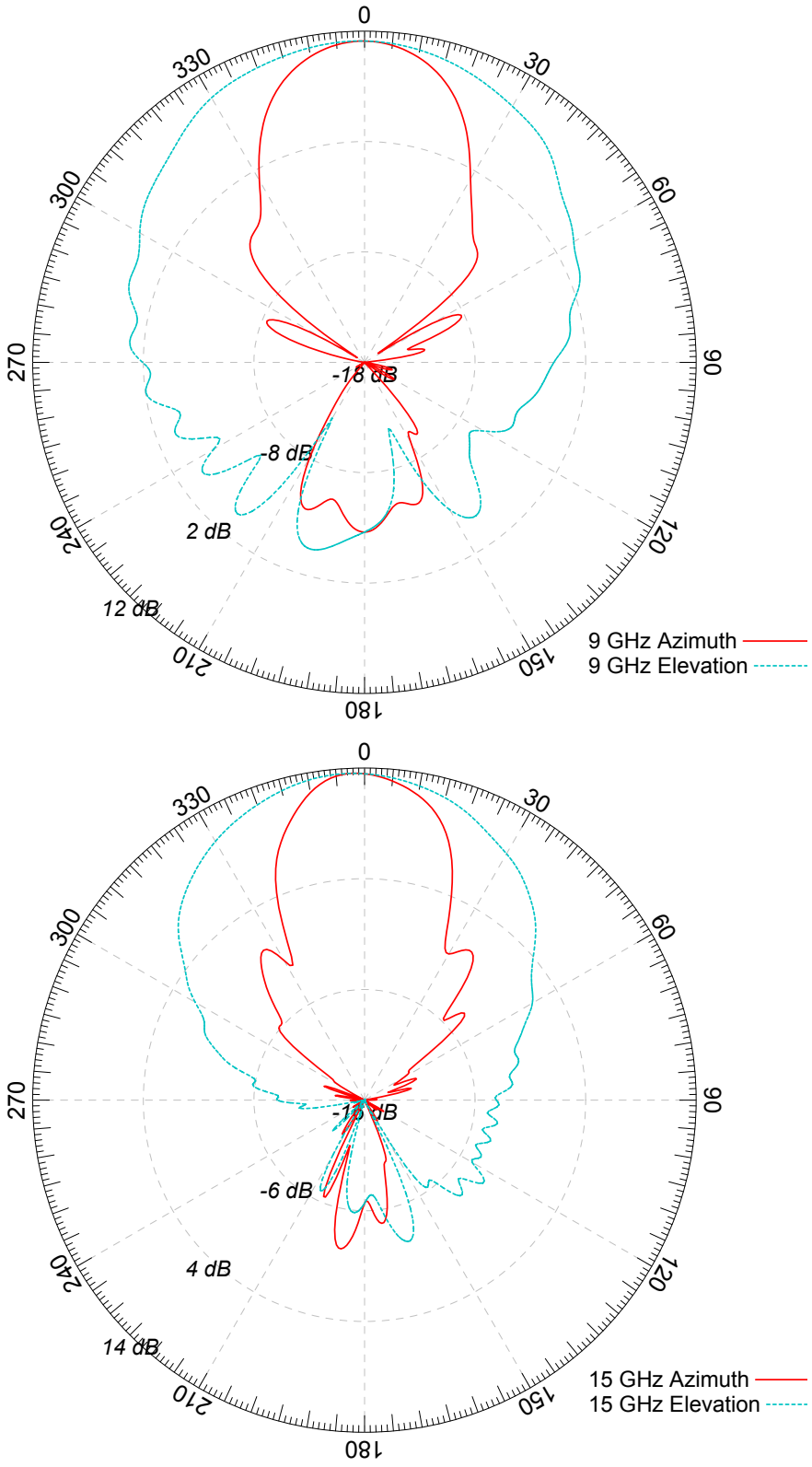

Fig. 6.6 Radiation pattern (total gain in dB) in the yz plane (H-plane, dot) and xy plane (E-plane, cross) at 9 GHz (top) and 15 GHz (bottom) for the antenna show in Fig. 6.4.

In Fig. 6.6, the radiation pattern at 9 GHz is shown, where the return loss for the structure is shown in Fig. 6.7. Using the Bézier shaped microstrip to thin H-guide transition discussed in the previous sections, the antenna design becomes relatively straightforward.

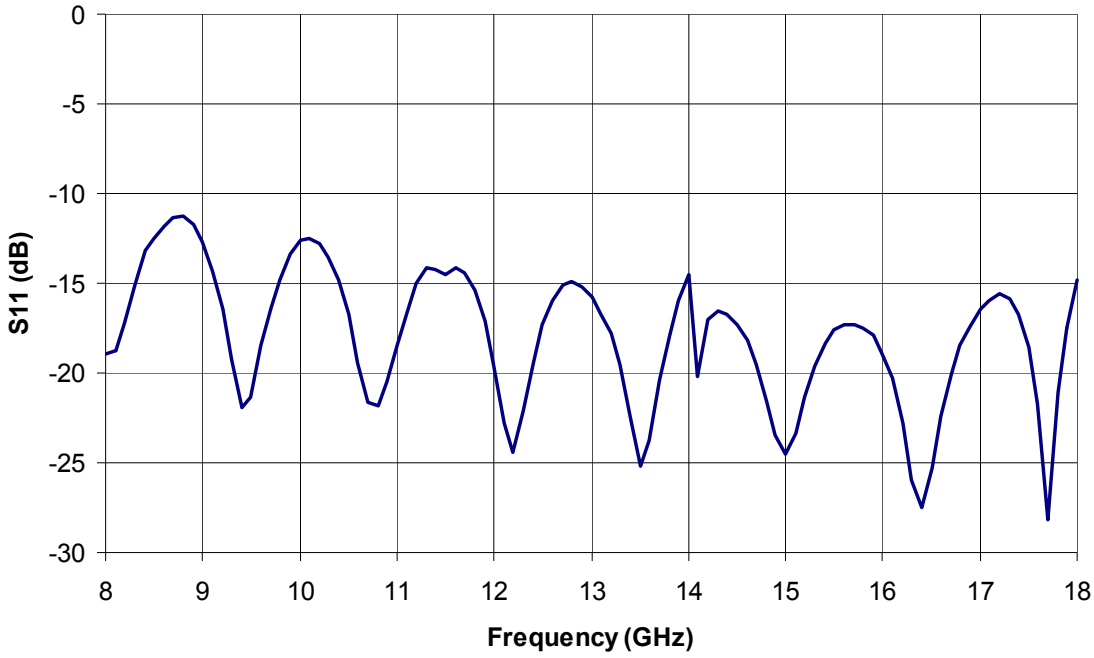

Fig. 6.7 Return loss at the H-guide waveport input for the antenna shown in Fig. 6.4.

An improved design which applies the double air gaps is shown in Fig. 6.8. As the wave approaches the mouth of the horn, the fields are guided primarily by the dielectric in both the horizontal and vertical directions, especially for wider vertical apertures in terms of wavelength. A wave that is guided in both the horizontal and vertical directions by a rectangular dielectric block is a rectangular dielectric waveguide, which is discussed in more detail in Appendix C.

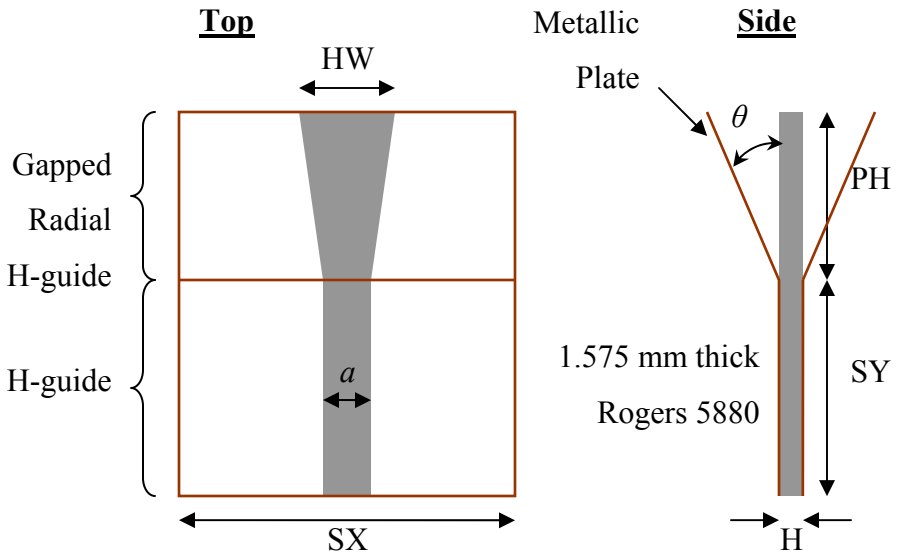

Fig. 6.8 Dual Air gaps. *a* = 10 mm, H = 1.575 mm, SX = 100 mm, PH = 100 mm, HW = 26 mm, θ = 18°.

6.3 Separating Input Impedance and Aperture

Before discussing H-guide aperture antennas of increased complexity, it is beneficial to discuss some theory behind their design. In the previous section, a taper from the H-guide to the gapped H-guide is used to transition into free space. Typically, we must consider the input impedance of an antenna to ensure good radiating efficiency. A poor return loss (poor impedance match) indicates that power is reflected back towards the input port instead of being transmitted. In many antenna designs, however, structures that change the input impedance also change the fields at the aperture, thus affecting the radiation pattern. The H-guide aperture antenna may be one exception to this design restriction as will be discussed in this section.

Let us examine the theoretical return loss using the power-corrected multiple reflection method discussed in Chapter 4. The return loss of an exponential taper has been compared between the multiple reflection method and an exponential closed form model [1] in Appendix F, Example 4. In that example, a smooth exponential taper has been split into 10 discrete sections, where the input impedances are a close match. Now, consider the segmentation of a gapped H-guide taper as shown in Fig. 6.9.

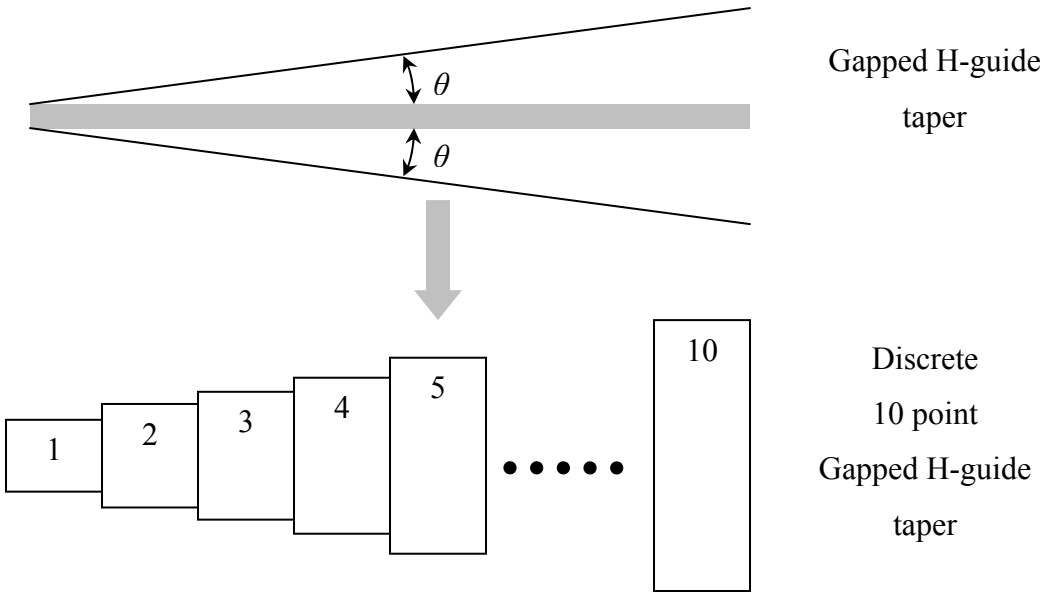

Fig. 6.9 Segmentation of an H-guide taper. Each section has an effective propagation constant, β_n, and length l_n.

If section 1 approaches a propagation constant that is equal to an H-guide (β_z), then $\beta_1 \rightarrow \beta_z$. Each subsequent section then has an effective propagation constant, β_n, and length l_n. The reflection coefficient, with reference to the start of the taper, is then given as (see Eq. (4.18) in Chapter 4).

$$\Gamma_{N1} = \sum_{n=1}^{N} \left(1 - \left|\Gamma_{n1}\right|^2\right) \Gamma_{(1+n)(n)} e^{-2j(n-1)(\beta_n l_n)}$$

where

$$\Gamma_{11} = 0 \tag{6.1}$$

Note that the square in the bracketed term is removed since each segment represents only one crossing of an interface, as opposed to two as in Chapter 4.

The task of finding a theoretical propagation constant for the gapped H-guide has not been considered here, since no closed form solution exists and some approximations must be made. Previous attempts from literature at approximating the propagation constant for a simpler rectangular dielectric waveguide are discussed in Appendix C. By examining eq. (6.1) and making physical observations, however, we can obtain some useful results.

At the beginning of the taper, the propagation constant, β_1 approaches β_z, the propagation constant of the H-guide. Therefore, the slower the taper, the lower the reflection

coefficient at the beginning of the taper, and a lower total reflection coefficient according to (6.1) will be obtained.

At the mouth of the horn, or at the end of the taper, the metallic plates are so far apart that the propagation constant of the gapped H-guide approaches that of a rectangular dielectric waveguide. In addition, because the rectangular dielectric waveguide in this design is so thin, the propagation of the dielectric waveguide is close to that of free space, β_o. Changes in the shape of the dielectric here do not significantly change the propagation constant as long as the propagation constant is close to that of free space. This allows the modification of the structure at the mouth of horn to "shape" the propagating wave, *without significantly changing the reflection coefficient!*

Since it possible, using this approach, to shape the fields at the mouth of the horn without significantly affecting return loss, it is possible to also shape the fields in the far field, and thus the radiation pattern. Consider the aperture of the horn to be an aperture source, then the space factor can be given as [62]

$$SF = \int_{-l_y/2}^{l_y/2} \int_{-l_x/2}^{l_x/2} A_n(x', y')\, e^{j[kx'\sin\theta\cos\phi + ky'\sin\theta\sin\phi + \phi_n(x', y')]} dx'\, dy' \tag{6.2}$$

Where l_x and l_y are the x and y dimensions of the aperture, and A_n and φ are the amplitude and phase distributions over the aperture. The element pattern can be assumed to be a small rectangular aperture.

Eq. (6.2) can be interpreted as a two dimensional Fourier transform [62]. A constant phase aperture, with a smooth Gaussian shaped pattern in the x-direction, and a cosine squared distribution in the y-direction, will therefore form a radiation pattern with low sidelobes.

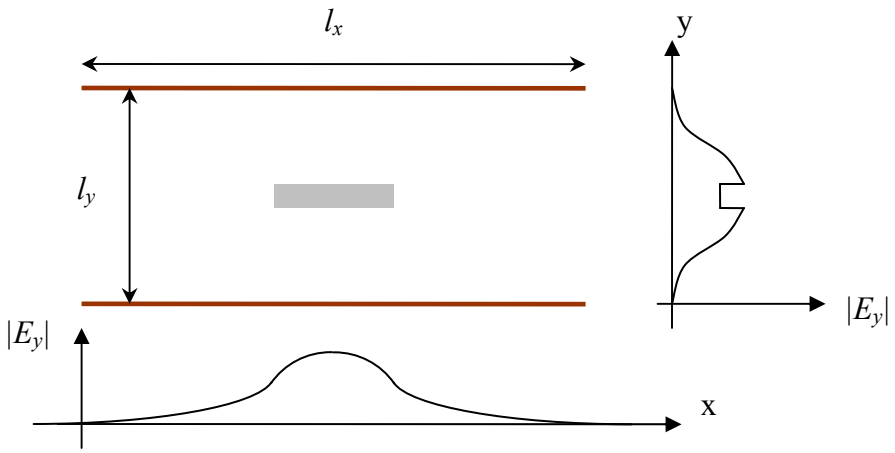

Fig. 6.10 Aperture and ideal amplitude distribution of Gapped H-guide aperture antenna. The notch in the vertical direction occurs because of boundary conditions over the dielectric and is unavoidable. Its effects are minimized through the use of thin substrates. (Drawing not to scale.)

In the next section, this method has been applied to correct the phase at 18 GHz and thus achieve low sidelobes at this frequency. Examination of the phase at the aperture confirms this. It should be easy to see that this design goal is possible over a wide bandwidth if the aperture is made large enough.

The structure in Fig. 6.10 can be simulated in HFSS and the magnitude of the electric field can be plotted for a 10 mm wide, 1 mm tall dielectric segment as shown in Fig. 6.11 and Fig. 6.12. The air-dielectric boundary is shown with dotted lines.

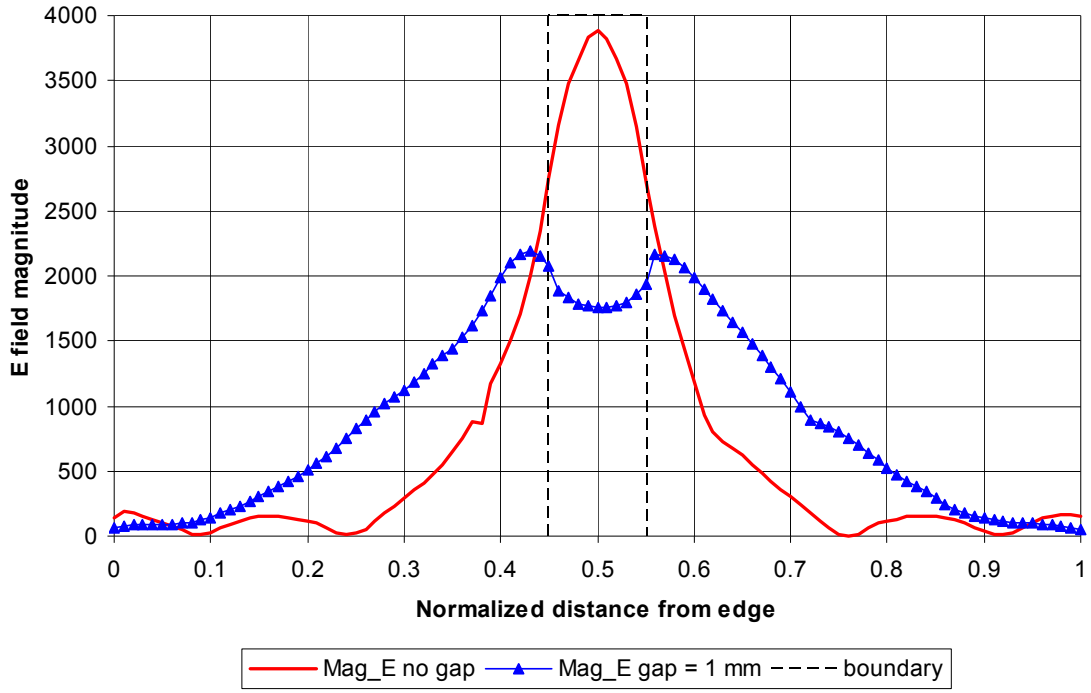

Fig. 6.11 Comparison of the magnitude of the electric field in the x-direction within an H-guide (no gap) and a gapped H-guide with a 1 mm gap between the dielectric and metallic plate.

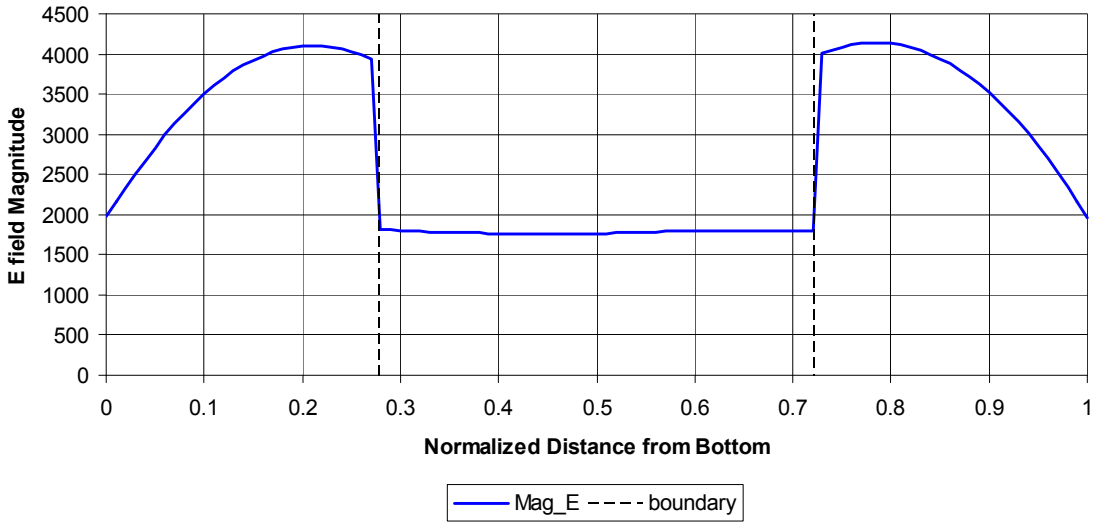

Fig. 6.12 Magnitude of the electric field in the y-direction within a gapped H-guide with a 1 mm spacing between the dielectric and metallic plates.

Because the fields within the gapped H-guide are complex, a parametric study is included in Fig. 6.13, where the vertical horn angle is varied, while the inner dielectric taper in the horizontal direction remains constant.

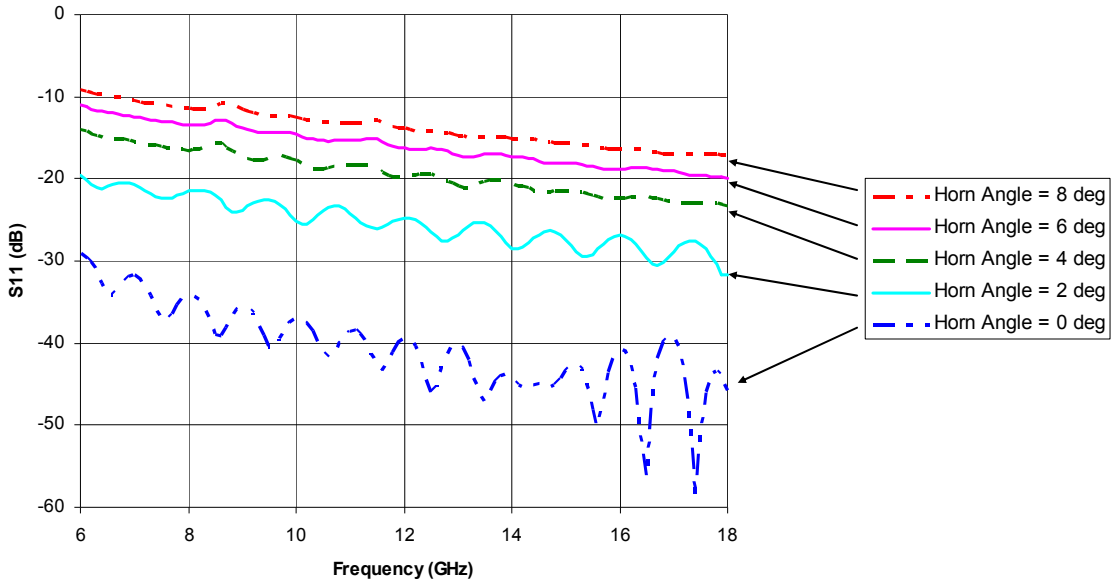

Fig. 6.13 Variation in angle of metallic plates. Inner dielectric tapers from 10 mm to 30 mm for each run. The horn angle is measured from the horizontal plane to the plane of one of the metallic plates.

In this parametric study, the radiation boundary is placed at the aperture of the horn, so that the effects of the aperture on the reflection coefficient are removed. The variations in Fig. 6.13 are therefore due only to the change in metallic plate angles.

From Fig. 6.13, we can conclude that for an optimal angle for operation from 6 to 18 GHz, where a return loss of 10 dB or better is required, is equal to 8 degrees in the vertical plane, close to the H-guide to gapped H-guide transition. This corresponds to a dielectric taper from 10 mm to 30 mm, given that Rogers 5880 is used as a substrate, and the H-guide plate separation distance is equal to 1.575 mm.

6.4 Dual Angle and Phase Corrected H-Guide Aperture Design

A second improved design is shown in Fig. 6.14, where a dual taper angle for the metallic plates is used, as well as a curved dielectric shape. The curved dielectric shape allows the phase at the mouth of the horn to be almost equal at 18 GHz, thus achieving low sidelobes at this frequency as discussed in the previous section.

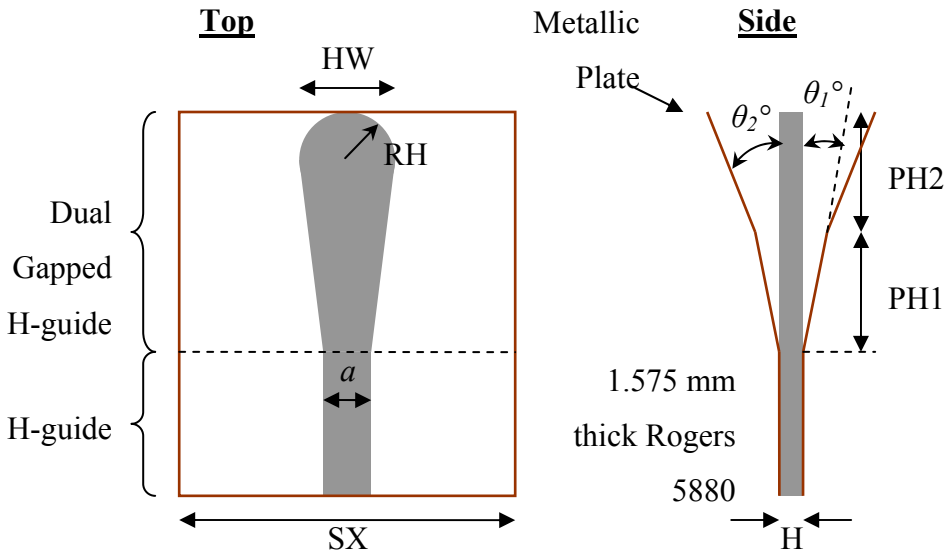

Fig. 6.14 Improved dual air gap H-guide aperture horn antenna design. a = 10 mm, H = 1.575 mm, SX = 100 mm, PH1 = 50 mm, PH2 = 50 mm, HW = 32 mm, RH = HW / 2 = 16 mm, θ_1 = 15°, θ_2 = 18°.

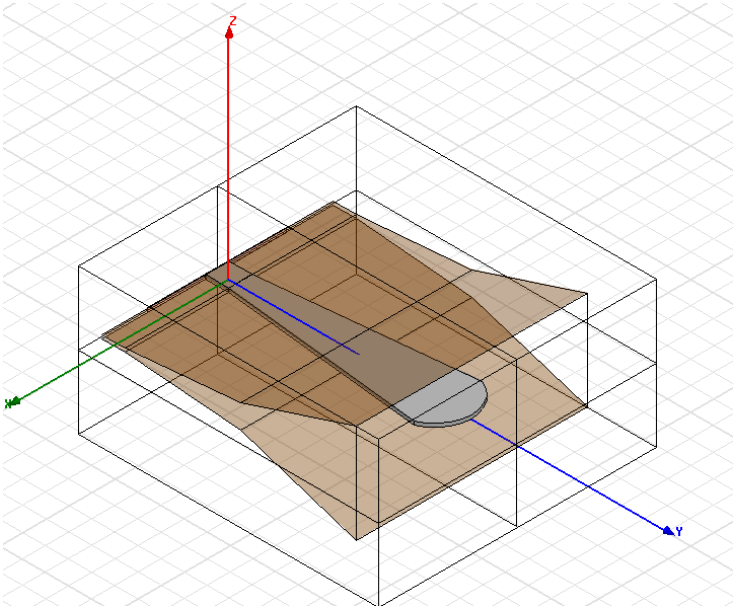

Fig 6.15 HFSS model for the improved dual air gap H-guide aperture horn antenna design shown in Fig. 6.14.

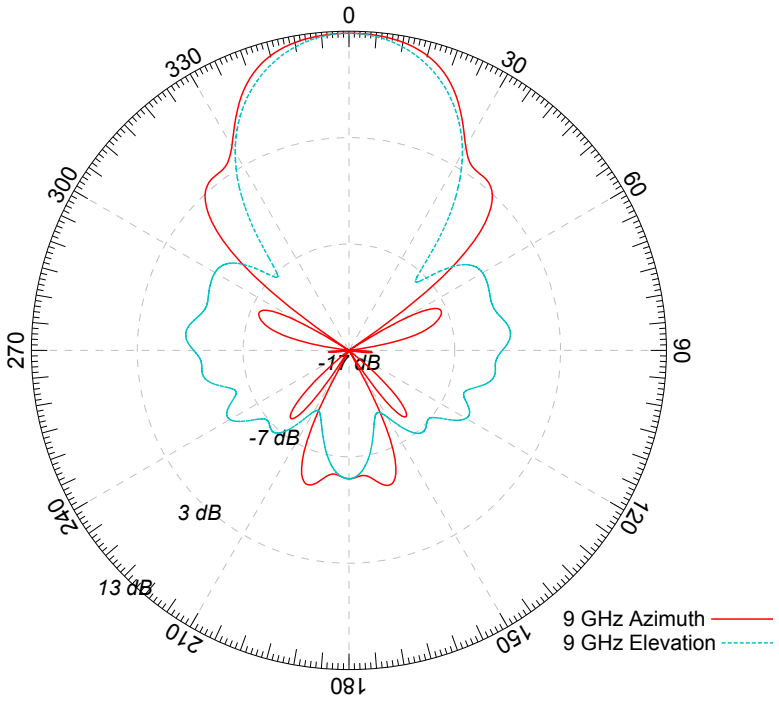

Fig 6.16(a) Antenna pattern at 9 GHz for the dual air gap H-guide aperture horn antenna simulation shown in Fig. 6.15. yz plane (H-plane, dot) and xy plane (E-plane, cross).

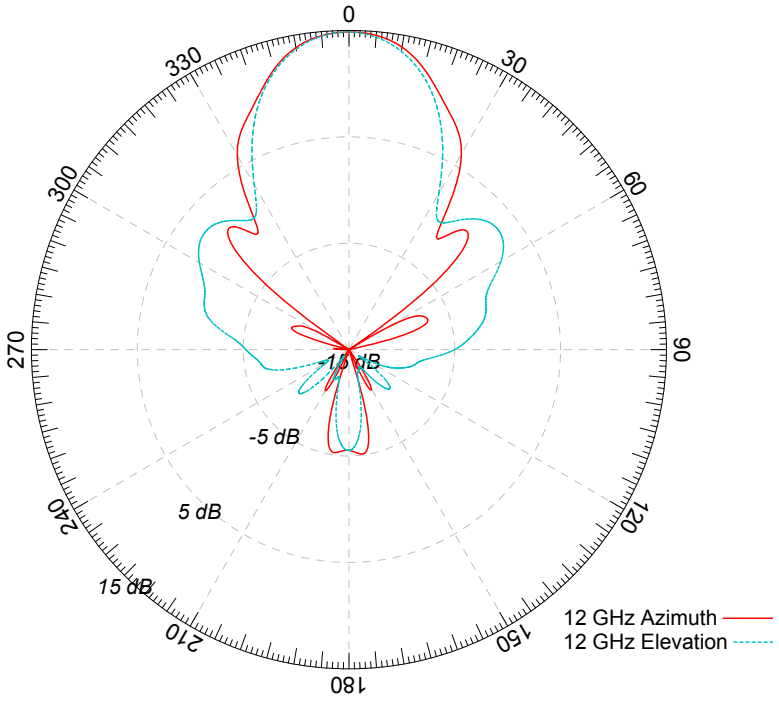

Fig 6.16(b) Antenna pattern at 12 GHz for the dual air gap H-guide aperture horn antenna simulation shown in Fig. 6.15. yz plane (H-plane, dot) and xy plane (E-plane, cross).

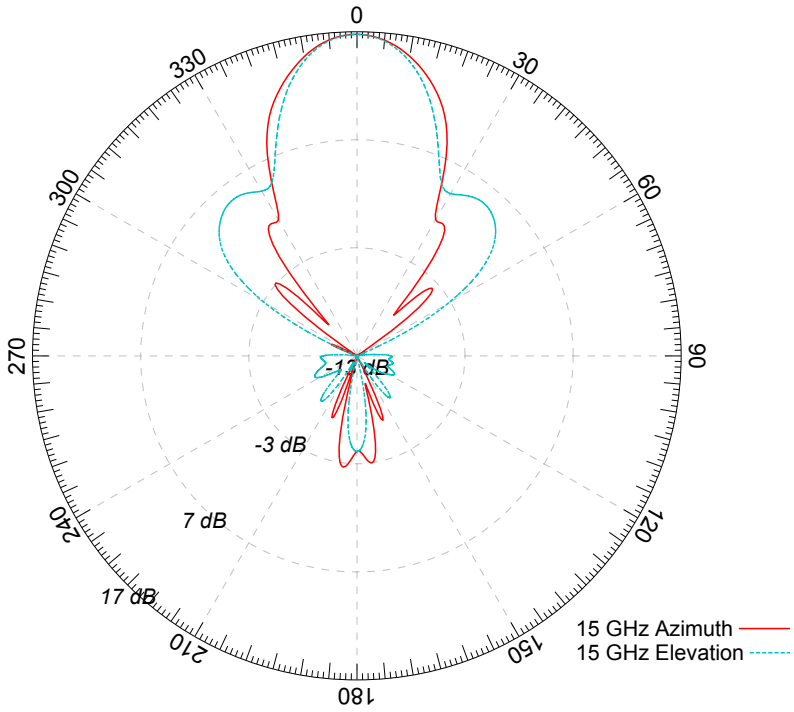

Fig 6.16(c) Antenna pattern at 15 GHz for the dual air gap H-guide aperture horn antenna simulation shown in Fig. 6.15. yz plane (H-plane, dot) and xy plane (E-plane, cross).

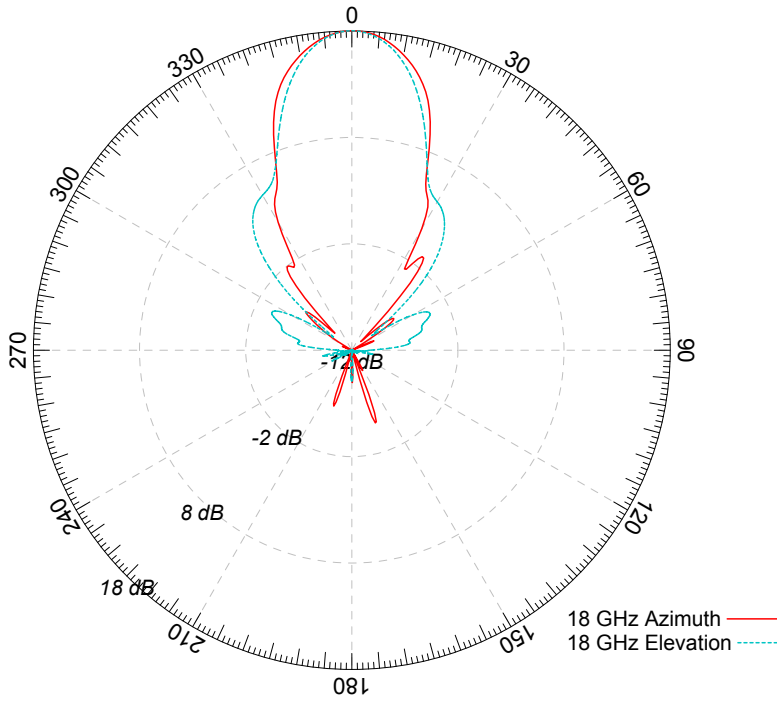

Fig 6.16(d) Antenna pattern at 18 GHz for the dual air gap H-guide aperture horn antenna simulation shown in Fig. 6.15. yz plane (H-plane, dot) and xy plane (E-plane, cross).

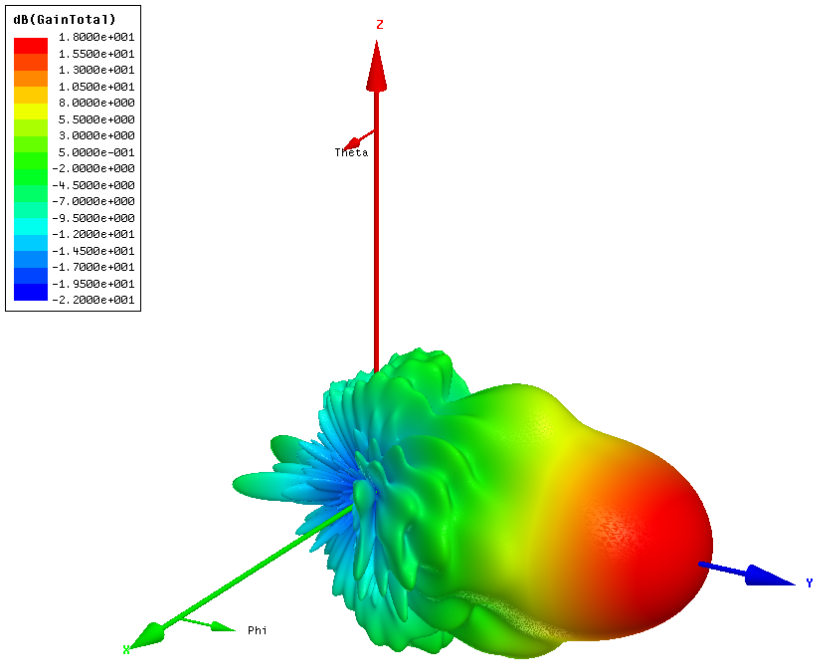

Fig. 6.17 Three-dimensional antenna pattern at 18 GHz for the antenna shown in Fig. 6.15.

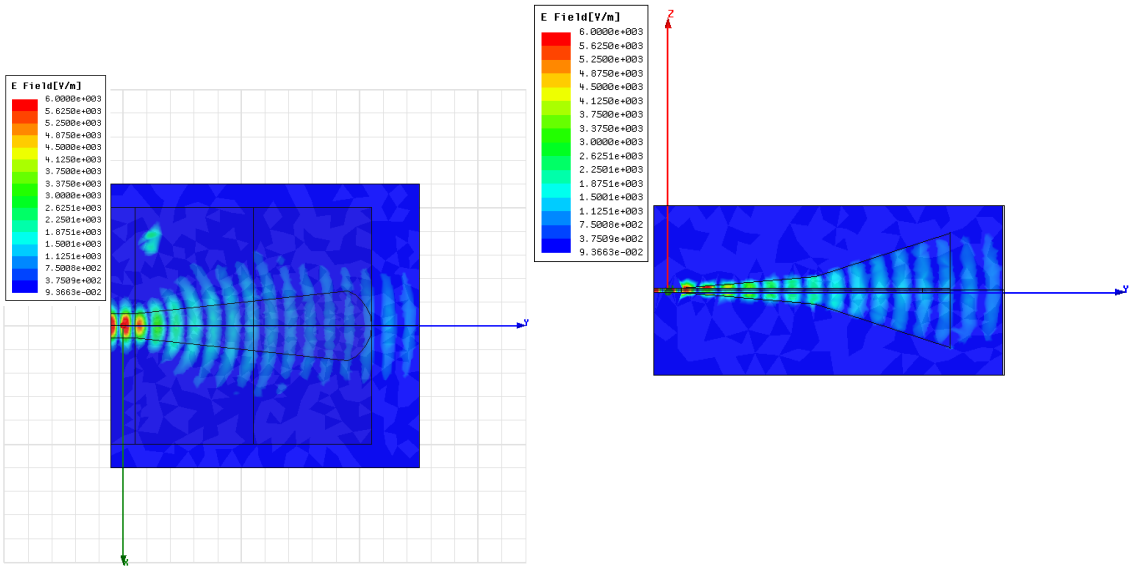

Fig. 6.18 Magnitude of the electric field at 18 GHz for the antenna shown in Fig. 6.15. Note that the phase is almost linear at the mouth of the horn, and *virtually no fringing* occurs at the metallic edges of the aperture, which both reduce sidelobe levels.

In this design, the simulation shows that this antenna exceeds a return loss of 10 dB from 7 to 18 GHz while achieving a gain that varies between 12 and 18 dBi as shown in Fig. 6.19.

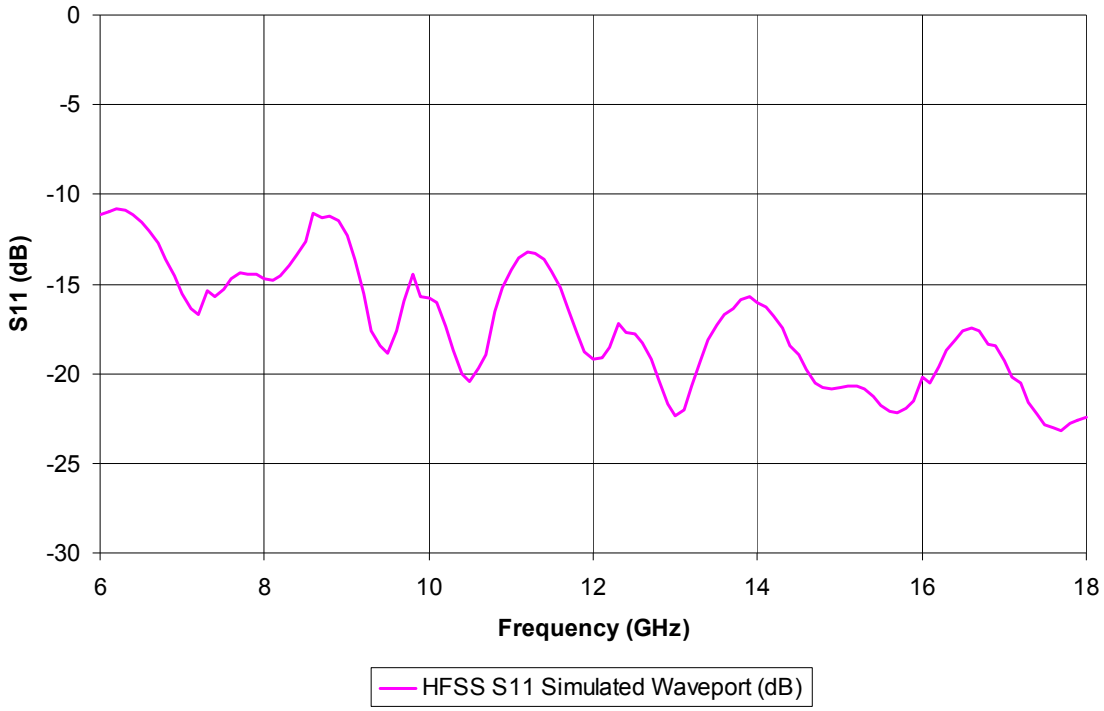

Fig 6.19. Measured vs. Simulated return loss for the antenna shown in Fig 6.15.

The width of the dielectric slowly increases to compensate for the loss in effective dielectric constant as the air gap widens. A two-stage design, with a smaller angle θ_1 to improve return loss, and a large angle, θ_2 is used to widen the aperture and thus improve gain. Finally, to speed up the wave at the aperture and thus adjust the phase, a curved shape with radius HW / 2 is cut into the dielectric. The three dimensional view of the antenna is shown in Fig. 6.15.

Some advantages of this design are that the wave exiting the aperture is nearly planar, and is mostly concentrated in the dielectric, away from metallic edges in the vertical direction, and with no metallic side walls required. The concentration away from metallic edges in the vertical direction reduces sidelobes, as does the absence of metallic side walls.

6.5 Complete Antenna Design and Measurement

In this section, the complete antenna design is discussed, where the microstrip to H-guide transition from Chapter 5 is used to excite the fundamental TE_{00} mode in the H-guide. The complete design is shown in Fig. 6.20 below with the magnitude of the electric fields at 15 GHz.

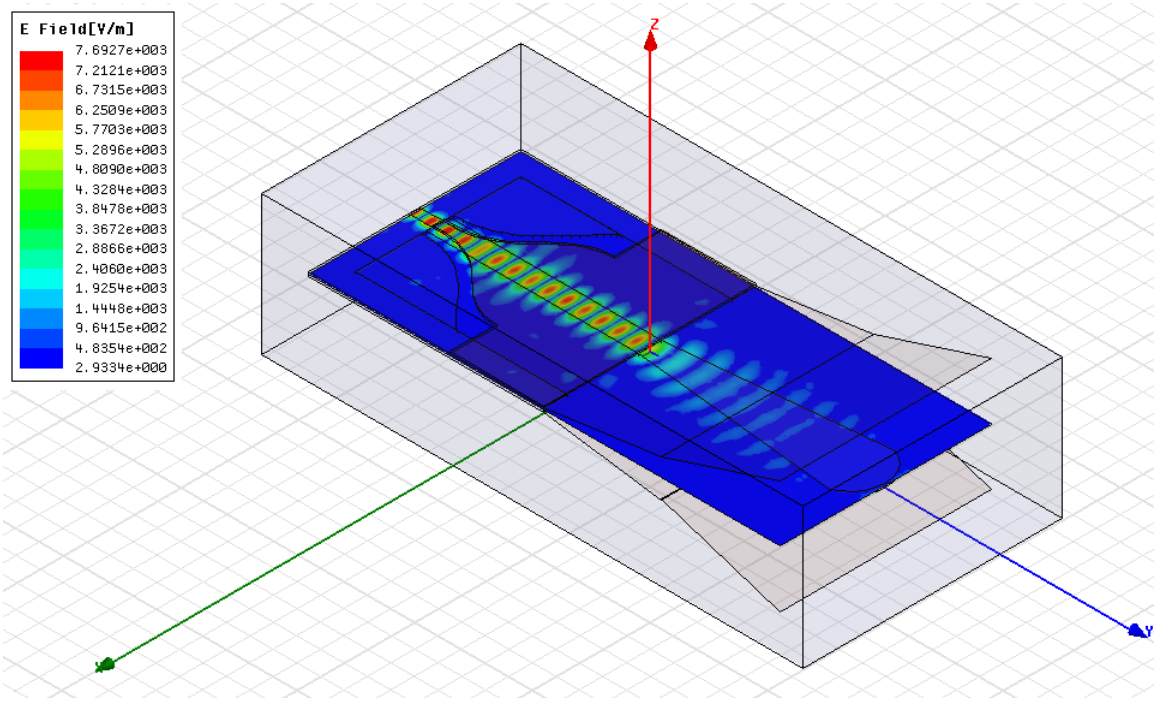

Fig. 6.20 Complete H-guide aperture antenna design. The H-guide antenna structure is fed using a microstrip to H-guide transition.

Of course, the addition of a non-ideal excitation source (as compared to a waveport) may lead to the excitation of higher order modes or leakage. At 15 GHz, however, the behavior of the electric fields are acceptable as can be seen in Fig. 6.20. Very little leakage is seen on either side of the centre dielectric structure.

The assembled structure is shown in Fig. 6.21. Top and bottom metallic plates are formed using sheets of single-sided copper-clad FR4. Partial bends in the substrate are possible by partially cutting into the substrate, which is fiberglass-reinforced. The remaining substrate and metal allow for the bend to keep its shape.

(a)

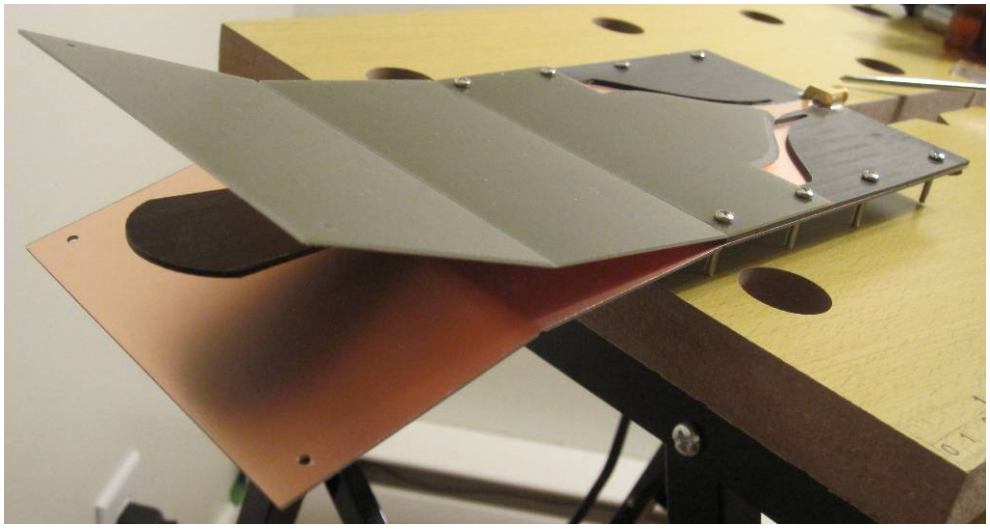

(b)

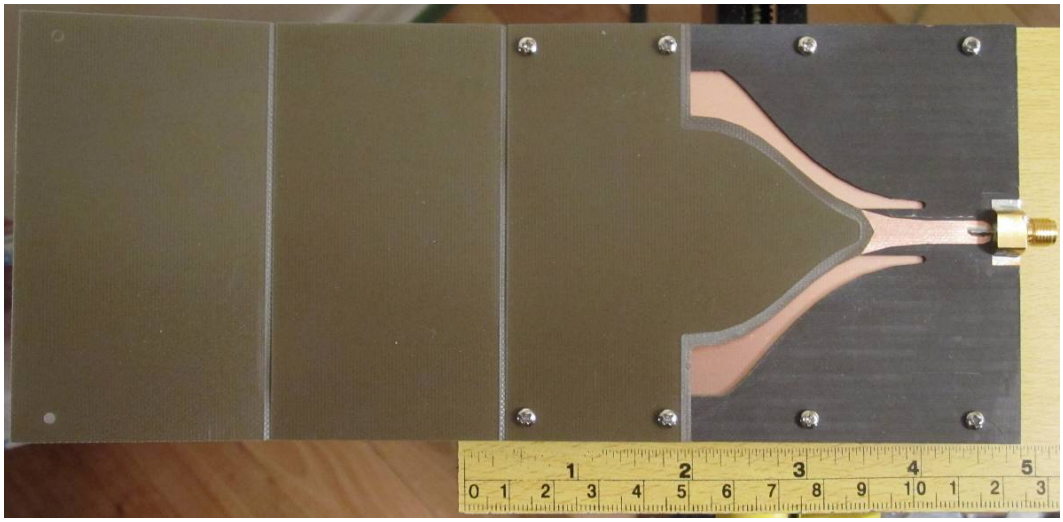

(c)

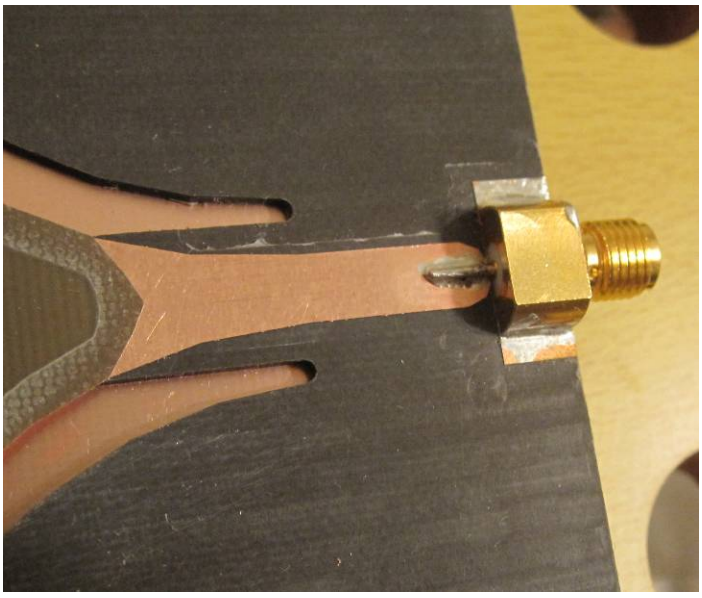

(d)

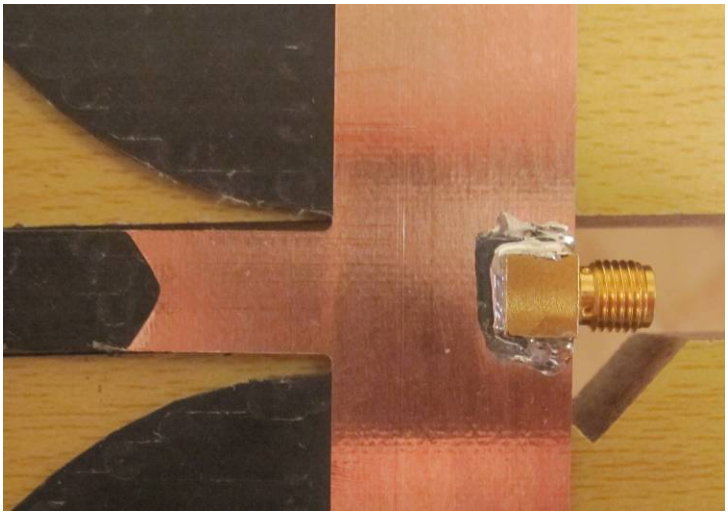

(e)

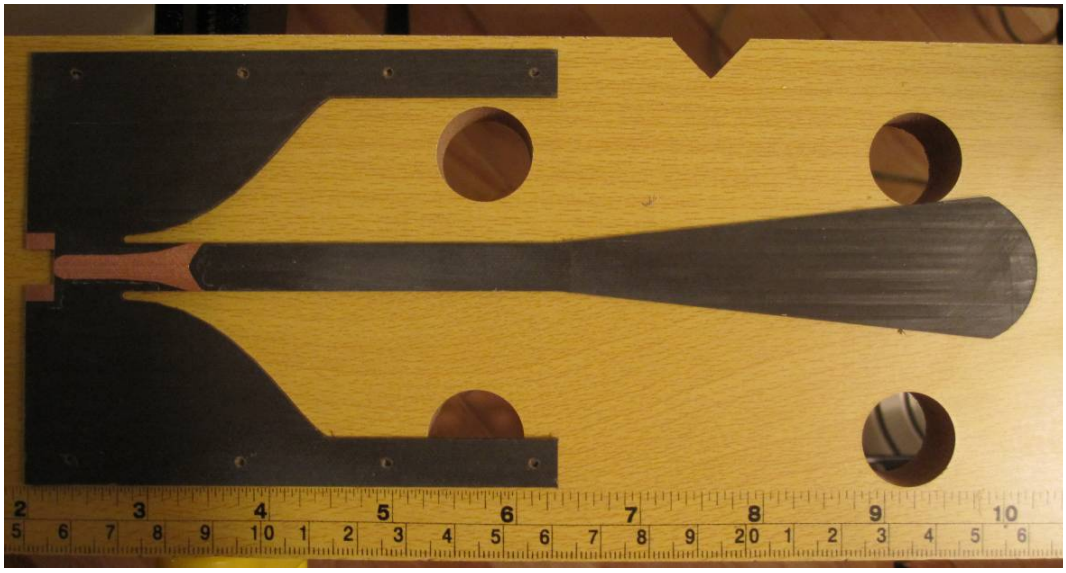

Fig. 6.21. (a) Three dimensional view of assembled H-guide aperture antenna using microstrip to H-guide transition. (b) Top view of assembled antenna. (c) Close-up top view of coaxial to microstrip connector. (d) Close-up bottom view of Rogers 5880 substrate before assembly. (e) Top view of Rogers 5880 substrate before soldering and assembly.

The return loss is compared between measured, simulated using a waveport, and simulated using the microstrip to H-guide transition in Fig. 6.22. The measured data includes a coaxial to microstrip transition that is not taken into account during simulations. Even though this was not taken into account, a reasonably close match is observed between measured and simulated results.

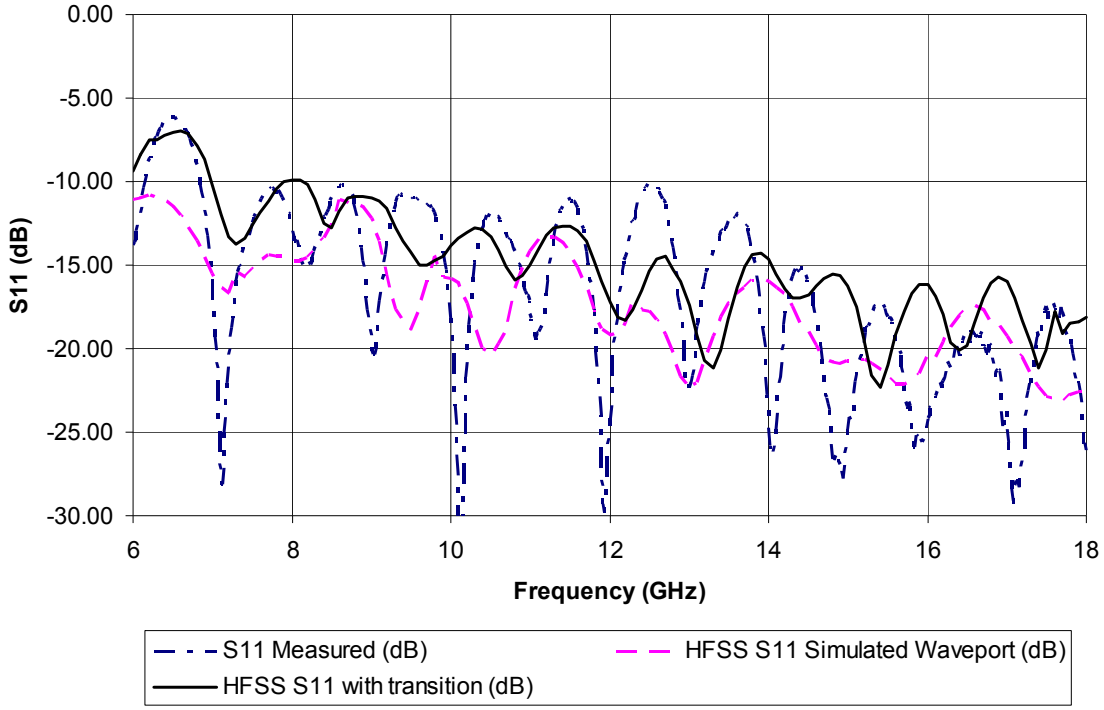

Fig. 6.22 Comparison of return loss (-S11) between simulation using a waveport, simulation using a microstrip-to-H-guide transition, and measured data.

The antenna azimuth and elevation patterns at 9 GHz are shown in Fig. 6.23, and Fig. 6.24, respectively. Similar behavior in the shape of the azimuth and elevation patterns can be seen, however, both patterns are degraded by the addition of the microstrip to H-guide transition.

At 12 GHz, the azimuth and elevation patterns are shown in Fig. 6.25 and Fig. 6.26, respectively. Again, the shapes of both the azimuth and elevation patterns are similar and are degraded by the addition of the transition.

At 15 GHz, the azimuth and elevation patterns are shown in Fig. 6.27 and Fig. 6.28, respectively. Sidelobes become apparent, however, the peak gain is still reasonable.

Differences between measured and simulated results are due to fabrication errors, and non-ideal effects of the FR4 substrate at higher frequencies. Some results of these effects include unwanted surface waves, or losses due to radiation at the edges of the top plate.

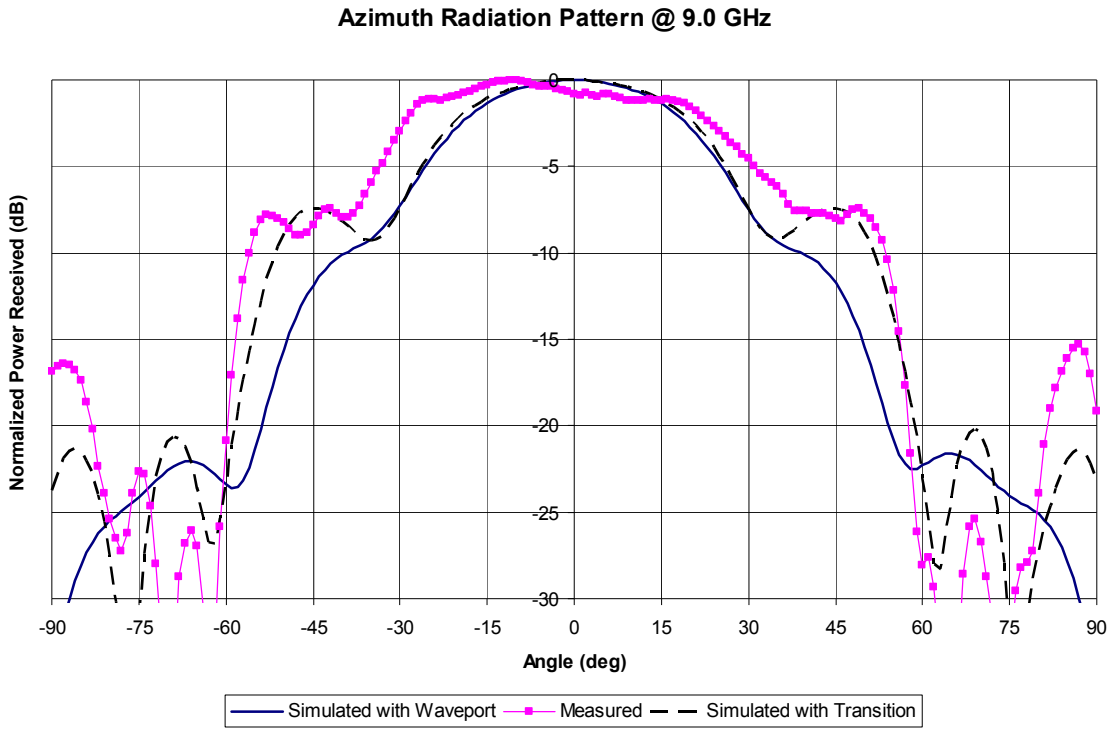

Fig. 6.23 Antenna azimuth radiation pattern at 9 GHz.

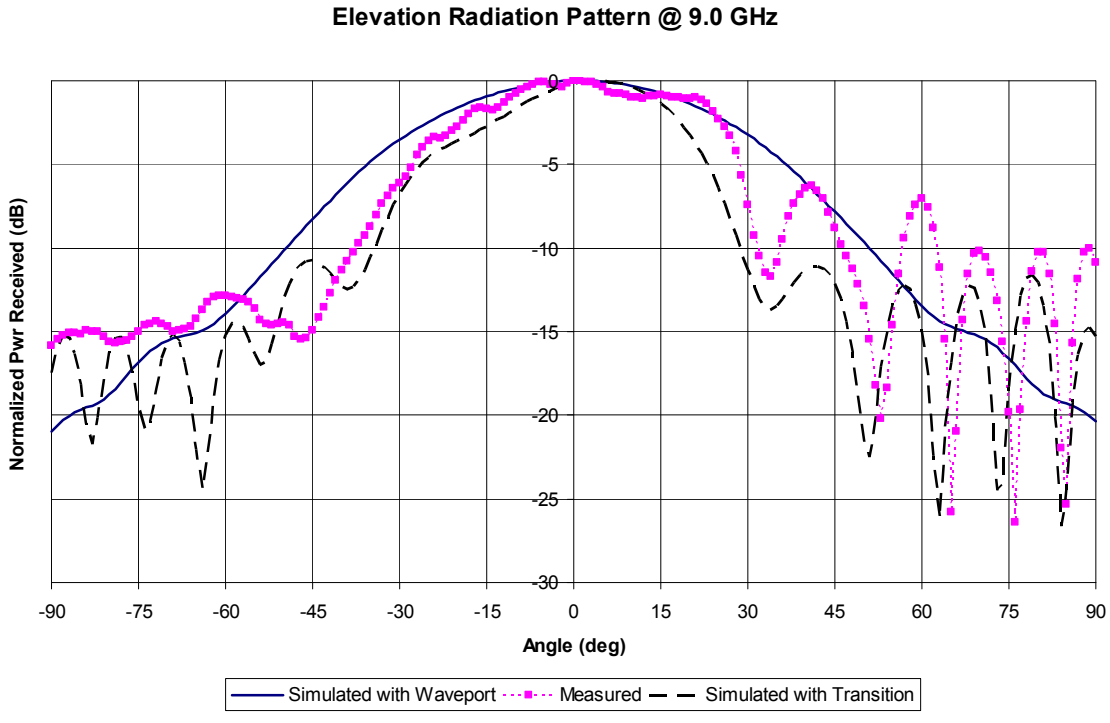

Fig. 6.24 Antenna elevation radiation pattern at 9 GHz.

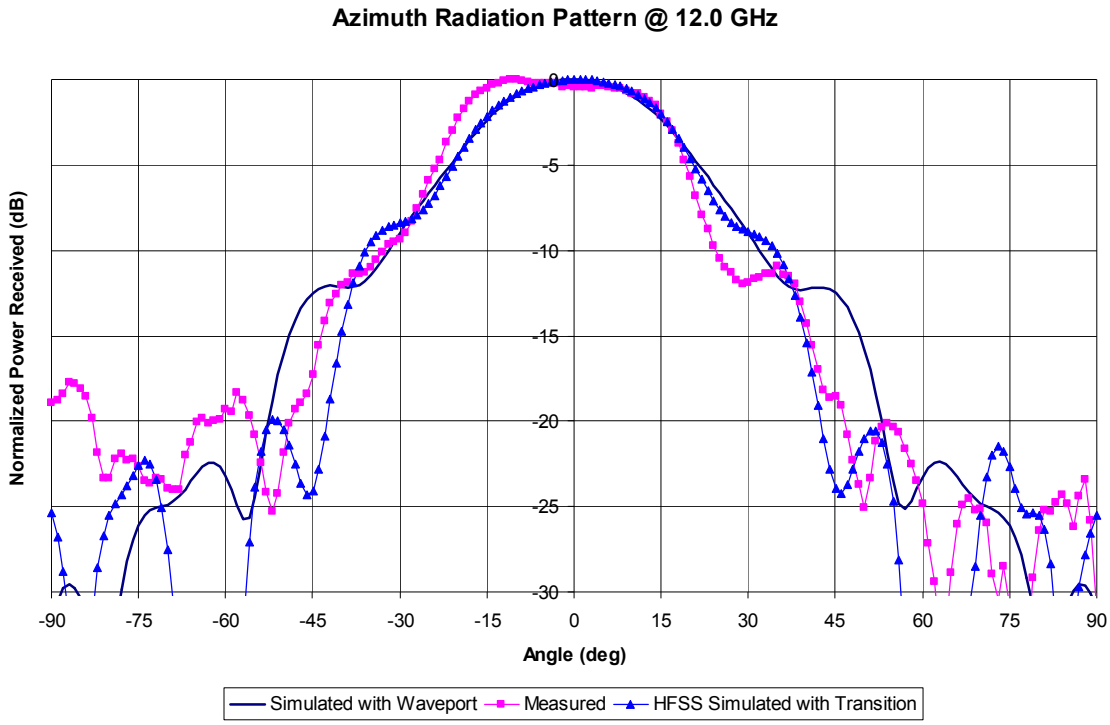

Fig. 6.25 Antenna azimuth radiation pattern at 12 GHz.

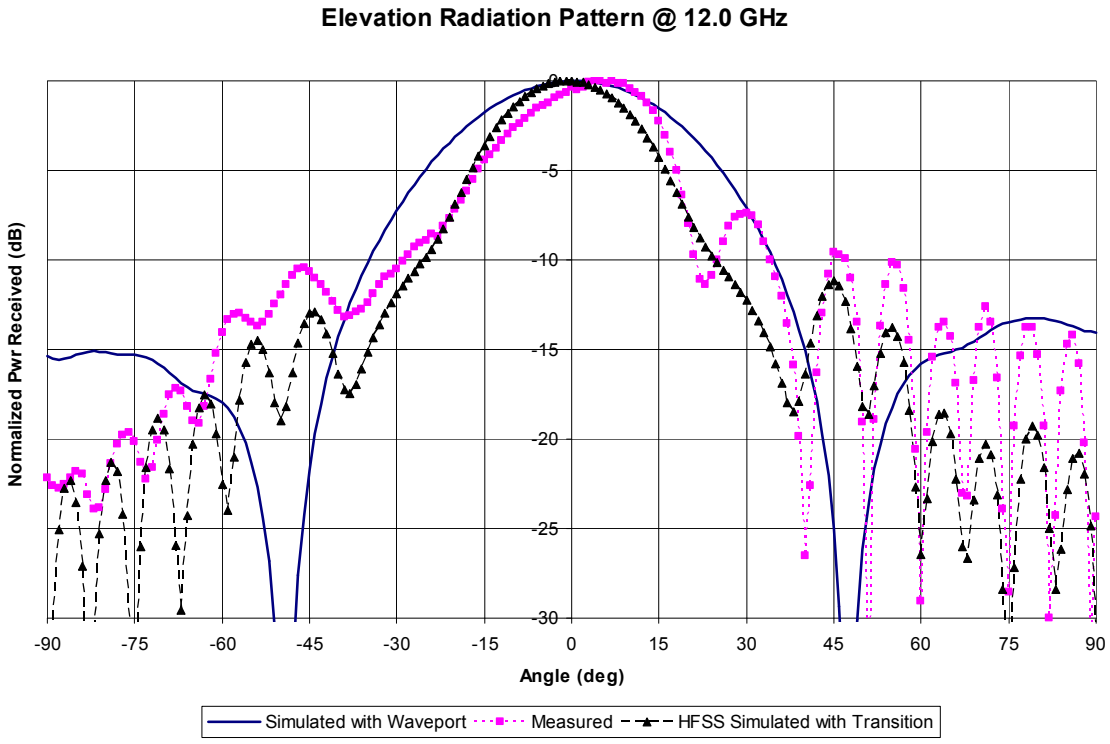

Fig. 6.26 Antenna elevation radiation pattern at 12 GHz.

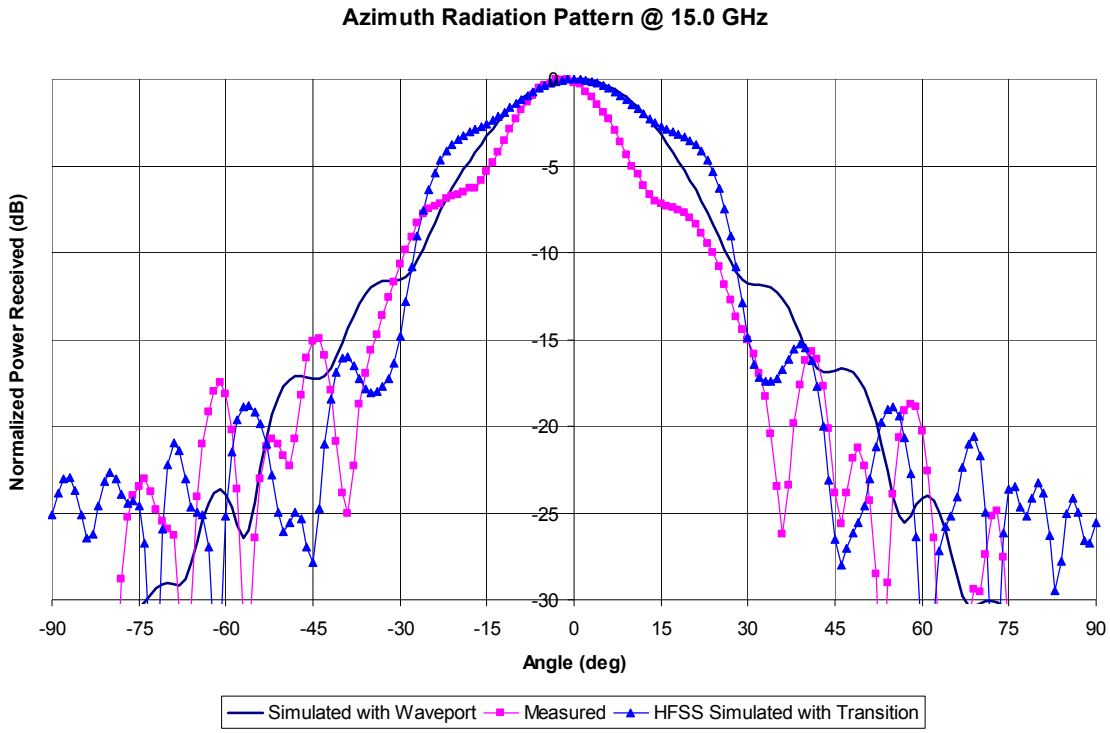

Fig. 6.27 Antenna azimuth radiation pattern at 15 GHz.

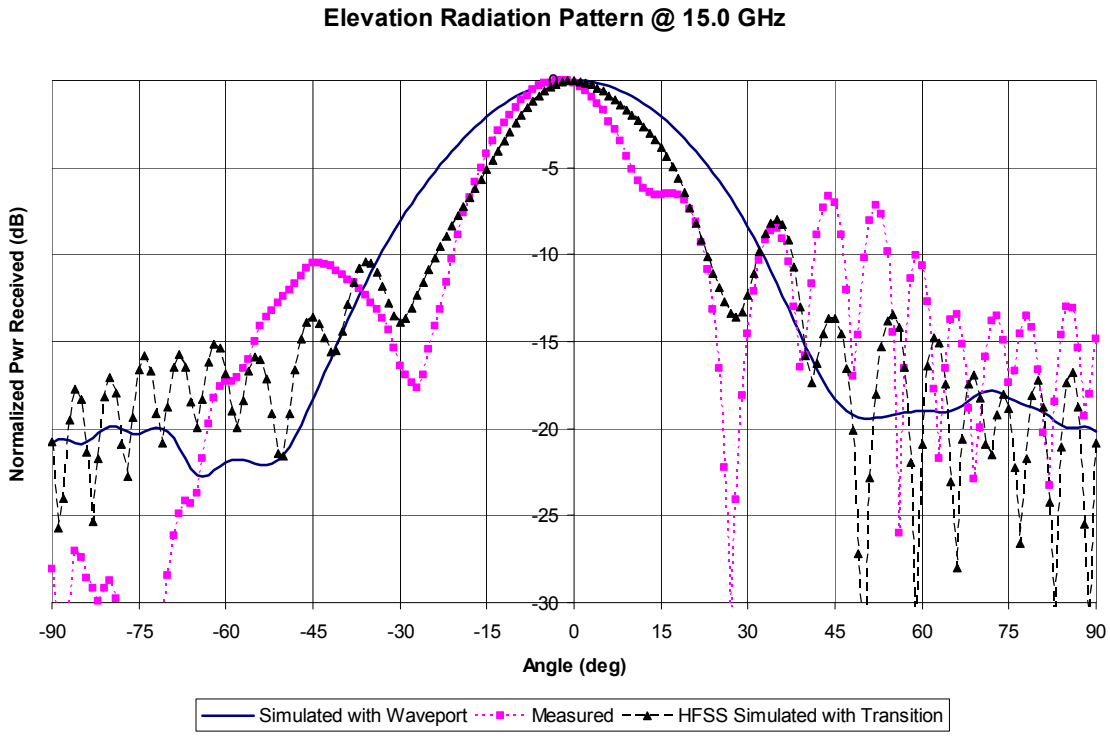

Fig. 6.28 Antenna elevation radiation pattern at 15 GHz. Sidelobes increase past 30 degrees due to leakage from the transition.

6.6 Summary

In this chapter, the design and simulation and measurement of the H-guide aperture horn antenna has been discussed. Simulation using a waveport is discussed, as well as simulation, fabrication, and measurement using a microstrip to H-guide transition. A very good match between simulation and measured return loss is observed. Antenna patterns, however, are degraded in the sidelobes due to leakage caused by the transition structure.

Chapter 7: H-Guide Dual Directional Coupler

In this chapter, the design of an H-guide Dual Directional Coupler is briefly investigated. Such a device is useful for test and measurement equipment and has been used for optical devices [33]. Non-Radiative Dielectric (NRD) guide couplers have been designed by using slots in a metallic plate [63], or by using a slab of dielectric [64] between two dielectric waveguide transmission lines. In these applications, forward and reverse power of the transmitted power can be measured very precisely. These results can subsequently used to

a) find the impedance of an unknown load
b) measure transmitted and reflected power for an H-guide antenna
c) find the bandwidth of a matching circuit

etc…

7.1 The Thin Single-Mode H-Guide

Consider a 4 mm wide H-guide formed using Rogers 6006 low loss substrate and copper plates. Transmission parameters for the fundamental and first odd modes are then simulated using HFSS [36] with waveports as shown in Fig. 7.1.

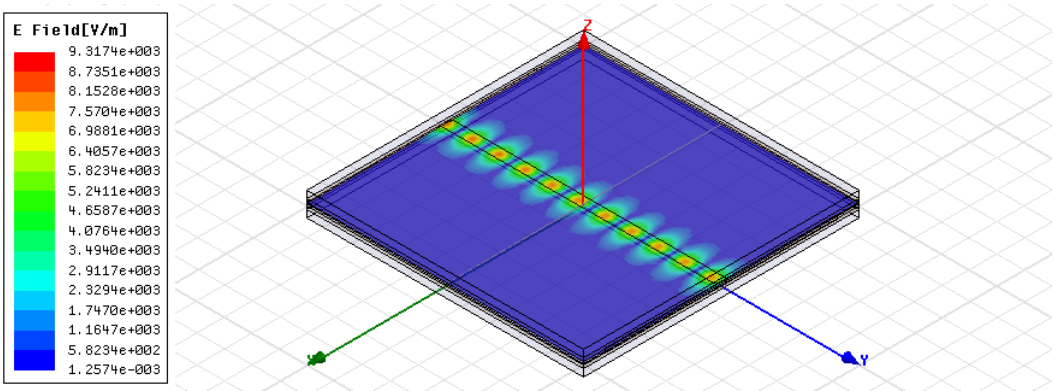

Fig. 7.1 Magnitude of the electric field within a 4 mm H-guide formed with Rogers 6006.

Transmission parameters for a 10 cm long section of H-guide are plotted in Fig. 7.2. The cutoff frequency for the first odd mode can be found using equations in [11] for an infinite slab dielectric waveguide. For a 4 mm wide slab of Rogers 6006, the cutoff frequency is 16.5 GHz and is marked approximately on Fig. 7.2 with a dotted line.

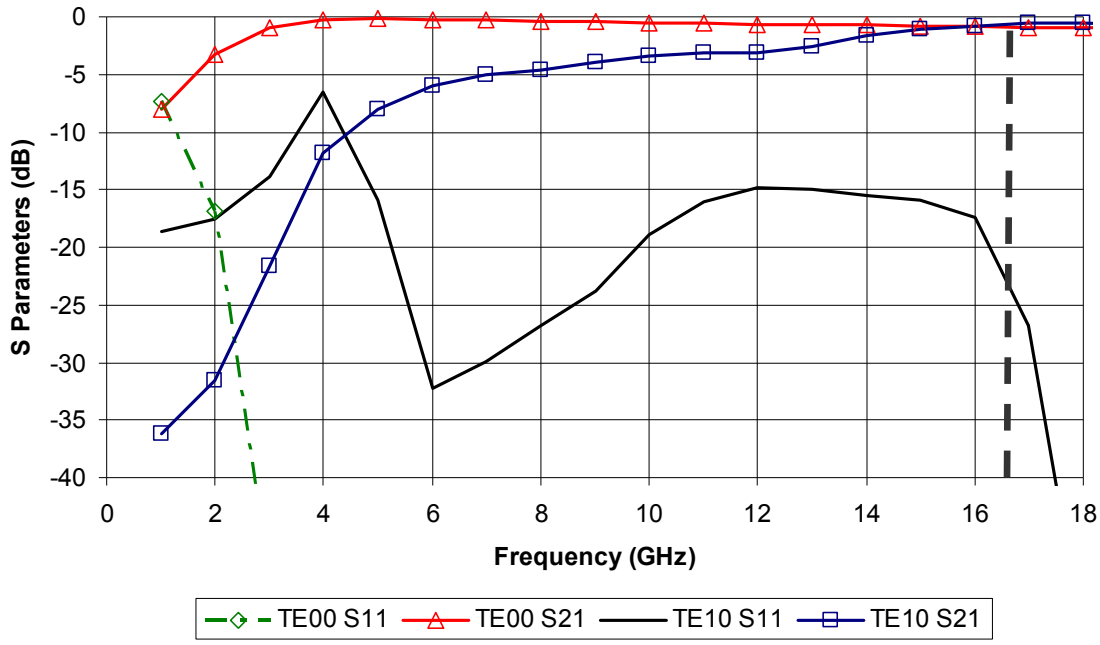

Fig. 7.2 Transmission parameters for a 4 mm H-guide using Rogers 6006.

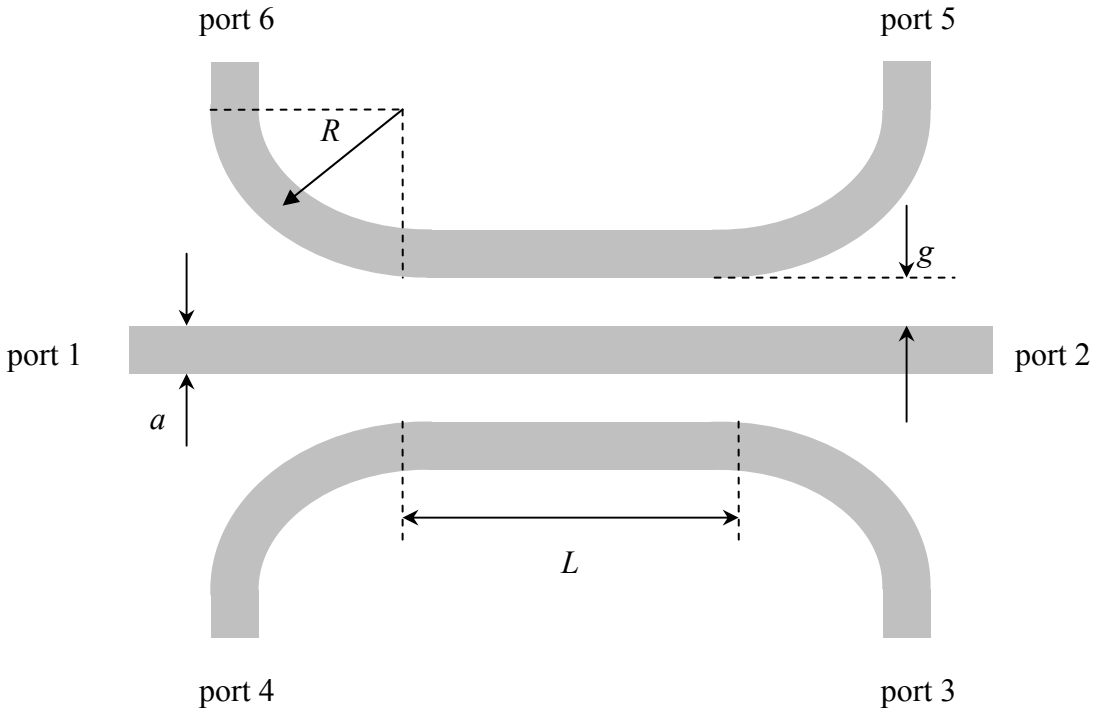

Fig. 7.3 Externally terminated dual directional H-guide coupler design. Length, *L* = 40 mm. Gap, *g* = 8 mm. Curve Radius, *R* = 35 mm. Substrate is Roger 6006 with height 1.27 mm, with an H-guide width, *a* = 4 mm.

7.2 Coupler Design

For this design, a single, 4 mm wide H-guide made of Rogers 6006 carries the signal from the input (Port 1) to the output (Port 2) as shown in Fig. 7.3. Dual curved H-guides couple energy from the main line to the coupled ports 3, 4, 5, and 6. These two sections suppress the formation of odd modes because the structure is symmetric.

The functionality of the externally terminated dual directional coupler can be described as follows. Input power is sent through port 1 and port 2 is connected to the unknown load. A small portion of the power is sent into ports 3 and ports 5. If port 3 is assigned to be the forward port, then port 4 and port 5 are externally terminated. Port 6 will then measure a portion of the power reflected back from port 2 into port 1, the input port.

A plot of the electric field at 14 GHz when port 1 is excited is shown in Fig. 7.4 below. A portion of the power from port 1 is coupled into ports 3 and 5.

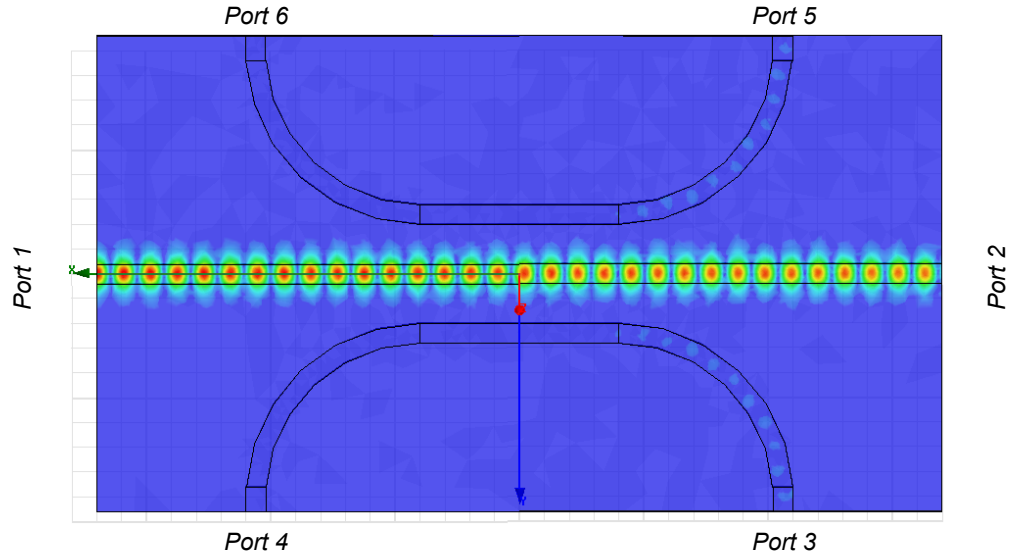

Fig. 7.4 A plot of the magnitude of the electric field inside the externally terminated dual directional coupler at 14 GHz.

The scattering parameters of the coupler are shown in Fig. 7.5. The insertion loss (-S21), or amount of power that is lost from port 1 to port 2, varies from 5 dB at 9 GHz to 1 dB at 14 GHz. The return loss (-S11) is better than 35 dB over the entire frequency range. The coupling (-S31) varies from 5 dB at 8 GHz to roughly 22 dB at 14 GHz. Although an

ideal coupler has constant coupling over the frequency range, for measurement devices, this factor can easily be "calibrated out" by simply taking the coupling factor into account in the calculations. The most important parameter, however, for a dual directional coupler is its directivity, or how much the coupler can discriminate between forward and reverse waves [1]. The directivity exceeds 25 dB between 8 and 13.5 GHz. Single mode, coupled dielectric lines have been analyzed in [65].

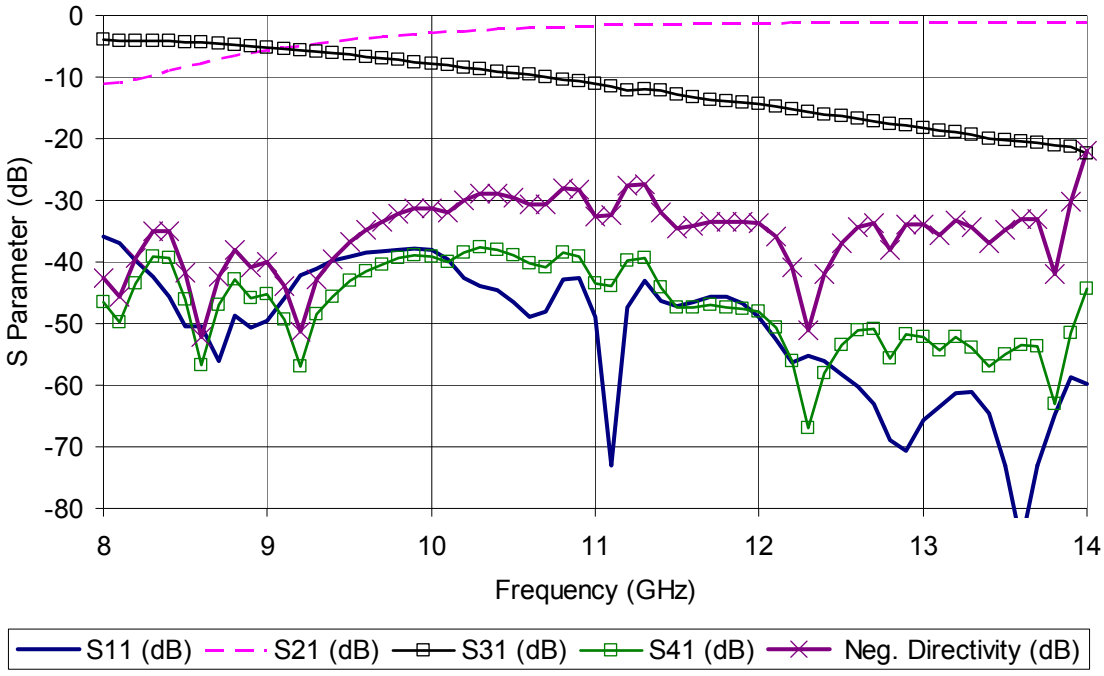

Fig. 7.5 S-parameters and directivity for the externally terminated dual directional coupler.

7.3 Summary

In this chapter, the design and simulation of a single mode H-guide dual directional coupler has been discussed. Directivity was found to be better than 25 dB from 8 to 14 GHz, while return loss was better than 30 dB.

Chapter 8: Conclusions and Future Work

In this thesis, it is shown that a relationship exists between dielectric waveguides, EBG structures, H-guide antennas, and H-guide directional couplers. Two dimensional EBG structures bounded by metallic plates can be modeled as coupled H-guides. Based on this model, a technique to predict the frequency response through such a structure has been developed. A new microstrip to H-guide wideband transition was designed to measure the structure as well as feed a new type of wideband, high gain, low sidelobe H-guide based aperture horn antenna. Finally, dual directional coupler confirms that the H-guide can be used for microwave circuit designs.

8.1 Contributions

The main contributions from this Ph.D. thesis include

- A new type of EBG structure that allows energy to pass instead of being blocked was presented in [38]. We have subsequently termed this structure a "band pass" structure, EBP.
- An antenna based on this EBP structure [38] was presented in [39].
- An optimized periodic structure as compared to [38] has been presented in [46]. This structure [46] contains only a single H-guide that guides energy instead of several coupled H-guides as in [38].
- A new wideband, low loss microstrip to H-guide transition structure has been presented in [48].
- In [61], a high gain antenna based on this transition structure has been presented.
- The analysis of a periodic H-guide structure presented in Chapter 4 has been submitted for a 2nd revision [66].
- The improved and measured dual gapped H-guide aperture antenna presented in Chapter 6, along with the transition presented in Chapter 5, will be combined and submitted as a full length journal paper.

- The directional coupler presented in Chapter 7 will be constructed and sent as a shorter submission. It has been accepted for publication as a conference paper for AP-S 2010 in Toronto [67].

8.3 Future Work

It is hoped that this thesis will be the basis for much further research work. In particular, the microstrip to H-guide transition proposed in this paper will allow

1) the design of efficient, new high gain antennas
2) the measurement of complex periodic structures in the form of EBG or perhaps even metamaterial structures
3) the design of compact waveguide-like microwave devices, such as the dual directional coupler

In addition, the periodic structure analysis presented in this thesis allows for much new research. Specifically, since the "inverse" operation exists, a structure that meets a certain frequency response or phase may be designed, given a certain criteria. A negative phase structure, for example, could in theory be designed using this theory. Several simplifications in the analysis were made so that the method is easier to understand, however, it should be easy to see that a more precise model based on this method will yield improved accuracy.

References

[1] D. M. Pozar, *Microwave Engineering*, John Wiley & Sons, New Jersey, 2005.

[2] Tischer, F.J. "H Guide with Laminated Dielectric Slab," IEEE Transactions on Microwave Theory and Techniques, Vol. 18, Issue 1, pp. 9–15, Jan 1970.

[3] S. G. Johnson, A. Mekis, S. Fan, J. D. Joannopoulos, "Molding the flow of light," Computing in Science & Engineering, Vol. 3, Issue 6, pp. 38-47, Nov.-Dec. 2001.

[4] F. Bloch, Z. Phys. 52, 555 (1928).

[5] L. Brillouin, *Wave Propagation in Periodic Structures: Electric Filters and Crystal Lattices*, McGraw Hill, New York, 1946.

[6] L. Brillouin, *Wave Propagation and Group Velocity*, Leon Brillouin, Academic, New York, 1960.

[7] K. Busch, S. John, "Liquid-Crystal Photonic-Band-Gap Materials: The Tunable Electromagnetic Vacuum," Physical Review Letters, Vol. 83, No. 5, 2 August 1999.

[8] E. Yablonivitch, "Inhibited Spontaneous Emission in Solid-State Physics and Electronics," Physical Review Letters, Vol 58, No. 20, 18 May 1987.

[9] R.F. Harrington, *Time Harmonic Electromagnetic Fields*, IEEE Press, Piscataway, New Jersey, 2001.

[10] C. A. Balanis, Advanced Electromagnetics. John Wiley & Sons, 1989.

[11] R. E. Collin, Field Theory of Guided Waves, Second Edition. IEEE Press, 1991, New Jersey, pp. 712–716.

[12] Y. Konishi, "Novel dielectric waveguide components-microwave applications of new ceramic materials," Proceedings of the IEEE, Vol. 79, Issue 6, pp. 726-740, June 1991.

[13] B. J. Mangan, L. Farr, A. Langford, P. J. Roberts, D. P. Williams, F. Couny, M. Lawman, M. Mason, S. Coupland, R. Flea, H. Sabert, T. A. Birks, J. C. Knight, P. St. J. Russell, "Low loss (1.7 dB/km) hollow core photonic bandgap fiber," Optical Fiber Communication Conference, p. 3, Vol. 2., 23-27 Feb. 2004.

[14] R. F. Cregan, B. J. Mangan, J. C. Knight, T. A. Birks, P. St. J. Russell, P. J. Roberts, D. C. Allan, "Single-Mode Photonic Band Gap Guidance of Light in Air", Science Magazine, issue 285, p. 1537, 1999.

[15] J.D. Joannopoulos, R. Meade, J. Winn., *Photonic Crystals: Molding the flow of light*. Princeton University Press, Princeton, New Jersey, 1995.

[16] F.B. McCormick, J.G. Fleming, S. Mani, M.R. Tuck, J.D. Williams, C.L. Arrington, S.H. Kravitz, C. Schmidt, G. Subramania, J.C. Verley, A.R. Ellis, I. El-kady, D.W. Peters, M. Watts, W.C. Sweatt, J.J. Hudgens, "Fabrication and characterization of large-area 3D photonic crystals," 2006 IEEE Aerospace Conference, 8 pages, 4-11 March 2006.

[17] A.R. Weily, K.P. Esselle, T.S. Bird, B.C. Sanders, "Linear array of woodpile EBG sectoral horn antennas," IEEE Transactions on Antennas and Propagation, Vol. 54, Issue 8, pp. 2263-2274, Aug. 2006.

[18] B. Martinez, I. Ederra, R. Gonzalo, B. Alderman, L. Azcona, P.G. Huggard, Bas de Hon, A. Hussain, S.R. Andrews, L. Marchand, P. de Maagt, "Manufacturing Tolerance Analysis, Fabrication, and Characterization of 3-D Submillimeter-Wave Electromagnetic-Bandgap Crystals," *IEEE Transactions on Microwave Theory and Techniques*, Vol. 55, Issue 4, pp. 672-681, April 2007.

[19] F. Gadot, A. Ammouche, A. de Lustrac, A. Chelnokov, F. Bouillault, P. Crozat, J. M. Lourtioz, "Photonic band gap materials for devices in the microwave domain," IEEE Transactions on Magnetics, Vol. 34, Issue 5, Part 1, pp. 3028-3031, Sept. 1998.

[20] S. John, "Strong Localization of Photons in Certain Disordered Dielectric Superlattices," Physical Review Letters, Vol. 58, No. 23, 8 June 1987.

[21] A.R. Weily, K.P. Esselle, T.S. Bird, B.C. Sanders, "Experimental woodpile EBG waveguides, bends and power dividers at microwave frequencies," Electronics Letters,Vol. 42, Issue 1, pp. 32-33, 5 Jan. 2006.

[22] R. W. Ziolkowski, Masahiro Tanaka, "FDTD analysis of PBG waveguides, power splitters and switches," Journal Optical and Quantum Electronics, Vol. 31, pp. 843-855, Oct 1999.

[23] Chi-Yang Chang, Wei-Chen Hsu, “Photonic Bandgap Dielectric Waveguide Filter,” IEEE Microwave And Wireless Components Letters, Vol. 12, No. 4, p. 137, April 2002.

[24] L. Han, K. Wu, R. G. Bosisio, “An integrated transition of microstrip to nonradiative dielectric waveguide for microwave and millimeter-wave circuits,” IEEE Transactions on Microwave Theory and Techniques, Vol. 44, Issue 7, Part 1, pp. 1091 – 1096. July 1996.

[25] J. A. G. Malherbe, J. H. Cloete, L. E. Losch, "A Transition from Rectangular to Nonradiating Dielectric Waveguide," Short Papers in IEEE Transactions on Microwave Theory and Techniques, Vol. 33, No. 6, pp. 539-543, June 1985.

[26] H. Sugimoto, F. Kuroki, T. Yoneyama, "Performance Improvement of NRD Guide / Microstrip Line Transition at 60 GHz," Asia-Pacific Microwave Conference, 2007. APMC 2007, pp. 1-4, 11-14 Dec. 2007.

[27] F. Kuroki, M. Kimura, T. Yoneyama, "A transition between NRD guide and microstrip line at 60 GHz,"2004 34th European Microwave Conference," Vol. 2, pp. 765-768, 13 Oct. 2004.

[28] J. A. G. Malherbe, "The Design Of A Slot Array In Nonradiating Dielectric Waveguide, Part I: Theory," IEEE Transactions On Antennas And Propagation, Vol. Ap-32, No. 12, pp. 1335-1340, December 1984

[29] J. A. G. Malherbe, J. H. Cloete, I. E. Losch, M. W. Robson, and D. B. Davidson, "The Design Of A Slot Array In Nonradiating Dielectric Waveguide, Part II: Experiment," IEEE Transactions On Antennas And Propagation, Vol. Ap-32, No. 12, pp. 1341-1344, December 1984

[30] K. Maamria, T. Wagatsuma, T. Yoneyama, "Leaky NRD guide as a feeder for microwave planar antennas," IEEE Transactions on Antennas and Propagation, Vol. 41, Issue 12, pp. 1680-1686, Dec. 1993

[31] F. Bongard, J. Perruisseau-Carrier, J. R. Mosig, "Enhanced Periodic Structure Analysis Based on a Multiconductor Transmission Line Model and Application to Metamaterials," IEEE Transactions on Microwave Theory and Techniques, Vol. 57, Issue 11, pp. 2715-2726, Nov. 2009.

[32] A. Grbic, G. V. Eleftheriades, "Periodic analysis of a 2-D negative refractive index transmission line structure," IEEE Transactions on Antennas and Propagation, Vol. 51, Issue 10, Part 1, pp. 2604 - 2611, Oct. 2003.

[33] R. Youngquist, L. Stokes, H. Shaw, "Effects of normal mode loss in dielectric waveguide directional couplers and interferometers," IEEE Journal of Quantum Electronics, Vol. 19, Issue 12, pp. 1888 - 1896, Dec 1983.

[34] A. L. Topa, C. R. Paiva, A. M. Barbosa, "Novel propagation features of double negative H-guides and H-guide couplers, " Microwave and Optical Technology Letters, Vol. 47, Issue 2, pp. 185 - 190, 25 Aug 2005.

[35] A. L. Topa, C. R. Paiva, A. M. Barbosa, "Full-wave analysis of a nonradiative dielectric waveguide with a pseudochiral Ω-slab, " IEEE Transactions on Microwave Theory and Techniques, Vol. 46, Issue 9, pp. 1263 - 1269, September 1998.

[36] Ansoft HFSS, Version 10.1.2, Ansoft Corporation, Pittsburg, PA, Build 28 September 2006. Latest 2010 version is currently part of the ANSYS, Inc. portfolio.

[37] C. H. Kuo, Z. Ye, "Electromagnetic Energy and Energy Flows in a Photonic Crystal Made of Arrays of Parallel Dielectric Cylinders," Physical Review, Vol. 70, Issue 4, Paper 044617, 2004.

[38] M. Wong, A. R. Sebak, T. A. Denidni, "An EBG Waveguide for Microwave Frequencies," USNC / URSI National Radio Science Meeting, Accepted, San Diego, July 5-12, 2008.

[39] M. Wong, A. R. Sebak, T. A. Denidni, "A Via-Less EBG Horn Antenna," URSI General Assembly, Chicago, August 7-16, 2008.

[40] T. Yoneyama, S. Nishida, "Nonradiative dielectric waveguide for millimeter wave integrated circuits," IEEE Transactions on Microwave Theory and Techniques, Vol. 29, Issue 11, pp. 1188–1192, Nov. 1981.

[41] N. Michishita, T. Ueda, A. Lai, and T. Itoh, "Evanescent-mode dielectric metamaterial structure excited by NRD guide and its application to leaky wave antenna," 2007 IEEE Antennas and Propagation International Symposium, pp. 2345–2348, 9-15 June 2007.

[42] D. Li, P. Yang, K. Wu, “An order-reduced volume-integral equation approach for analysis of NRD-guide and H-guide millimeter-wave circuits,” IEEE Transactions on Microwave Theory and Techniques, Vol. 53, Issue 3, Part 1, pp. 799 – 812, Mar. 2005.

[43] D. C. Webb, R. A. Moore, “H guide for miniature microwave circuitry,” Proceedings of the IEEE, Vol. 51, Issue 2, pp. 384 – 384, Feb. 1963.

[44] Y. Cassivi, K. Wu, “Substrate integrated NRD (SINRD) guide in high dielectric constant substrate for millimetre wave circuits and systems,” 2004 IEEE MTT-S International Microwave Symposium Digest, Vol. 3, pp. 1639 – 1642, 6-11 Jun. 2004.

[45] E. Lidorikis, M. L. Povinelli, S. G. Johnson, and J. D. Joannopoulos, "Polarization-Independent Linear Waveguides in 3D Photonic Crystals", Phys. Rev. Lett., Vol 91, paper #023902, 2003.

[46] M. Wong, A. R. Sebak, T. A. Denidni, “Implementation of a Structurally Robust Periodic H-Guide,” USNC/URSI, Charleston, South Carolina, Jun. 1-5, 2009.

[47] J. Chenkin, “DC to 40 GHz coaxial-to-microstrip transition for 100-µm-thick GaAs substrates,” IEEE Transactions on Microwave Theory and Techniques, Vol. 37, Issue 7, pp.1147 – 1150, July 1989.

[48] M. Wong, A.R. Sebak, and T.A. Denidni, "Wideband Bézier curve shaped microstrip to H-guide transition," Electronics Letters, Volume 45, Issue 24, p.1250–1252, 19 November 2009.

[49] A. D. Olver, B. Philips, “Profiled dielectric loaded horns,” Eighth International Conference on Antennas and Propagation, Vol. 2, pp. 788 – 791, 1993.

[50] W. C. Song, S. C. Ou, and S. R. Shiau, “Integrated computer graphics learning system in virtual environment: case study of Bezier, B-spline and NURBS algorithms,” Proceedings of the 2000 IEEE International Conference on Information Visualization, pp. 33–38, 19-21 July 2000.

[51] Xiang-Yin Zeng, Kwai-Man Luk, Shan-Jai Xu, "Uncovered leakage phenomenon in H-guide slot antenna," 2nd International Conference on Microwave and Millimeter Wave Technology, ICMMT 2000, pp. 283-286, 14-16 Sept. 2000.

[52] M. Kisliuk, A. Axelrod, "Theoretical and Experimental Study of a Novel H-Guide Transverse Slot Antenna (Short Papers)," IEEE Transactions on Microwave Theory and Techniques, Vol. 33, Issue 5, pp. 428-433, May 1985.

[53] G. Voronoff, "H-guide log periodic slot antenna," Antennas and Propagation Society International Symposium, Volume 4, pp. 167-176, Dec 1966.

[54] H. Hasegawa, H. Shimasaki, M. Tsutsumi, "Millimetre wave leaky wave antenna using an H-guide loaded with a corrugated ferrite," IEE Proceedings on Microwaves, Antennas and Propagation, Volume 144, Issue 6, pp. 443-448, Dec. 1997.

[55] F.J. Tischer, "The Groove Guide, a Low-Loss Waveguide for Millimeter Waves," IEEE Transactions on Microwave Theory and Techniques, Vol. 11, Issue 5, pp. 291-296, Sep 1963.

[56] P. Bhartia, I.J. Bahl, Millimeter Wave Engineering and Applications, John Wiley & Sons, New York, 1984.

[57] P. Arcioni, M. Bressan, F. Broggi, G. Conciauro, P. Pierini, "The groove guide: a non-conventional interaction structure for microwave FEL experiments," Proceedings of the 1993 Particle Accelerator Conference, pp. 1569 - 1571 vol. 2, 17-20 May 1993.

[58] E. Lier, A. Kishk, "A new class of dielectric-loaded hybrid-mode horn antennas with selective gain: design and analysis by single mode model and method of moments," IEEE Transactions on Antennas and Propagation, Vol. 53, Issue 1, Part 1, pp. 125 – 138, Jan. 2005.

[60] F.J. Tischer, "Domino-Type Microwave and Millimeter-Wave Systems," 15th European Microwave Conference, pp. 721-725, Oct. 1985.

[61] M. Wong, A. R. Sebak, T. A. Denidni, "Gapped Radial H-Guide Aperture Antenna," 2009 IEEE International APS, Charleston, South Carolina, June 1-5, 2009.

[62] C. A. Balanis, Antenna Theory: Analysis and Design. John Wiley & Sons, 1997.

[63] L. Hong-Yeol, J. Dong-Suk, K. Dong-Young, L. Sang-Seok, C. Ik-Guen, "60GHz wideband directional coupler with non-radiative dielectric guide," 2005 European Microwave Conference, Vol. 2, 4-6 Oct. 2005.

[64] D.-C Niu, T. Yoneyama, T. Itoh, “Analysis and measurement of NRD-guide leaky wave coupler in Ka-band,” IEEE Transactions on Microwave Theory and Techniques, Vol. 41, Issue 12, pp. 2126 - 2132, Dec. 1993.

[65] E. A. J. Marcatili, Bell System Technical Journal, Vol 69, p. 2071, 1969.

[66] M. Wong, A. R. Sebak, T. A. Denidni, “Analysis, Simulation, and Measurement of Square Periodic H-Guide Structures,” submitted to IET for 2nd revision.

[67] M. Wong, A. R. Sebak, T. A. Denidni, “Dual Directional H-Guide Coupler ,” 2010 IEEE International APS, Toronto, Ontario, accepted, to be published.

[68] J. E. Goell, Bell System Technical Journal, Vol 69, p. 2133, 1969.

[69] K. S. Chiang, “Dual effective-index method for the analysis of rectangular dielectric waveguides,” Applied Optics, Vol. 25, No. 13, pp. 2169-2174, 1 July 1986.

[70] D. Deslandes, K. Wu, "Integrated microstrip and rectangular waveguide in planar form," IEEE Microwave and Wireless Components Letters, Vol. 11, no. 2, pp. 68-70, 2001.

Appendix A: The Infinitely Large Dielectric Slab Waveguide

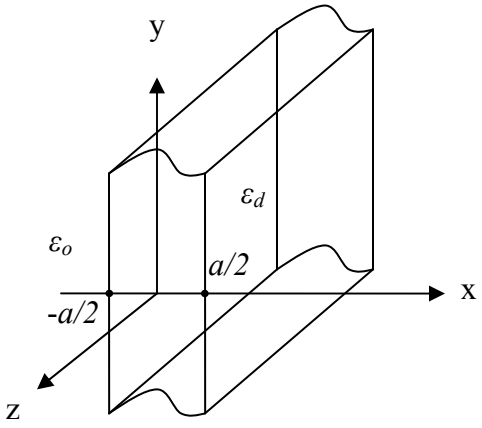

Fig. A.1 A two dimensional Dielectric Slab Waveguide of width "*a*" with dielectric constant ε_d is infinitely large in the y and z directions. It is sandwiched between a medium with dielectric constant ε_o. We wish to consider the propagation in the +z direction.

The following analysis follows a similar derivation for TM modes as outlined in [10].

In Chapter 2, we have assumed that since the dielectric slab is infinitely large in the y direction, the variation in the electric field in the y direction is 0, or

$$\frac{\partial E}{\partial y} = 0 \tag{A.1}$$

Here, we wish to consider TE_z propagation in the +z direction, where E_z =0, as shown in the simplified diagram in Fig. A.1. E_x and E_y may or may not be zero. We first assume a magnetic vector potential function

$$\overline{F} = \hat{a}_z F_z(x, y, z) \tag{A.2}$$

where the potential function F_z satisfies the wave equation

$$\nabla^2 F_z(x, y, z) + \beta^2 F_z(x, y, z) = 0 \tag{A.3}$$

To find the fields for TE_z modes we then evaluate the following derivatives to find the field components,

$$\begin{aligned} E_x &= -\frac{1}{\varepsilon}\frac{\partial F_z}{\partial y} \\ E_y &= \frac{1}{\varepsilon}\frac{\partial F_z}{\partial x} \\ E_z &= 0 \end{aligned} \tag{A.4}$$

$$\begin{aligned} H_x &= -\frac{j}{\omega\mu\varepsilon}\frac{\partial^2 F_z}{\partial x \partial z} \\ H_y &= \frac{j}{\omega\mu\varepsilon}\frac{\partial^2 F_z}{\partial y \partial z} \\ H_z &= \frac{-j}{\omega\mu\varepsilon}\left(\frac{\partial^2}{\partial z^2} + \beta^2\right)F_z \end{aligned} \tag{A.5}$$

If F_z is separable, it can be written as

$$F_z(x,y,z) = f(x)g(y)h(z) \tag{A.6}$$

To simplify the problem and to consider the solutions that are important to the analysis in this case, we apply the theory of superposition and consider only the odd modes. Even modes may be considered separately and added to the solution.

For the potential function inside the dielectric, we consider the fact that there will be a standing wave between the air/dielectric boundary at $x = +a/2$ and $x = -a/2$, and apply the function for traveling waves in the z direction. We can then form the following potential function for odd modes inside the dielectric, where odd modes refer to the sine term in the potential function,

$$F_{zd}(x,y,z) = A_d \sin(\beta_{xd}x)e^{-j\beta_z z} \tag{A.7}$$

where

F_{zd} is the potential function inside the dielectric

A_d is the magnitude constant inside the dielectric

β_{xd} is the propagation constant in the x direction inside the dielectric

β_z is the propagation constant in the z direction inside and outside the dielectric

Outside the dielectric, we form similar functions, however, since the air around the dielectric slab is infinite, the wave is evanescent.

For $x > a/2$,

$$F_{zo+}(x,y,z) = A_o e^{-\alpha_{xo}x} e^{-j\beta_z z} \tag{A.8}$$

For $x < -a/2$,

$$F_{zo-}(x,y,z) = -A_o e^{+\alpha_{xo}x} e^{-j\beta_z z} \tag{A.9}$$

Where

F_{zo+} is the potential function outside the dielectric where $x > a/2$

F_{zo-} is the potential function outside the dielectric where $x < -a/2$

A_o is the magnitude constant outside the dielectric

α_{xo} is the attenuation constant in the x direction outside the dielectric

β_z is the propagation constant in the z direction inside and outside the dielectric

We may find the separation of variables equation by taking the second partial derivatives of each component of the potential function with the procedure outlined in [10].

Inside the dielectric,

$$\boxed{\beta_{xd}^{\ 2} + \beta_z^{\ 2} = \beta_d^{\ 2} = \omega^2 \varepsilon_d \mu_d} \tag{A.10}$$

where

β_d is the propagation constant inside the dielectric

Outside the dielectric,

$$\boxed{-\alpha_{xo}^{\ 2} + \beta_z^{\ 2} = \beta_o^{\ 2} = \omega^2 \varepsilon_o \mu_o} \tag{A.11}$$

where

β_o is the propagation constant outside the dielectric

Note that β_z is common to both inside and outside the dielectric. This allows us to solve for the entire wave at once, propagating as a whole. The propagation constant in the x direction uses the symbol α since when this quantity is zero, the wave is contained

entirely inside the dielectric with zero loss. Since we now have the necessary potential functions, we may apply our derivatives to find the electric and magnetic fields.

The fields for the odd modes inside the dielectric are then,

$$E_x = 0$$
$$E_y = \frac{1}{\varepsilon_d} A_d \beta_{xd} \cos(\beta_{xd} x) e^{-j\beta_z z} \tag{A.12}$$
$$E_z = 0$$

$$H_x = \frac{A_d \beta_{xd} \beta_z}{\omega \mu_d \varepsilon_d} \cos(\beta_{xd} x) e^{-j\beta_z z}$$
$$H_y = 0 \tag{A.13}$$
$$H_z = \frac{-jA_d}{\omega \mu_d \varepsilon_d} \left(\beta_d{}^2 - \beta_z{}^2\right) \sin(\beta_{xd} x) e^{-j\beta_z z}$$

The fields for the odd modes outside the dielectric, for $x > a/2$ are,

$$E_x = 0$$
$$E_y = -\frac{A_o \alpha_{xo}}{\varepsilon_o} e^{-\alpha_{xo} x} e^{-j\beta_z z} \tag{A.14}$$
$$E_z = 0$$

$$H_x = \frac{A_o \alpha_{xo} \beta_z}{\omega \mu_o \varepsilon_o} e^{-\alpha_{xo} x} e^{-j\beta_z z}$$
$$H_y = 0 \tag{A.15}$$
$$H_z = \frac{-jA_o}{\omega \mu_o \varepsilon_o} \left(\beta_o{}^2 - \beta_z{}^2\right) e^{-\alpha_{xo} x} e^{-j\beta_z z}$$

The fields for the odd modes outside the dielectric for $x < -a/2$ can be found in a similar fashion. Even modes can also be found through a similar procedure. We now apply boundary conditions at the dielectric / air boundary, ensuring that the normal and tangential field components are continuous.

To ensure continuity of the E_y component at $x = a/2$,

$$\frac{1}{\varepsilon_d} A_d \beta_{xd} \cos(\beta_{xd} a/2) e^{-j\beta_z z} = -\frac{1}{\varepsilon_o} A_o \alpha_{xo} e^{-\alpha_{xo} a/2} e^{-j\beta_z z} \tag{A.16}$$

To ensure continuity of the H_z component at $x = a/2$,

$$\frac{-jA_d}{\omega\mu_d\varepsilon_d}\left(\beta_d{}^2-\beta_z{}^2\right)\sin(\beta_{xd}\,a/2)e^{-j\beta_z z}=\frac{-jA_o}{\omega\mu_o\varepsilon_o}\left(\beta_o{}^2-\beta_z{}^2\right)e^{-\alpha_{xo}a/2}e^{-j\beta_z z} \tag{A.17}$$

Now, simplify and divide the second equation (A.18) by the first (A.17) to obtain,

$$\begin{aligned}\frac{\frac{A_d}{\mu_d\varepsilon_d}\left(\beta_d{}^2-\beta_z{}^2\right)\sin(\beta_{xd}\,a/2)}{\frac{1}{\varepsilon_d}A_d\beta_{xd}\cos(\beta_{xd}\,a/2)}&=\frac{\frac{A_o}{\mu_o\varepsilon_o}\left(\beta_o{}^2-\beta_z{}^2\right)e^{-\alpha_{xo}a/2}}{-\frac{1}{\varepsilon_o}A_o\alpha_{xo}e^{-\alpha_{xo}a/2}}\\ \frac{\left(\beta_d{}^2-\beta_z{}^2\right)\tan(\beta_{xd}\,a/2)}{\mu_d\beta_{xd}}&=-\frac{\left(\beta_o{}^2-\beta_z{}^2\right)}{\mu_o\alpha_{xo}}\end{aligned} \tag{A.18}$$

We may simplify this equation by re-arranging the separation of variables equation,

$$\begin{aligned}\beta_{xd}{}^2&=\beta_d{}^2-\beta_z{}^2\\ -\alpha_{xo}{}^2&=\beta_o{}^2-\beta_z{}^2\end{aligned} \tag{A.19}$$

We may then substitute and obtain

$$\begin{aligned}\frac{\beta_{xd}{}^2\tan(\beta_{xd}\,a/2)}{\mu_d\beta_{xd}}&=\frac{\alpha_{xo}{}^2}{\mu_o\alpha_{xo}}\\ \beta_{xd}\tan(\beta_{xd}\,a/2)&=\frac{\mu_d\alpha_{xo}}{\mu_o}\end{aligned} \tag{A.20}$$

$$\boxed{\frac{\beta_{xd}a}{2}\tan(\beta_{xd}\,a/2)=\frac{\mu_d}{\mu_o}\frac{\alpha_{xo}a}{2}} \tag{A.21}$$

This last equation may be used to find the TE cutoff modes for the infinitely large dielectric slab waveguide as follows,

The propagation constant of the wave itself must lie between that of each medium [10], or

$$\beta_o<\beta_z<\beta_d \tag{A.22}$$

It is intuitive to see that this should be the case, however, the reader may refer to [9] or [10] for a more detailed explanation of this. The lowest propagation constant allowed for the wave is when it approaches the lower end of the bound, or β_o. If this is the case, then from the separation of variables equation,

$$\alpha_{xo}{}^2=\beta_z{}^2-\beta_o{}^2\approx 0 \tag{A.23}$$

This implies that the zeros of the equation for the cutoff modes may be written as

$$\frac{\beta_{xd}a}{2}\tan(\beta_{xd}\,a/2) = \frac{\mu_d}{\mu_o}\frac{\alpha_{xo}a}{2} = 0$$
$$\beta_{xd}\,a/2 = \frac{n\pi}{2} \tag{A.24}$$

where n is an integer. At cutoff, we may again make an approximation as follows,

$$\begin{aligned}
&\beta_{xd}^{\,2} + \beta_z^{\,2} = \beta_d^{\,2} = \omega^2\varepsilon_d\mu_d \\
&when\ \ \beta_z^{\,2} \to \beta_o^{\,2} \\
&\beta_{xd}^{\,2} \approx \beta_d^{\,2} - \beta_o^{\,2} = \omega^2\varepsilon_d\mu_d - \omega^2\varepsilon_o\mu_o \\
&\beta_{xd} \approx \omega\sqrt{\varepsilon_d\mu_d - \varepsilon_o\mu_o}
\end{aligned} \tag{A.25}$$

Then, finally, we may substitute (A.25) into the (A.24) above to obtain the cutoff frequencies for odd modes [9] [10] [11] as,

$$\boxed{f_c = \frac{n}{2a\sqrt{\varepsilon_d\mu_d - \varepsilon_o\mu_o}}} \tag{A.26}$$

where for odd modes, n = 1, 3, 5, etc…

For even modes, n = 0, 2, 4, etc… where the entire derivation above is repeated [10]. TM modes are found the same way. We note that in (A.26), the cutoff modes for both the TE and TM modes begin at 0 Hz for TE_0 and TM_0. Again, as in the case for TIR, this equation provides real numbers only if dielectric constant ε_d is larger than dielectric constant ε_o.

Appendix B: The Single Mode H-guide

In this Appendix, the thin single mode H-guide and its cutoff frequencies are discussed as shown in Fig. B.1.

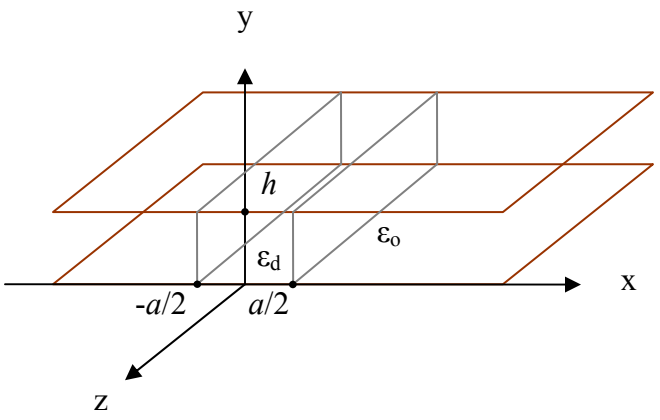

Fig. B.1 The H-guide. A rectangular dielectric slab extends from $x = -a/2$ to $x = a/2$ and is bounded at $y = 0$ and $y = h$ by metallic plates. The structure continues to infinity in the +z and –z directions.

Results in this thesis show that, surprisingly, low loss H-guide propagation is indeed possible for very small plate separations less than a half wavelength apart. This has been shown through simulated results with copper and dielectric losses in Chapter 3, and with measured results in Chapter 5. We therefore wish to study the TE_z propagation in a thin H-guide using a similar procedure as the previous section, where $E_z = 0$ and E_x and E_y may or may not be zero.

Consider in this case, that the electric fields tangent to the metallic plates are forced to zero. Therefore, at $y = 0$ and $y = h$,

$$E_x = E_y = 0 \tag{B.1}$$

We can assume a standing wave between the two metallic plates as for rectangular waveguides,

$$g(y) = C_1 \sin(\beta y) + C_2 \cos(\beta y) \tag{B.2}$$

Applying the same potential functions in the x and z directions from the previous section allows us to form F_z as follows,

For odd modes in the x direction inside the dielectric,

$$F_{zd}(x,y,z) = A_d \sin(\beta_{xd}x)\left[C_1 \sin(\beta_{yd}y) + C_2 \cos(\beta_{yd}y)\right] e^{-j\beta_z z} \tag{B.3}$$

For odd modes in the x direction outside the dielectric when $x > a/2$,

$$F_{zo+}(x,y,z) = A_d e^{-\alpha_{xo}x}\left[C_1 \sin(\beta_{yo}y) + C_2 \cos(\beta_{yo}y)\right] e^{-j\beta_z z} \tag{B.4}$$

Again, we have assumed the same propagation constant in the z direction so that we solve for the wave propagating as a whole and have assumed a standing wave in the y direction. To simplify the problem, we find the E_x derivative in the dielectric and apply boundary conditions as follows,

$$E_x = A_d \sin(\beta_{xd}x)\left[C_1\beta_{yd} \cos(\beta_{yd}y) - C_2\beta_{yd} \sin(\beta_{yd}y)\right] e^{-j\beta_z z} \tag{B.5}$$

At $y = 0$, $E_x = 0$, so that the only non-trivial solution requires that C_1 is zero. In addition, at $y = h$, $E_x = 0$, so that inside the dielectric,

$$\beta_{yd}h = n\pi \tag{B.6}$$

And outside the dielectric,

$$\beta_{yo}h = n\pi \tag{B.7}$$

In this case, we will assume the same mode in the y direction (parallel to the air/dielectric boundary), inside and outside the dielectric. The same technique is applied to the partially filled dielectric waveguide in [10] to satisfy the boundary conditions along the air/dielectric edge. Therefore,

$$\beta_y = \beta_{yd} = \beta_{yo} \tag{B.8}$$

Where

β_{yd} is the propagation constant in the y direction inside the dielectric

β_{yo} is the propagation constant in the y direction outside the dielectric

β_y is the propagation constant in the y direction both inside and outside the dielectric, since they are assumed to be the same.

We may then rewrite the potential functions as follows. For odd modes in the x direction inside the dielectric,

$$F_{zd}(x,y,z) = A_d \sin(\beta_{xd}x)\cos(\beta_y y)e^{-j\beta_z z} \tag{B.9}$$

For odd modes in the x direction outside the dielectric when $x > a/2$,

$$F_{zo+}(x,y,z) = A_o e^{-\alpha_{xo}x}\cos(\beta_y y)\, e^{-j\beta_z z} \tag{B.10}$$

For odd modes in the x direction outside the dielectric when $x < -a/2$,

$$F_{zo+}(x,y,z) = -A_o e^{+\alpha_{xo}x}\cos(\beta_y y)\, e^{-j\beta_z z} \tag{B.11}$$

Applying the same technique as in the previous section, we apply the separation of variables technique again to find, inside the dielectric,

$$\boxed{\beta_{xd}{}^2 + \beta_y{}^2 + \beta_z{}^2 = \beta_d{}^2 = \omega^2\varepsilon_d\mu_d} \tag{B.12}$$

And outside the dielectric,

$$\boxed{-\alpha_{xo}{}^2 + \beta_y{}^2 + \beta_z{}^2 = \beta_o{}^2 = \omega^2\varepsilon_o\mu_o} \tag{B.13}$$

We now find our fields by applying derivatives to the potential functions as follows. Inside the dielectric,

$$\begin{aligned}
E_x &= -\frac{A_d\beta_y}{\varepsilon_d}\sin(\beta_{xd}x)\sin(\beta_y y)e^{-j\beta_z z} \\
E_y &= \frac{A_d\beta_{xd}}{\varepsilon_d}\cos(\beta_{xd}x)\cos(\beta_y y)e^{-j\beta_z z} \\
E_z &= 0
\end{aligned} \tag{B.14}$$

$$\begin{aligned}
H_x &= \frac{A_d\beta_{xd}\beta_z}{\omega\mu_d\varepsilon_d}\cos(\beta_{xd}x)\cos(\beta_y y)e^{-j\beta_z z} \\
H_y &= -\frac{A_d\beta_y\beta_z}{\omega\mu_d\varepsilon_d}\sin(\beta_{xd}x)\sin(\beta_y y)e^{-j\beta_z z} \\
H_z &= \frac{-jA_d}{\omega\mu_d\varepsilon_d}\left(\beta_d{}^2 - \beta_z{}^2\right)\sin(\beta_{xd}x)\cos(\beta_y y)e^{-j\beta_z z}
\end{aligned} \tag{B.15}$$

Outside the dielectric, we have

$$
\begin{aligned}
E_x &= \frac{A_o \beta_y}{\varepsilon_o} e^{-\alpha_{xo} x} \sin(\beta_y y) e^{-j\beta_z z} \\
E_y &= -\frac{A_o \alpha_{xo}}{\varepsilon_o} e^{-\alpha_{xo} x} \cos(\beta_y y) e^{-j\beta_z z} \\
E_z &= 0
\end{aligned}
\tag{B.16}
$$

$$
\begin{aligned}
H_x &= -\frac{A_o \alpha_{xo} \beta_z}{\omega \mu_o \varepsilon_o} e^{-\alpha_{xo} x} \cos(\beta_y y) e^{-j\beta_z z} \\
H_y &= -\frac{A_o \beta_y \beta_z}{\omega \mu_o \varepsilon_o} e^{-\alpha_{xo} x} \sin(\beta_y y) e^{-j\beta_z z} \\
H_z &= \frac{-jA_o}{\omega \mu_o \varepsilon_o} \left(\beta_o^{\,2} - \beta_z^{\,2}\right) e^{-\alpha_{xo} x} \cos(\beta_y y) e^{-j\beta_z z}
\end{aligned}
\tag{B.17}
$$

We may now apply additional boundary conditions to our problem. We previously applied boundary conditions with the y potential function at $y = 0$ and $y = h$ to simplify our problem, where we have found that

$$\beta_y h = n\pi \tag{B.18}$$

We can apply boundary conditions at $x = a/2$ for the E_y component as follows,

$$\frac{A_d \beta_{xd}}{\varepsilon_d} \cos(\beta_{xd} a/2) \cos(\beta_y y) e^{-j\beta_z z} = -\frac{A_o \alpha_{xo}}{\varepsilon_o} e^{-\alpha_{xo} a/2} \cos(\beta_y y) e^{-j\beta_z z} \tag{B.19}$$

We can apply boundary conditions at $x = a/2$ for the H_z component as follows,

$$\frac{-jA_d}{\omega \mu_d \varepsilon_d} \left(\beta_d^{\,2} - \beta_z^{\,2}\right) \sin(\beta_{xd} a/2) \cos(\beta_y y) e^{-j\beta_z z} = \frac{-jA_o}{\omega \mu_o \varepsilon_o} \left(\beta_o^{\,2} - \beta_z^{\,2}\right) e^{-\alpha_{xo} a/2} \cos(\beta_y y) e^{-j\beta_z z} \tag{B.20}$$

We simplify and divide these equations to find

$$
\begin{aligned}
\frac{\frac{A_d}{A_o} \left(\beta_d^{\,2} - \beta_z^{\,2}\right)}{\frac{A_d \beta_{xd}}{A_o}} \sin(\beta_{xd} a/2) &= \frac{\frac{\mu_d \varepsilon_d}{\mu_o \varepsilon_o} e^{-\alpha_{xo} a/2}}{-\frac{\varepsilon_d \alpha_{xo}}{\varepsilon_o} e^{-\alpha_{xo} a/2}} \\
\frac{\alpha_{xo} \left(\beta_d^{\,2} - \beta_z^{\,2}\right)}{\left(\beta_o^{\,2} - \beta_z^{\,2}\right)} \tan(\beta_{xd} a/2) &= -\frac{\mu_d}{\mu_o} \beta_{xd}
\end{aligned}
\tag{B.21}
$$

which is identical to the case without infinite metallic plates. In this case, however, the separation of variables equations have an additional $\beta_y^{\,2}$ term, which will lead to different cutoff frequencies for modes higher than TE_{m0} in the y direction where $\beta_y \neq 0$. Cutoff frequencies for the TE_{m0} modes, for example, are identical for the TE_m modes in an

infinite dielectric slab with or without parallel metallic plates since $\beta_y = 0$, while cutoff frequencies for TE_{m1} will be different than for TE_{m0} modes since $\beta_y \neq 0$. It is possible to solve for the cutoff frequencies for modes higher than TE_{m0} using the separation of variables equations and applying additional boundary condition equations, however, we may simplify the problem for our purposes as follows. Consider the separation of variables equation, repeated here for convenience,

$$\beta_{xd}^{\ 2} + \beta_y^{\ 2} + \beta_z^{\ 2} = \beta_d^{\ 2} \tag{B.22}$$

Using Pythagoras' theorem, we see than β_y must be smaller than β_d if β_z does not equal zero. To satisfy boundary conditions in the y direction, we must satisfy

$$\beta_y h = n\pi \tag{B.23}$$

Let us substitute β_y for β_d to find a lower bound on the lowest frequency that satisfies the boundary condition for mode $n = 1$.

$$\beta_d h > \pi$$
$$f_c > \frac{1}{2h\sqrt{\mu_d \varepsilon_d}} \tag{B.24}$$

For Roger`s Duroid 5880 substrate where $\varepsilon_r = 2.2$ and the height, h, of the substrate is 1.575 mm we obtain from (B.25),

$$f_c > 64.17\ GHz \tag{B.25}$$

We can see that the first cutoff frequency is quite high in the y direction. This will be a function of the dielectric constant and the height of the substrate chosen. Now, consider the cutoff frequency for the TE_1 mode for the infinite dielectric slab without metallic plates, which will be the same as for the TE_{10} mode for the infinite dielectric slab with metallic plates, where $n = 1$. Let's use (A.26) repeated here for convenience,

$$f_c = \frac{n}{2a\sqrt{\varepsilon_d \mu_d - \varepsilon_o \mu_o}} \tag{B.26}$$

For the same Roger's Duroid 5880 substrate as used in Eq. (B.25), where $\varepsilon_r = 2.2$ and the height, h, of the substrate is 1.575 mm and $a = 6.0$ mm, we obtain

$$f_c = 22.8\ GHz \tag{B.27}$$

We can see that for this realizable case, the cutoff frequency for the TE_{10} modes is much lower than the lowest possible cutoff frequencies for the TE modes restricted by the

height of the substrate. In addition, since these frequencies are both above 20 GHz, there is a very large bandwidth available between 6 and 20 GHz that is available. Note that these zero order modes may propagate. At lower frequencies, however, waves in the x-direction extend great distances from the waveguide [10], causing unwanted losses.

Another approach to finding the cutoff frequency for modes where the electric field is parallel to the metallic plates involves solving for TM modes in an infinite dielectric slab, as discussed in [40] for the Non-Radiative Dielectric (NRD) waveguide. If the guide wavelength, λ_g, for the TM_1 mode is found according to equations in [11] or [40], then the distance $\lambda_g / 2$ represents the lower bound on the distance between metallic plates where propagation may occur. For the case discussed above for Eq. (B.27), this method for finding the TM_1 mode produces a frequency of 65.98 GHz, or less than 3.5% away from the lower bound found using Eq. (B.24). This method, however, requires solving a much more complicated system of equations as discussed in [11] and [40].

Appendix C: Rectangular Dielectric Waveguide

In this section, the rectangular dielectric waveguide is discussed, where a rectangular piece of dielectric waveguide guides electromagnetic waves in the +z direction.

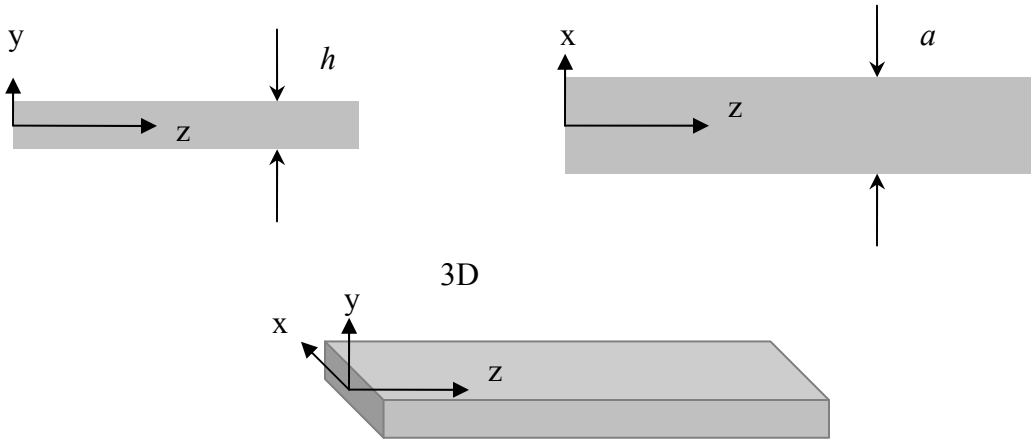

Fig. C.1 Rectangular dielectric waveguide.

We wish to study the quasi TE_z propagation in the rectangular waveguide using a similar procedure as a dielectric slab waveguide in [10], where $E_z = 0$ and E_x and E_y may or may not be zero, while using the same approach as in [65].

Assume that the electric field potential components are separable, and can be written in the form

$$F(x,y,z) = f(x)g(y)h(z) \tag{C.1}$$

The potentials inside the dielectric are chosen to yield a symmetric E_y electric field for TE_z modes. The fields in Regions 1 through 5 are considered, where regions in the corners are ignored, as shown in Fig. C.2 and proposed in the model in [65].

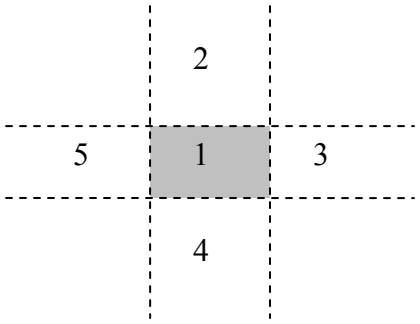

Fig. C.2 Regions for consideration in [65], labeled 1 through 5. Non-labelled regions are not considered.

Inside the dielectric,

$$F_{zd}(x,y,z) = C_{xd}C_{yd}C_z \sin(\beta_{xd}x)\cos(\beta_{yd}y)\, e^{-j\beta_z z} \tag{C.2}$$

The potentials outside the dielectric are chosen to decay exponentially, and to match the boundary conditions at the air/dielectric boundary as in the model in [65]. The distribution along the x direction outside the dielectric is the same as inside the dielectric, for example.

Outside the dielectric on top, ($y > h/2$)

$$F_{zo}(x,y,z) = C_{xd}C_{yo}C_z \sin(\beta_{xd}x)\, e^{-\beta_{yo}y} e^{-j\beta_z z} \tag{C.3}$$

Outside the dielectric on the right, ($x > a/2$)

$$F_{zo}(x,y,z) = C_{xo}C_{yd}C_z e^{-\beta_{xo}x} \cos(\beta_{yd}y)\, e^{-j\beta_z z} \tag{C.4}$$

The same propagation constant is used in the z direction for inside the dielectric as outside the dielectric so that the wave propagates as a whole. In the air section, the same distribution is assumed immediately next to the structure.

Using potential F_z, and assuming TE_z modes, the electromagnetic fields are found with the following derivatives. [10]

$$E_x = -\frac{1}{\varepsilon}\frac{\partial F_z}{\partial y}$$
$$E_y = \frac{1}{\varepsilon}\frac{\partial F_z}{\partial x} \tag{C.5}$$
$$E_z = 0$$

$$H_x = -j\frac{1}{\omega\mu\varepsilon}\frac{\partial^2 F_z}{\partial x \partial z}$$
$$H_y = -j\frac{1}{\omega\mu\varepsilon}\frac{\partial^2 F_z}{\partial y \partial z} \tag{C.6}$$
$$H_z = -j\frac{1}{\omega\mu\varepsilon}\left(\frac{\partial^2}{\partial z^2} + \beta^2\right)F_z$$

Inside the dielectric,

$$E_x = \frac{A_d \beta_{yd}}{\varepsilon_d}\sin(\beta_{xd}x)\sin(\beta_{yd}y)e^{-j\beta_z z}$$
$$E_y = \frac{A_d \beta_{xd}}{\varepsilon_d}\cos(\beta_{xd}x)\cos(\beta_{yd}y)e^{-j\beta_z z} \tag{C.7}$$
$$E_z = 0$$

$$H_x = -\frac{A_d \beta_{xd}\beta_z}{\omega\mu_d\varepsilon_d}\cos(\beta_{xd}x)\cos(\beta_{yd}y)e^{-j\beta_z z}$$
$$H_y = \frac{A_d \beta_{yd}\beta_z}{\omega\mu_d\varepsilon_d}\sin(\beta_{xd}x)\sin(\beta_{yd}y)e^{-j\beta_z z} \tag{C.8}$$
$$H_z = \frac{-jA_d}{\omega\mu_d\varepsilon_d}\left(\beta_d{}^2 - \beta_z{}^2\right)\sin(\beta_{xd}x)\cos(\beta_{yd}y)e^{-j\beta_z z}$$

Outside the dielectric on top,

$$E_x = \frac{A_o \beta_{yo}}{\varepsilon_o}\sin(\beta_{xd}x)e^{-\beta_{yo}y}e^{-j\beta_z z}$$
$$E_y = \frac{A_o \beta_{xd}}{\varepsilon_o}\cos(\beta_{xd}x)e^{-\beta_{yo}y}e^{-j\beta_z z} \tag{C.9}$$
$$E_z = 0$$

$$H_x = -\frac{A_o \beta_{xd} \beta_z}{\omega \mu_o \varepsilon_o} \cos(\beta_{xd} x) e^{-\beta_{yo} x} e^{-j\beta_z z}$$
$$H_y = \frac{A_o \beta_{yo} \beta_z}{\omega \mu_o \varepsilon_o} \sin(\beta_{xd} x) e^{-\beta_{yo} y} e^{-j\beta_z z} \quad \text{(C.10)}$$
$$H_z = \frac{-jA_o}{\omega \mu_o \varepsilon_o} \left(\beta_o{}^2 - \beta_z{}^2\right) \sin(\beta_{xd} x) e^{-\beta_{yo} y} e^{-j\beta_z z}$$

Outside the dielectric on the right,

$$E_x = \frac{A_o \beta_{yd}}{\varepsilon_o} e^{-\beta_{xo} x} \sin(\beta_{yd} y) e^{-j\beta_z z}$$
$$E_y = -\frac{A_o \beta_{xo}}{\varepsilon_o} e^{-\beta_{xo} x} \cos(\beta_{yd} y) e^{-j\beta_z z} \quad \text{(C.11)}$$
$$E_z = 0$$

$$H_x = \frac{A_o \beta_{xo} \beta_z}{\omega \mu_o \varepsilon_o} e^{-\beta_{xo} x} \cos(\beta_{yd} y) e^{-j\beta_z z}$$
$$H_y = \frac{A_o \beta_{yd} \beta_z}{\omega \mu_o \varepsilon_o} e^{-\beta_{xo} x} \sin(\beta_{yd} y) e^{-j\beta_z z} \quad \text{(C.12)}$$
$$H_z = \frac{-jA_o}{\omega \mu_o \varepsilon_o} \left(\beta_o{}^2 - \beta_z{}^2\right) e^{-\beta_{xo} x} \cos(\beta_{yd} y) e^{-j\beta_z z}$$

The separation of variables equation is used to find the characteristic equations inside and outside the dielectric.

$$\frac{1}{f}\frac{d^2 f}{dx^2} + \frac{1}{g}\frac{d^2 g}{dy^2} + \frac{1}{h}\frac{d^2 h}{dz^2} = -\beta^2 \quad \text{(C.14)}$$

Inside the dielectric,

$$\beta_{xd}{}^2 + \beta_{yd}{}^2 + \beta_z{}^2 = \beta_d{}^2 = \omega^2 \varepsilon_d \mu_d$$
$$\beta_{xd}{}^2 + \beta_{yd}{}^2 = \beta_d{}^2 - \beta_z{}^2 \quad \text{(C.15)}$$

And outside the dielectric,

$$-\beta_{xo}{}^2 - \beta_{yo}{}^2 + \beta_z{}^2 = \beta_o{}^2 = \omega^2 \varepsilon_o \mu_o$$
$$\beta_{xo}{}^2 + \beta_{yo}{}^2 = \beta_z{}^2 - \beta_o{}^2 \quad \text{(C.16)}$$

The negative terms appear when substituting the functions *f* and *g* outside the dielectric into the separation of variables equation.

Now, apply boundary conditions along the entire right edge, where E_y must be continous

$$E_y = \frac{A_d \beta_{xd}}{\varepsilon_d}\cos(\beta_{xd}x)\cos(\beta_{yd}y)e^{-j\beta_z z} = -\frac{A_o \beta_{xo}}{\varepsilon_o}e^{-\beta_{xo}x}\cos(\beta_{yd}y)e^{-j\beta_z z}$$
$$\frac{A_d \beta_{xd}}{\varepsilon_d}\cos(\beta_{xd}\frac{a}{2}) = -\frac{A_o \beta_{xo}}{\varepsilon_o}e^{-\beta_{xo}\frac{a}{2}} \tag{C.17}$$

Along the entire right edge, H_z must also be continous

$$H_z = \frac{-jA_d}{\omega\mu_d\varepsilon_d}\left(\beta_d{}^2 - \beta_z{}^2\right)\sin(\beta_{xd}x)\cos(\beta_{yd}y)e^{-j\beta_z z} = \frac{-jA_o}{\omega\mu_o\varepsilon_o}\left(\beta_o{}^2 - \beta_z{}^2\right)e^{-\beta_{xo}x}\cos(\beta_{yd}y)e^{-j\beta_z z}$$
$$\frac{A_d}{\mu_d\varepsilon_d}\left(\beta_d{}^2 - \beta_z{}^2\right)\sin(\beta_{xd}\frac{a}{2}) = \frac{A_o}{\mu_o\varepsilon_o}\left(\beta_o{}^2 - \beta_z{}^2\right)e^{-\beta_{xo}\frac{a}{2}} \tag{C.18}$$

Divide, (C.17) and (C.18)

$$\frac{\frac{A_d \beta_{xd}}{\varepsilon_d}\cos(\beta_{xd}\frac{a}{2})}{\frac{A_d}{\mu_d\varepsilon_d}\left(\beta_d{}^2 - \beta_z{}^2\right)\sin(\beta_{xd}\frac{a}{2})} = \frac{-\frac{A_o \beta_{xo}}{\varepsilon_o}e^{-\beta_{xo}\frac{a}{2}}}{\frac{A_o}{\mu_o\varepsilon_o}\left(\beta_o{}^2 - \beta_z{}^2\right)e^{-\beta_{xo}\frac{a}{2}}}$$
$$\beta_{xd}\cot(\beta_{xd}\frac{a}{2}) = -\beta_{xo}\frac{\mu_o}{\mu_d}\frac{\left(\beta_d{}^2 - \beta_z{}^2\right)}{\left(\beta_o{}^2 - \beta_z{}^2\right)} \tag{C.19}$$

Apply boundary conditions along the entire top edge, where the E_x term must be continuous.

$$E_x = \frac{A_d \beta_{yd}}{\varepsilon_d}\sin(\beta_{xd}x)\sin(\beta_{yd}y)e^{-j\beta_z z} = \frac{A_o \beta_{yo}}{\varepsilon_o}\sin(\beta_{xd}x)e^{-\beta_{yo}y}e^{-j\beta_z z}$$
$$\frac{A_d \beta_{yd}}{\varepsilon_d}\sin(\beta_{yd}\frac{h}{2}) = \frac{A_o \beta_{yo}}{\varepsilon_o}e^{-\beta_{yo}\frac{h}{2}} \tag{C.20}$$

Along the entire top edge, H_z must be continuous,

$$H_z = \frac{-jA_d}{\omega\mu_d\varepsilon_d}\left(\beta_d{}^2 - \beta_z{}^2\right)\sin(\beta_{xd}x)\cos(\beta_{yd}y)e^{-j\beta_z z} = \frac{-jA_o}{\omega\mu_o\varepsilon_o}\left(\beta_o{}^2 - \beta_z{}^2\right)\sin(\beta_{xd}x)\,e^{-\beta_{yo}y}e^{-j\beta_z z}$$

$$\frac{A_d}{\mu_d\varepsilon_d}\left(\beta_d{}^2 - \beta_z{}^2\right)\cos(\beta_{yd}\frac{h}{2}) = \frac{A_o}{\mu_o\varepsilon_o}\left(\beta_o{}^2 - \beta_z{}^2\right)e^{-\beta_{yo}\frac{h}{2}} \tag{C.21}$$

Divide (C.20) and (C.21) to obtain

$$\frac{\frac{A_d\beta_{yd}}{\varepsilon_d}\sin(\beta_{yd}\frac{h}{2})}{\frac{A_d}{\mu_d\varepsilon_d}\left(\beta_d{}^2 - \beta_z{}^2\right)\cos(\beta_{yd}\frac{h}{2})} = \frac{\frac{A_o\beta_{yo}}{\varepsilon_o}e^{-\beta_{yo}\frac{h}{2}}}{\frac{A_o}{\mu_o\varepsilon_o}\left(\beta_o{}^2 - \beta_z{}^2\right)e^{-\beta_{yo}\frac{h}{2}}} \tag{C.22}$$

$$\beta_{yd}\tan(\beta_{yd}\frac{h}{2}) = \beta_{yo}\frac{\mu_o}{\mu_d}\frac{\left(\beta_d{}^2 - \beta_z{}^2\right)}{\left(\beta_o{}^2 - \beta_z{}^2\right)}$$

Along the entire top edge, E_y must be discontinuous by $\varepsilon_d E_d = \varepsilon_o E_o$

$$E_y = \varepsilon_d\frac{A_d\beta_{xd}}{\varepsilon_d}\cos(\beta_{xd}x)\cos(\beta_{yd}y)e^{-j\beta_z z} = \varepsilon_o\frac{A_o\beta_{xd}}{\varepsilon_o}\cos(\beta_{xd}x)e^{-\beta_{yo}y}e^{-j\beta_z z} \tag{C.23}$$

$$A_d\cos(\beta_{yd}\frac{h}{2}) = A_o e^{-\beta_{yo}\frac{h}{2}}$$

Divide by the H_z (C.21) condition on the top edge, to obtain,

$$\frac{\left(\beta_d{}^2 - \beta_z{}^2\right)}{\left(\beta_o{}^2 - \beta_z{}^2\right)} = \frac{\mu_d\varepsilon_d}{\mu_o\varepsilon_o} \tag{C.24}$$

However, (C.24) suggests that we may solve β_z as follows,

$$\begin{aligned}
&\mu_o\varepsilon_o\left(\beta_d{}^2 - \beta_z{}^2\right) = \mu_d\varepsilon_d\left(\beta_o{}^2 - \beta_z{}^2\right)\\
&\mu_o\varepsilon_o\beta_d{}^2 - \mu_o\varepsilon_o\beta_z{}^2 = \mu_d\varepsilon_d\beta_o{}^2 - \mu_d\varepsilon_d\beta_z{}^2\\
&\beta_z{}^2\left(\mu_d\varepsilon_d - \mu_o\varepsilon_o\right) = \mu_d\varepsilon_d\beta_o{}^2 - \mu_o\varepsilon_o\beta_d{}^2\\
&\beta_z{}^2 = \frac{\mu_d\varepsilon_d\beta_o{}^2 - \mu_o\varepsilon_o\beta_d{}^2}{\left(\mu_d\varepsilon_d - \mu_o\varepsilon_o\right)} = \frac{\mu_d\varepsilon_d\omega^2\mu_o\varepsilon_o - \mu_o\varepsilon_o\omega^2\mu_d\varepsilon_d}{\left(\mu_d\varepsilon_d - \mu_o\varepsilon_o\right)} = 0
\end{aligned} \tag{C.25}$$

(C.25) suggests a non-causal answer for β_z!

Sub into (C.15) and (C.16),

$$\frac{\beta_{xo}{}^2 + \beta_{yo}{}^2}{\beta_{xd}{}^2 + \beta_{yd}{}^2} = -\frac{\mu_o\varepsilon_o}{\mu_d\varepsilon_d} \tag{C.26}$$

Sub (C.24) into (C.19) and (C.22), to obtain

$$\beta_{xd} \cot(\beta_{xd} \frac{a}{2}) = -\beta_{xo} \frac{\varepsilon_d}{\varepsilon_o} \tag{C.27}$$

$$\beta_{yd} \tan(\beta_{yd} \frac{h}{2}) = \beta_{yo} \frac{\varepsilon_d}{\varepsilon_o} \tag{C.28}$$

Equations (C.27) and (C.28) are the same equations as presented for the infinite dielectric slab case in [10], and for the rectangular dielectric waveguide in [65]. Note that we applied equation (C.24), which implies that propagation is non-causal as shown in Equation (C.25).

In [65], the author explains that the rectangular dielectric waveguide can be represented by two intersecting infinite dielectric slabs using formulas (C.27) and (C.28). In [69], the procedure is outlined, where TM modes are assumed in one plane and TE modes in the other. The dielectric slab can then be solved easily using techniques in [10].

Another model for the rectangular dielectric waveguide uses Bessel functions [68], however more recent work [69] claims that parts of this work is incorrect. [69] also suggest that the model for two intersecting dielectric slabs [65] is the easiest, most effective way to obtain an estimate for the propagation constant of the rectangular dielectric waveguide, despite its non-physical properties.

Appendix D: Qualitative Transmission Line Comparison

A detailed comparison between different types of transmission lines, is included in publications such as [1] or [56], where the H-guide is discussed. Copper and dielectric losses for the H-guide are considered in [56] on p. 331. For the frequencies and structures discussed in this thesis made of low-loss Rogers substrates, dielectric and conductor losses are negligible.

Here, a qualitative comparison is summarized in tabulated form for convenience.

Transmission line	Advantage	Disadvantage
Microstrip	• Compact. • Wideband. • Robust. • Easy to manufacture using chemical etching or mechanical milling.	• Leaky for high frequency antenna designs especially around bends. • Chemical etching may sometimes not be easy or environmentally friendly.
Standard Air-filled metallic waveguide	• Able to carry vast amounts of power. (hundreds of watts) • Low loss.	• Large. • Heavy. • Costly to manufacture quality, low-loss components.
Single mode H-guide	• Low loss when operating in the proper mode in the proper frequency range. • Can be made very thin. • Highly suitable for	• Leaky around bends and discontinuities • Width approximately double that of a metallic waveguide. • Proposed transition in this

	• Can be fabricated cost effectively with a low cost mechanical milling process.	
Substrate Integrated Waveguide [70]	• Compact. • Little leakage around bends or discontinuities.	• Prone to metallic losses, especially at high frequencies. • Prone to manufacturing defects. i.e. one bad via may seriously affect performance. • Expensive equipment needed for clean, fast, reliable mm wave fabrication. • Fabrication is time consuming without costly equipment.

Appendix E: HFSS Simulations

HFSS [36] is a popular commercial simulation software based on the Finite Element Method (FEM). Structures can be drawn in a three-dimensional Computer Aided Design (CAD) environment.

Once drawn in this CAD environment, HFSS is able to "mesh" the structure. In HFSS, meshing a structure consists of dividing it into very small three dimensional tetrahedral shapes that approximate the actual structure. The density of these shapes depend on the dielectric constant, proximity to metallic surfaces, proximity to sources, or proximity to boundary conditions, etc…

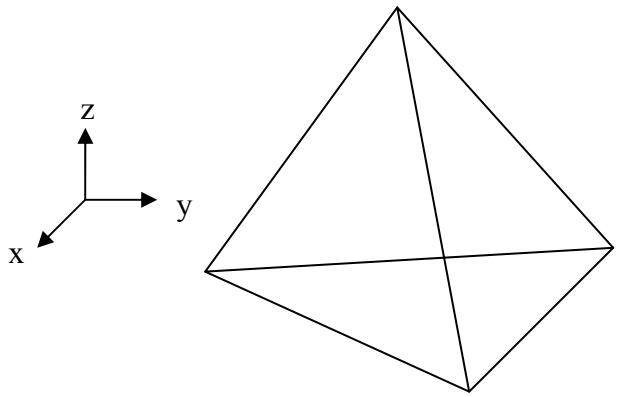

Fig. E.1 A single tetrahedral shape used for meshing a structure in HFSS.

Once the structure has been meshed, an electric field that satisfies Maxwell's equations is solved using matrix methods. The value of the electric field is stored at the vertices of each tetrahedron and at the midpoints of each edge. Values of the electric field at interior points are found through interpolation.

A tradeoff exists between the size of the mesh and accuracy. Of course, a very fine mesh will yield higher accuracy; however, will also result in a very long computational time. HFSS begins with a very coarse mesh, then will refine the mesh until the required

accuracy is found in regions of high error, such as near a waveport or metallic edges. The user may choose the level of accuracy of the final solution.

The HFSS package contains automated tools to optimize a design, which can save valuable user time. Available resources include parametric analysis of structure dimensions, or optimization analysis using non-linear techniques. In both of these methods, the structure's dimensions are varied to obtain a certain simulation result, such as a greater return loss (S11), or smaller insertion losses (S21). Other goals can include higher antenna gains, or almost any other parameter available in HFSS.

For a parametric analysis, the user begins by defining a nominal geometry. The user then defines which variables should be changed at each step. HFSS allows the user to choose a linear step of a certain dimension, such as varying the length of a structure from 10 mm to 15 mm in 1 mm steps.

For an optimization analysis, the non-linear method works best if the user begins by defining a near-optimal geometry. The user then must define which variables are part of the study, and in addition, must define the goal and limits for the simulation. One example would be to vary the length of a dipole antenna to obtain a best return loss at 2 GHz. The user may then choose the optimization method, such as Pattern Search, Sequential Non-Linear Programming, Quasi Newton, etc… The solutions in this thesis have used the Sequential Non-Linear Programming method.

Appendix F: Examples

In this appendix, some examples are discussed that aid in the understanding of the structures and theories discussed in this thesis.

Example 1: Single Mode H-guide

You are given a surplus of 62 mil thick Rogers 5880. Design a single mode H-guide with for operation from 8 to 13.7 GHz.

Step 1: Convert 62 mils to millimeters

25.2 mm is equal to 1 inch, which is equal to 1000 mils, or thousands of an inch.

$$\frac{62\,mils}{1000\,mils/inch}\times 25.2\,mm/inch = 1.575\,mm$$

Step 2: Find a lower bound for the cutoff frequency for modes where the electric field is parallel to the metallic plates.

Using equations in Appendix B (B.24),

$$\beta_d h > \pi$$

$$f_c > \frac{1}{2h\sqrt{\mu_d \varepsilon_d}}$$

And using a height of 1.575, and a dielectric constant of 2.2,

$$f_c > 64.17\ GHz$$

Therefore, below 64.17 GHz, for non-lossy modes, the electric fields will be perpendicular to the metallic plates. These modes are denoted TE_{n0}, where n is an integer.

Step 3: Find the cutoff frequency of the first mode.

Using equation (2.2),

$$f_c = \frac{n}{2a\sqrt{\varepsilon_d \mu_d - \varepsilon_o \mu_o}}$$

We find that for a dielectric constant of 2.2, and a width of 10 mm,

$$f_c = 13.7\ GHz$$

Step 4: find the minimum air gap width for operation at 8 GHz

To find the minimum width, we should consider the rate at which the electric field attenuates on either side of the dielectric for the TE_{00} mode. In this case, $\beta_y = 0$, and the electric field outside of the dielectric will be given by equation (4.3),

$$E_x = 0$$

$$E_y = -\frac{A_o p}{\varepsilon_o} e^{-px} e^{-j\beta_g z}$$

$$E_z = 0$$

The electric field decays exponentially from the dielectric at rate p. Solve the characteristic equation (4.7) to find p and h_n, where a is the width of the dielectric, and $\varepsilon_r = 2.2$.

$$pa = h_n a \tan\frac{h_n a}{2}$$

$$(pa)^2 + (h_n a)^2 = (\varepsilon_r - 1)(k_o a)^2$$

We obtain a value of $p = 118.4$, and using (4.8)

$$\beta_g{}^2 = \varepsilon_r k_o{}^2 - h_n{}^2$$

$$where\ \ k_o = \frac{2\pi}{\lambda_o},\ \ \beta_g = \frac{2\pi}{\lambda_g}$$

a guide wavelength, $\lambda_g = 30.6$ mm.

In this case, we wish to avoid an attenuating standing wave between the outside wall and center dielectric. This will always exists, however, if the separation is large enough, the standing wave will be small since the wave is attenuating.

$$g \approx \pi / p = 26.5 \text{ mm}$$

Thus, a minimum air gap, g, of 26.5 mm is required on each side of the H-guide for a minimum operating frequency of 8 GHz. At higher frequencies, standing waves might exist, but are weak because of the exponential decay. The total width of the H-guide for a minimum operating frequency of 8 GHz is therefore

2 * 26.5 mm + 10 mm = 63 mm

Final dimensions

The dimensions of the H-guide for single-mode operation from 8 to 13.7 GHz is then shown in the figure below.

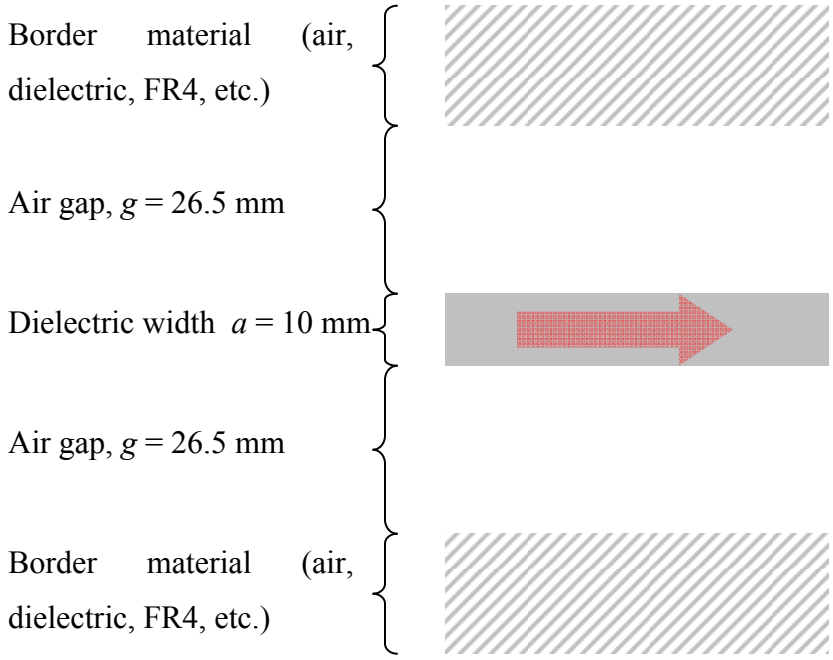

Fig. F.1 Required dimensions for a single mode H-guide operating from 8 to 13.7 GHz formed out of 62 mils thick Rogers 5880.

Example 2: Periodic H-guide Structure

Design an Electromagnetic Band Pass (EBP) H-guide periodic structure that includes a passband from 8 to 18 GHz. Your machinist informs you that the thinnest structure he can safely machine is 1 mm.

Step 1: H-guide design

Let us make use of Example 1 for a substrate of Rogers 5880 that is 1.575 mm thick. Even though the single mode operation applies from 8 to 13.7 GHz only, this is not a major concern for a passband structure that simply aims to pass energy. In addition, odd modes only appear when excited through the introduction of asymmetric structures.

Therefore,

a = 10 mm

air gap, g = 26.5 mm

Step 2: Find the dimensions of the structure to satisfy a first resonant frequency of 18 GHz

This is one example of an "inverse" operation. We can determine requirements on the structure given a certain criteria.

The first resonant frequency can be found using equation (4.19),

$$s = \frac{n\pi - \beta_v d}{\beta_g} \quad where\, n = 1,2,...$$

where n = 1.

Again, we must solve (4.7), to find h_n, where a is the width of the dielectric, and ε_r = 2.2.

$$pa = h_n a \tan\frac{h_n a}{2}$$

$$(pa)^2 + (h_n a)^2 = (\varepsilon_r - 1)(k_o a)^2$$

Apply (4.8)

$$\beta_g{}^2 = \varepsilon_r k_o{}^2 - h_n{}^2$$

$$where\ \ k_o = \frac{2\pi}{\lambda_o},\ \ \beta_g = \frac{2\pi}{\lambda_g}$$

At 18 GHz,

$$\beta_g = 518.9$$

and for a parallel plate waveguide,

$$\beta_v = 559.5$$

Inserting these into (4.19), for a minimum vane width of d = 1 mm,

$$s = 4.98 \text{ mm}$$

The final structure is then shown in the figure below,

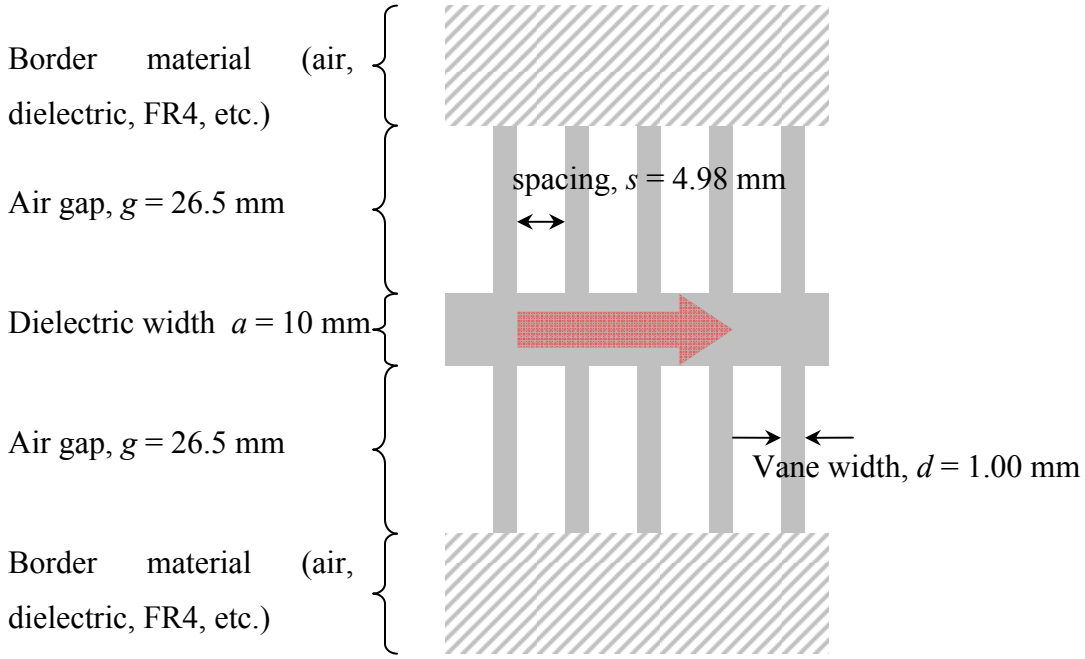

Fig. F.2 Design of a periodic structure using an inverse operation.

Example 3: H-Guide to Microstrip Transition

A 50 Ohm microstrip line is fabricated using 62 mil thick (1.575 mm) thick Rogers 5880. Find rough dimensions for a microstrip to 10 mm wide H-guide transition that operates with a minimum frequency of 8 GHz. To improve the design, explain which parameters must be input into the optimizer in a numerical simulator.

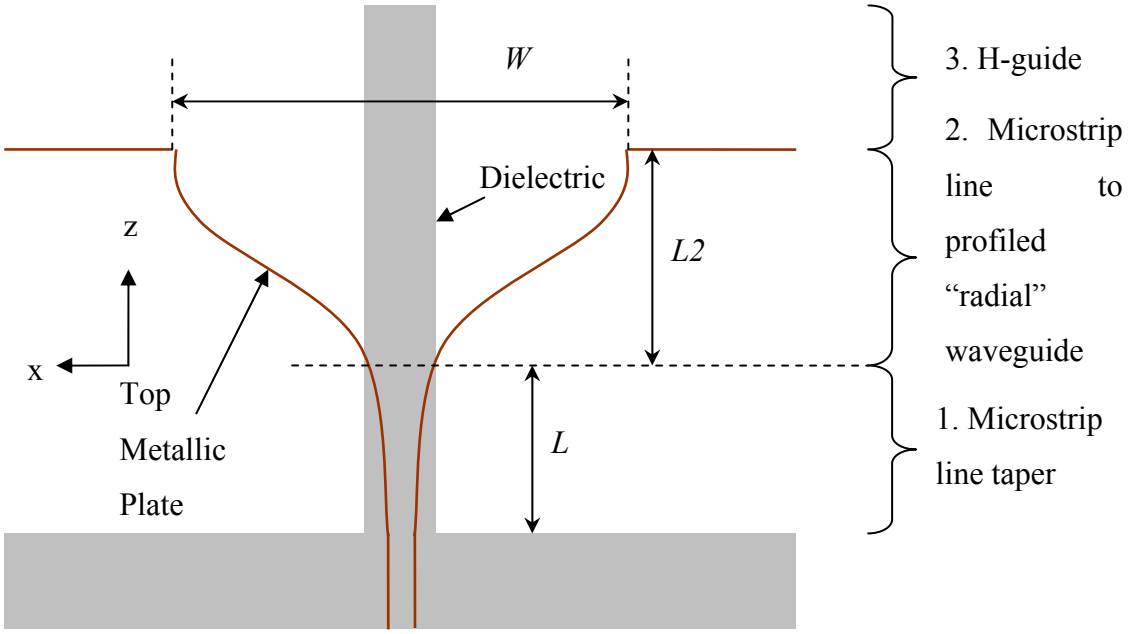

Fig. F.3 Microstrip to H-guide transition

Step 1: Design a microstrip line exponential taper that matches the impedance between the 50 Ohm microstrip line, and a 10 mm wide microstrip line, for a minimum frequency of 8 GHz.

Using equations in Pozar [1], a 50 Ohm microstrip line should be 4.85 mm wide for a 1.575 mm thick Rogers 5880 substrate.

Using a ***non***-power corrected multiple reflection model from the textbook by Pozar, approximate dimensions for the taper using are found.

From equations in Pozar [1],

$$Z(z) = Z_o e^{az}$$
$$0 < z < L$$

$$a = \frac{1}{L} \ln\left(\frac{Z_L}{Z_o}\right)$$
$$\Gamma = \frac{\ln\left(\frac{Z_L}{Z_o}\right)}{2} e^{-j\beta L} \frac{\sin \beta L}{\beta L}$$

Z_o is the characteristic impedance of the microstrip line and is equal to 50 Ohms.

Z_L is the characteristic impedance of a 50 Ohm microstrip line

β is the propagation constant for the microstrip line

The length of the exponential taper should be greater than $\lambda / 2$, or $\beta L > \pi$

From equations in Pozar [1] for a microstrip line, a 10 mm wide microstrip line has a characteristic impedance of

Z_L = 29.5 Ohms

We can then find the rate of the exponential, a,

a = -27.8

β is found for a 50 Ohm microstrip line at 8 GHz to be

β = 229.4 rad / m

Then the minimum length of the taper is

$L = \pi / \beta$ = 1.37 cm

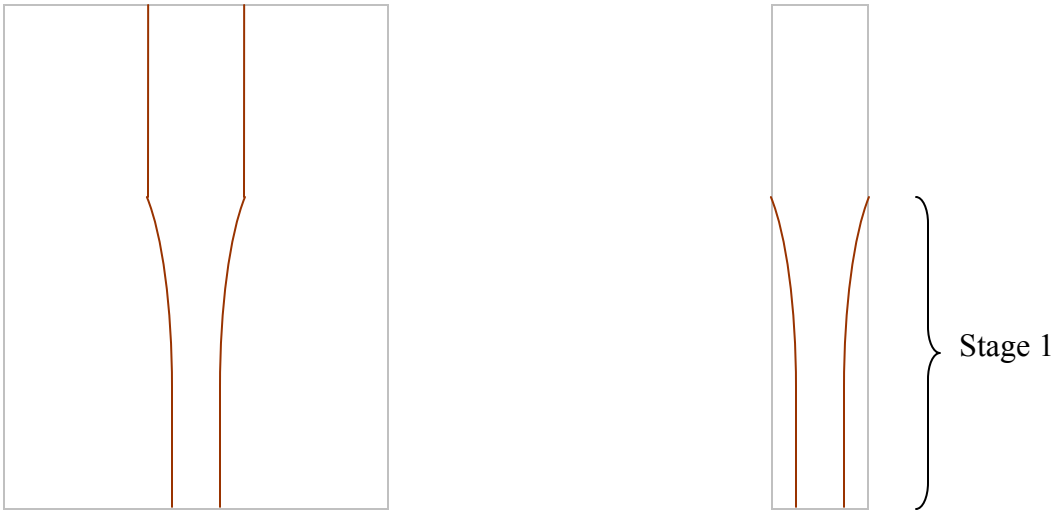

Fig. F.4 (a) a microstrip line exponential taper from 50 Ohm to a 10 mm wide line. (b) a microstrip to 10 mm wide line where the dielectric is also 10 mm wide.

Step 2: Find rough dimensions for the wide microstrip to profiled "Radial" waveguide section whose lowest operating frequency is 8 GHz.

The microstrip line taper of problem a) is used to find an approximate length for the required exponential taper section. The actual length may vary because the 10 mm wide microstrip line has air on either side as shown in Fig. F.4(b).

After this stage, the radial horn shape should be used to widen the electric field. The maximum width of the transition will be limited by non-ideal effects at the edges of the transition, where unwanted currents travel along the edges of the metallic plates.

The minimum width of the transition is found using the exponential rolloff of the H-guide, using attenuation constant "*p*". This was found in Example 1 for 8 GHz and a 10 mm wide H-guide in Rogers 5880 to be $p = 118.4$. The corresponding maximum air gap width at 8 GHz was then found to be 26.5 mm. The maximum total width, W, was found to be 63 mm.

In this case, however, the width must be less than 63 mm, since the electric fields at the edges do not end abruptly as for Perfect Electric Conductor (PEC) edges. The optimal width and length should be found using numerical simulation.

Example 4: Exponential Taper

Use the power-corrected multiple reflection model proposed in this thesis to verify the exponential taper calculation in Example 3.

Step 1: Use existing non-power corrected model for an exponential taper.

The input is a 50 Ohm transmission line in 1.575 mm thick Rogers 5880. The output line is a 30 Ohm line and the length of the taper is 1.37 cm. In this problem, the magnitude of the equation below from Pozar [1] will be compared to the multiple reflection model.

$$\Gamma = \frac{\ln\left(\frac{Z_L}{Z_o}\right)}{2} e^{-j\beta L} \frac{\sin \beta L}{\beta L}$$

Z_o = 50 Ohms

Z_L = 30 Ohms

L = 1.37 cm

Step 2: Compare to the discrete, power-corrected multiple reflection model proposed in this thesis.

The multiple reflection model proposed in previous chapters can be used in a discrete case, where the power correction factor makes the method more robust. Meaning, previous multiple reflection models required that each incremental reflection must be very small, where the power-corrected multiple reflection model reduces this requirement.

Let us consider the same exponential taper, however, with 10 discrete steps instead of a continuous curve.

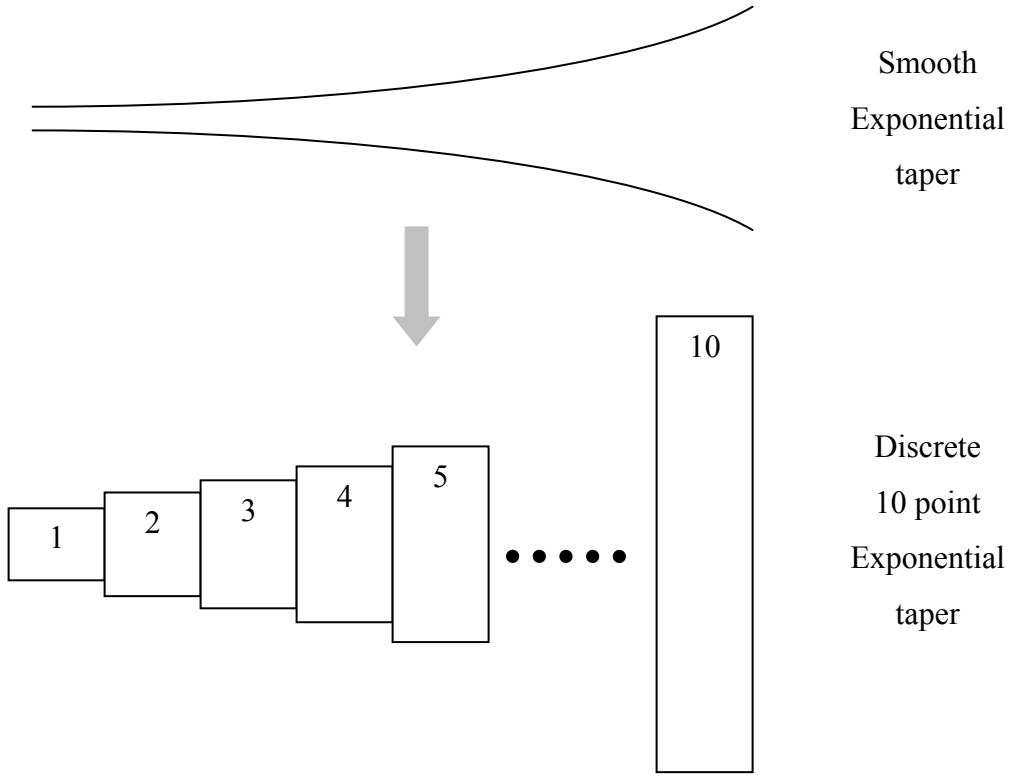

Fig. F.5 Smooth exponential taper and discrete 10 point exponential taper used for the multiple reflection model.

Now, use the power corrected model as follows for two segments first,

$$\Gamma_{31} = \Gamma_{21} + (1 - |\Gamma_{21}|^2)\Gamma_{32} e^{-2j\theta_2}$$

where $\theta_2 = \beta_2 l_2$

Notice that the bracketed term is not squared, since each reflection considers only one interface, not two as in previous chapters. Again, a cascaded approach will be used to find the reflection from three and more interfaces.

$$\Gamma_{41} = \Gamma_{31} + (1 - |\Gamma_{31}|^2)\Gamma_{43} e^{-2j\theta_3}$$

This result may be generalized as a sum as follows,

$$\Gamma_{N1} = \sum_{n=1}^{N} \left(1 - \left|\Gamma_{n1}\right|^2\right) \Gamma_{(1+n)(n)} e^{-2j(n-1)\theta_n}$$

where

$$\Gamma_{11} = 0$$

The results are compared to Pozar [1] in Fig. F.6.

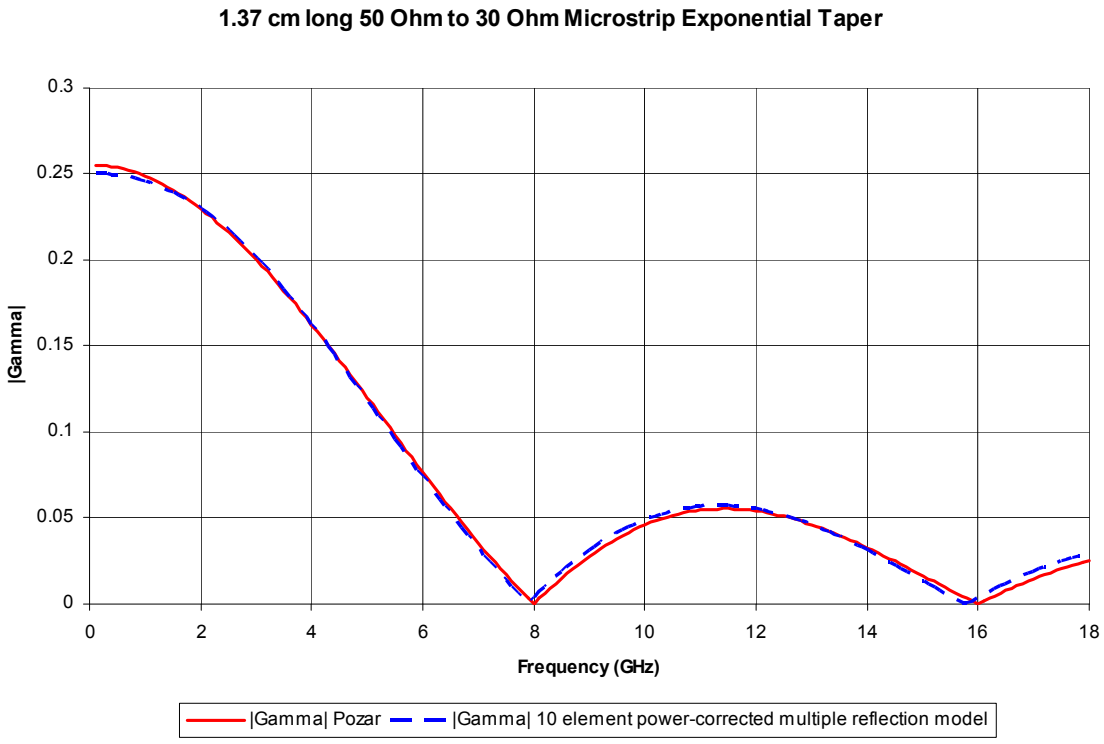

Fig. F.6 Exponential taper from Pozar [1] vs. 10 element power corrected multiple reflection model.